UNIVERSITY OF PISA: LEONARDO DA VINCI SCHOOL

---

Address in Remote Sensing

**phD thesis**

# INNOVATIVE SAR & ISAR SIGNAL PROCESSING


Tutor:
Prof. **BERIZZI FABRIZIO**

phD student:
**DOMENICO OLIVADESE**


---

ACADEMIC YEAR 2012-2013

**To Tiziana**

# Abstract

This thesis reports on research into the field of Synthetic Aperture Radar (SAR) and Inverse Synthetic Aperture Radar (ISAR) signal processing. The contributions of this thesis may be divided into two following parts:

- A new bistatic 3D near field circular SAR imaging algorithm was developed. High resolution radar imaging is typically obtained by combining wide bandwidth signals and synthetic aperture processing. High range resolution is obtained by using modulated signals whereas high cross range resolution is achieved by coherently processing the target echoes at different aspect angles of the target. Anyway, theoretical results have shown that when the aspect angle whereby the target is observed is sufficiently wide, high resolution target images can be obtained by using continuous wave (CW) radars [2], therefore allowing to reduce hardware costs. In a similar way, three dimensional radar imaging can be performed by coherently processing the backscattered field as a function of two rotation angles about two orthogonal axes [3].Three dimensional target radar imaging can be efficiently obtained by means of a 3D Fourier Transform, when the far-field (planar wave) approximation holds. Otherwise, the wavefront curvature has to be accounted for. For this reason, a new algorithm based on a near field spherical wave illumination that takes into account the wavefront curvature by adopting a planar piecewise approximation was designed. This means that the wavefront is assumed to be locally planar around a given point on the target. The operator that the algorithm uses for the focusing procedure is a space variant focusing function which aims at compensating the propagation losses and the wavefront curvature. The algorithm has been developed under the Microwave Electronic Imaging Security and Safety Access (MELISSA) project. The system MELISSA is a body scanner whose purpose is the detection of concealed objects. The added value of the system is the capability to provide an electromagnetic image of the concealed objects. The author would like to thank all people that worked at the project, all LabRass colleagues, all people who designed and acquired real data, all

people that permitted the drafting of the first part of this thesis. The developed algorithm was presented in the chapter 1. The goal of this work was the system design concerning the imaging point of view, by simulating and therefore predicting the system performance by means of the developed algorithm. In the chapter 2 was shown how the design was achieved. Finally, in the chapter 3, the results on real data measured in anechoic chamber with a system with characteristics very close to the final system prototype MELISSA, was presented.

- A new way of ISAR processing has been defined, by applying the traditional ISAR processing to data acquired from passive radars. Purpose of the ISAR processing is to extract an electromagnetic bi-dimensional image of the target in order to determine the main geometric features of the target, allowing (when possible) recognition and classification. Passive radars are able to detect and track targets by exploiting illuminators of opportunity (IOs). In this work of thesis, it will be proven that the same concept can be extended to allow for Passive Inverse Synthetic Aperture Radar (P-ISAR) imaging. A suitable signal processing is detailed that is able to form P-ISAR images starting from range-Doppler maps, which represent the output of a passive radar signal processing. Multiple channels Digital Video Broadcasting - Terrestrial (DVB-T) signals are used to demonstrate the concept as they provide enough range resolution to form meaningful ISAR images. The problem of grating lobes, generated by DVB-T signal, is also addressed and solved by proposing an innovative P-ISAR technique. The second part of this thesis has been developed under the Array Passive ISAR adaptive processing (APIS) project. APIS is defined as a multichannel, bi-static single receiver for array passive radar, capable of detecting targets and generating ISAR images of the detected targets for classification purposes. The author would like to thank all people that worked at the project, all LabRass colleagues, all people who designed, built the prototype and acquired real data, all people that permitted the drafting of the second part of this thesis. In the chapter 4, the basics on Passive Bistatic Radar (PBR) was briefly recalled, the P-ISAR processor was detailed and the new algorithm per the Grating Lobes Cancellation was presented. In the chapter 5, some numerical results on simulated data was shown, in order to demonstrate the potentiality of the P-ISAR, for the imaging and classification purpose. In fact, by using more than three adjacent channels and by observing the signal for a long time, finer range and cross-range resolutions, respectively, could be achieved. Finally, the obtained results on real data was discussed in the chapter 6.

# List of Acronyms

**SAR** Synthetic Aperture Radar

**ISAR** Inverse Synthetic Aperture Radar

**P-ISAR** Passive Inverse Synthetic Aperture Radar

**DFT** Discret Fourier Transform

**IDFT** Inverse Discret Fourier Transform

**CW** Continuous Wave

**FFT** Fast Fourier Transform

**IFFT** Inverse Fast Fourier Transform

**FT** Fourier Transform

**IFT** Inverse Fourier Transform

**LoS** Line of Sight

**PSF** Point Spread Function

**MELISSA** Microwave Electronic Imaging Security and Safety Access

**MMW** Millimeter Waves

**CW** continuous wave

**BEM** Bistatically equivalent monostatic

**SLL** Side Lobe Level

**PP** Polypropylene

**TATB** Triamino-Trinitobenzene

**PEC** Perfect Conductor

**APIS** Array Passive ISAR adaptive processing

**DVB-T** Digital Video Broadcasting - Terrestrial

**DVB** Digital Video Broadcasting

**COFDM** Coded Orthogonal Frequency Division Multiplex

**DAB** Digital Audio Broadcasting

**IOs** illuminators of opportunity

**RD** range Doppler

**CAF** Cross-Ambiguity Function

**SVA** Spatially Variant Apodization

**S-SVA** Super - Spatial Variant Apodization

**ICBA** Image Contrast Based Autofocusing

**FM** Frequency Modulated

**CPI** Coherent Processing Interval

**LoS** Line of Sight

**IC** Image Contrast

**LPFT** local polynomial Fourier transform

**IE** Image Entropy

**TPS** Transport Parameter Signaling

**ISL** Integrated Side Lobe level

**PRI** Pulse Repetition Interval

**IPP** Image Projection Plane

**USRP** Universal Software Radio Peripheral

**ADS-B** Automatic Dependent Surveillance - Broadcast

**VHF** Very High Frequency

**UHF** Ultra High Frequency

**RCS** Radar Cross Section

**PBR** Passive Bistatic Radar

# Contents

**Abstract** **v**

**List of Acronyms** **vii**

**List of Figures** **xv**

**List of Tables** **xxi**

**1 Innovative SAR Processing** **1**
1.1 3D near field SAR imaging Algorithm . . . . . 1
1.2 3D SAR image focusing . . . . . 4
1.3 Mapping on the spatial frequencies . . . . . 5
1.4 Reconstruction of the reflectivity function . . . . . 6

**2 Microwave Electronic Imaging Security and Safety Access system** **9**
2.1 Introduction . . . . . 9
2.2 system requirements and design . . . . . 10
2.2.1 Working frequency . . . . . 10
2.2.2 Distance between sensors and target: “ the near field issue “ . . . . . 11
2.2.3 Geometric resolutions . . . . . 12
Vertical resolution . . . . . 12
Horizontal resolution . . . . . 15
Signal model . . . . . 15
Signal model: Bi-static geometry both in vertical and horizontal plane . . . . . 18
2.2.4 Volume of focus . . . . . 18
2.2.5 Radiometric resolution . . . . . 19
2.2.6 Criteria for Sampling in Frequency, Azimuth and Vertical coordinate . . . . . 20

Sampling in angle . . . 20
Sampling in the vertical dimension . . . 21
Sampling in frequency . . . 21
2.3 System Analysis and Design . . . 22
2.3.1 Antenna Design . . . 22
2.3.2 Spatial frequencies analysis . . . 24
2.3.3 Geometric resolutions analysis . . . 24
Vertical resolutions . . . 24
Horizontal resolutions . . . 26
2.3.4 Radiometric resolutions analysis . . . 29
2.3.5 Direct Signal Interference . . . 31
2.3.6 Waveform Bandwidth design . . . 33
2.4 Sum up: final system design . . . 34

**3 Real Data Results and Analysis 37**
3.1 First target: Cylinder . . . 37
3.2 Second target: Panel with different materials . . . 42
3.3 Third target: Panel with balls and padlock . . . 44

**4 Innovative ISAR Signal Processing 53**
4.1 APIS: Array Passive ISAR adaptive processing . . . 53
4.2 Introduction . . . 53
4.3 Basics on Passive Bistatic Radar (PBR) . . . 55
4.4 Bistatic Passive Isar Imaging . . . 57
4.5 P-ISAR algorithm . . . 61
4.5.1 Sub-image inversion . . . 63
4.5.2 Autofocusing algorithm . . . 63
4.5.3 Image Formation . . . 64
4.5.4 Time Windowing . . . 65
4.5.5 Image Scaling . . . 65
4.6 DVB-T signals and high range resolution . . . 66
4.7 Grating Lobes Cancellation Algorithm . . . 67

**5 Numerical Results on Simulated Data 75**
5.1 Isar Imaging results on aerial targets . . . 75
5.1.1 CESSNA 172 target . . . 75
5.1.2 BOEING 747 target . . . 80
5.2 Isar Imaging results on maritime targets . . . 83
Experiment 1 . . . 83
Experiment 2 . . . 85
5.3 Performance of the Grating Lobes cancellation algorithm . . . 88

**6 Results on Real Data** **93**
6.1 Aerial Target: Boeing 737 . . . . . 93
6.2 Maritime Target: container ship LIWIA P . . . . . 96
6.3 Aerial Target: Airbus 340 . . . . . 101

**7 Conclusions** **107**

**Bibliography** **109**

# List of Figures


1.1 Acquisition geometry of the system . . . . . 1
1.2 Reference system . . . . . 2

2.1 Representation of the shelter . . . . . 11
2.2 Geometry for calculate the vertical resolution: mono-static case 13
2.3 Signal representation in the frequencies spatial domain: mono-static case . . . . . 13
2.4 Geometry for calculate the vertical resolution: bi-static case . . 14
2.5 Signal representation in the frequencies spatial domain: bi-static case . . . . . 14
2.6 Point Spread Function (PSF) in the horizontal plane of an ideal scatterer in (0,0,0) . . . . . 17
2.7 Signal representation in the spatial frequencies domain, if just one frequency is transmitted . . . . . 17
2.8 Vertical profile by varying the number of antenna elements: a) #91 elements, b) #151 elements, c) #201 elements, d) #251 elements . . . . . 23
2.9 Spatial frequencies domain of the focusing point in (0 cm, 0 cm, 0cm) . . . . . 24
2.10 Spatial frequencies domain of the focusing point in (50 cm,40 cm, 70cm) . . . . . 24
2.11 Vertical profile of the point of coordinate (0,0,0) with a) $f_0 = 35GHz$ b) $f_0 = 16.5GHz$ . . . . . 25
2.12 Vertical profile of the point of coordinate (0,0,1) with a) $f_0 = 35GHz$ b) $f_0 = 16.5GHz$ . . . . . 25
2.13 PSF in the horizontal plane of the scatterer (0,0,0) by scanning an angle of $2\pi$, with a) $f_0 = 35GHz$ b) $f_0 = 16.5GHz$ . . . . . 27
2.14 PSF in the horizontal plane of the scatterer (0.5,0.4,0.7) by scanning an angle of $2\pi$, with a) $f_0 = 35GHz$ b) $f_0 = 16.5GHz$ . . . 27
2.15 Simulation geometry: the transmitter (colored line) moves jointly with the receiver. . . . . 28

2.16 Horizontal PSF with a scan angle of 120°@35$GHz$ . . . . . 29
2.17 Horizontal PSF with a scan angle of 120°@16.5$GHz$ . . . . . 29
2.18 Signal representation in the spatial frequency domain for a scanning angle of 120° . . . . . 30
2.19 Reconstructed image in the vertical plane of three different targets overlapped to the skin - a) Pec + Skin b) TATB + Skin c) PP+Skin . . . . . 31
2.20 Reconstructed image (a) Received signal (b) Only direct signal . 32
2.21 Reconstructed image (a) only target (b) obtained by subtracting the two images . . . . . 33
2.22 Reconstructed image in the horizontal plane, scanning angle of 120° . . . . . 35

3.1 Target used for the measurements . . . . . 37
3.2 Real data acquisition geometry . . . . . 38
3.3 Reconstructed image of the cylinder of fig. 3.1, in the $x_2 - x_3$ vertical plane . . . . . 39
3.4 Reconstructed image of the cylinder of fig. 3.1, in the $x_1 - x_3$ vertical plane . . . . . 39
3.5 Reconstructed image of the cylinder of fig. 3.1, in the $x_1 - x_2$ horizontal plane . . . . . 40
3.6 Reconstructed image of the cylinder of fig. 3.2, in the $x_1 - x_3$ vertical plane, by exploit the multi frequency signal . . . . . 41
3.7 Reconstructed image of the cylinder of fig. 3.2, in the $x_1 - x_2$ horizontal plane, by exploit the multi frequency signal . . . . . 41
3.8 (a) - Measurement setup for the panel multi-material (copper in the upper left corner, ceramic in the upper right corner, liquid in the lower left corner, plastic in the bottom right corner). (b) - Geometry of scanning: the angle between transmitter and receiver is 60° and the scanning is performed for an angle of 60° 43
3.9 Reconstructed image of the target depicted in fig. 3.8 for (a) $x_3 = 0$ - (b) $x_3 = 0.1$ . . . . . 43
3.10 Reconstructed image of the target depicted in fig. 3.8 in the vertical plane for different values of $x_1$, mono-frequency case. . . 46
3.11 Reconstructed image of the target depicted in fig. 3.8 in the horizontal plane, multi frequency case. . . . . 47
3.12 Reconstructed image at $x_1 = -0.13m$of the target depicted in fig. 3.8 in the vertical plane, multi frequency case. . . . . 47
3.13 Measurement setup . . . . . 48
3.14 Reconstructed image of the background . . . . . 48
3.15 Target: Panel with two balls of $9mm$ of diameter and a padlock 49

3.16 Reconstructed image of the target depicted in fig. 3.15 . . . . . 49
3.17 Reconstructed image of the target depicted in fig. 3.15, at which the background has been removed . . . . . 50
3.18 Target: three balls plus a padlock and a metal box . . . . . 50
3.19 Reconstructed image of the target of figure 3.18 . . . . . 51

4.1 APIS demonstrator . . . . . 54
4.2 The bistatic geometry . . . . . 56
4.3 Bistatic range resolution. The distance between the contours are given by the signal bandwidth. $T_x(red), R_x(blue)$. . . . . 57
4.4 Bistatic ISAR geometry. . . . . 58
4.5 ISAR processing scheme . . . . . 60
4.6 General ISAR processing flow chart . . . . . 61
4.7 P-ISAR Algorithm flow chart . . . . . 62
4.8 DVB-T ambiguity function . . . . . 67
4.9 Spectrum of the multi-channel DVB-T signal . . . . . 68
4.10 Algorithm flow chart of the Grating Lobe cancellation procedure 69
4.11 Simulation Geometry . . . . . 71
4.12 P-ISAR image before the GLC algorithm in the case of the scatterers with different amplitude . . . . . 72
4.13 P-ISAR image after the GLC algorithm in the case of the scatterers with different amplitude . . . . . 72
4.14 P-ISAR image before the GLC algorithm in the case of the scatterers with equal amplitude . . . . . 72
4.15 P-ISAR image after the GLC algorithm in the case of the scatterers with equal amplitude . . . . . 73

5.1 Point-like scatterer model of a CESSNA 172 . . . . . 76
5.2 Block scheme of the pre-processing used for simulating the theoretical scenario (sub-image inversion of the figure 4.7 . . . . . 77
5.3 Bistatic geometry and zoom of the trajectory of the target . . . 77
5.4 Target projected onto the estimated image plane (a) range-cross range (b) range-Doppler . . . . . 78
5.5 (a)-Target's ISAR image after focusing with known radial motion parameters (b)- zoom of the ISAR image (c) - zoom of the ISAR image with the superimposed point-like scatterers . . . . 78
5.6 (a)-Target's ISAR image after focusing processing (b)- zoom of the ISAR image (c) - zoom of the ISAR image with the superimposed point-like scatterers . . . . . 79
5.7 Point-like scatterer model of the Boeing 747 (a)-Top view (b)-Side view . . . . . 80

5.8 Target projected onto the estimated image plane (a) range-cross range (b) range-Doppler . . . 81
5.9 Target's ISAR image of the Boeing, obtained by exploiting (a)-10 channels (b)- 3 channels . . . 81
5.10 (a)- Extracted scatterers of the target (b)- Regression line of the Cross range scaling algorithm . . . 82
5.11 Fully scaled ISAR images of the target (a) - 10 channels (b) - 3channels . . . 82
5.12 target . . . 84
5.13 geometry . . . 84
5.14 target sub image . . . 85
5.15 target ISAR image . . . 86
5.16 geometry . . . 86
5.17 target sub image . . . 87
5.18 target ISAR image . . . 87
5.19 target ISAR image obtained by using the time windowing algorithm . . . 88
5.20 Spectral content of the signal before to fill out the gaps . . . 89
5.21 P-ISAR image after the SVA algorithm . . . 89
5.22 Spectral content of the P-ISAR image after the SVA algorithm . 90
5.23 P-ISAR image after the cancellation technique . . . 90
5.24 Spectral content with the gaps filled out . . . 91

6.1 Boeing-737 . . . 94
6.2 Geometry of the real measurements concerning the Boeing-737 . 94
6.3 Range-Doppler map . . . 95
6.4 P-ISAR image of the target . . . 95
6.5 Simulated P-ISAR image by substituting the real target with a point-like scatterer one. . . . 96
6.6 A picture of the target used in the first experiment - the target was a container ship . . . 97
6.7 Geometry of real data . . . 97
6.8 Range-Doppler map . . . 98
6.9 Crop of the unfocused target . . . 99
6.10 Range Profiles of the unfocused target . . . 99
6.11 Results obtained by considering data frame 1: (left) range profile of the target after autofocusing, (right) ISAR image of the target . . . 100
6.12 ISAR image of the target by considering the frame1, after the Grating Lobes cancellation . . . 100

6.13 Results obtained by considering data frame 2: (left) range profile of the target after autofocusing, (right) ISAR image of the target . . . 101
6.14 ISAR image of the target by considering the frame2, after the Grating Lobes cancellation . . . 102
6.15 A picture of the target used in the second experiment - the target was an Airbus 340-313X . . . 102
6.16 Geometry of real data-aerial target . . . 103
6.17 Range-Doppler map -Airbus 340 . . . 103
6.18 Unfocussed target image -Airbus 340 . . . 104
6.19 Range Profiles of the unfocused target - Airbus 340 . . . 104
6.20 (left) range profile of the target after autofocusing, (right) ISAR image of the target . . . 105
6.21 ISAR image of the target after Grating Lobes cancellation - Airbus 340 . . . 105

# List of Tables


2.1 Vertical resolutions: scatterer in (0,0,0) . . . . . 15
2.2 Vertical resolutions: scatterer in (0,0,1) . . . . . 15
2.3 Vertical resolutions at $-3dB$ . . . . . 26
2.4 Horizontal resolutions at $-3dB$ . . . . . 28
2.5 Horizontal resolutions at $-3dB$ Vs theoretical resolutions . . . . 29
2.6 Dielectric properties . . . . . 31
2.7 System parameters for direct interference cancellation . . . . . 32

5.1 Radar parameters . . . . . 84
5.2 Radar parameters . . . . . 85

# Chapter 1

# Innovative SAR Processing

## 1.1 3D near field SAR imaging Algorithm

The algorithm is based on a near field spherical wave illumination. It takes into account the wavefront curvature by adopting a planar piecewise approximation. This means that the wavefront is assumed to be locally planar around a given point on the target. The operator that the algorithm uses for the focusing procedure is a space variant focusing function which aims at compensating the propagation losses and the wavefront curvature. The reflectivity function of the target is estimated by performing a three dimensional Discret Fourier Transform (DFT). The algorithm has been designed on the acquisition geometry shown in fig. 1.1

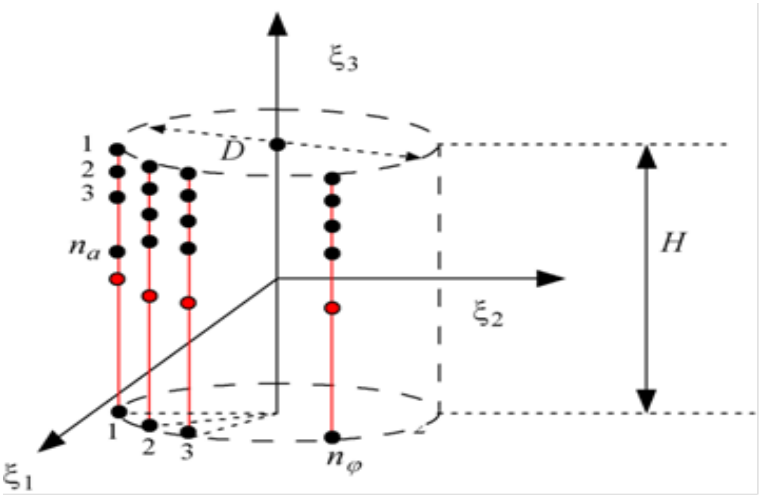


Figure 1.1: Acquisition geometry of the system

The receiver is a linear array of receiving elements aligned along the $\zeta_3$ axis, and its height is indicated with $H$. The transmitter (the Red filled dot of the fig.1.1) is a CW radar and it is located in the middle of the receiving array. Both the transmitter and the receiver move along a circular path around the $\zeta_3$ axis, in order to illuminate the target from all around. $D$ is the diameter of the circular acquisition system. $n_a$ and $n_\phi$ are the number of elements of the receiving array along the $\zeta_3$ axis and the number of the positions in the $\zeta_1 - \zeta_2$ plane, respectively. The SAR technique is performed both along in the horizontal and vertical direction, but in a different way. Along the horizontal direction ( $\zeta_1 - \zeta_2$ plane) the whole array move around the target with a velocity $V$, scanning a circular arc $S$ with a sampling time $T_{co}$, therefore the high resolution is acquired by collecting the signal in each azimuth $n_\phi$ position of the array. Along the vertical direction ($\zeta_3$ axis), the movement of the array is performed by using an electronic switch of the single dipoles. Each element of the array acquires the back scattered signal only for a time $T_{cv}$, that is the sampling time in the vertical dimension. The required high resolution is therefore performed by collecting the signal in each vertical position of the array. As a consequence of this working solution, a bi-static configuration has to be considered, as shown in fig. 1.2.

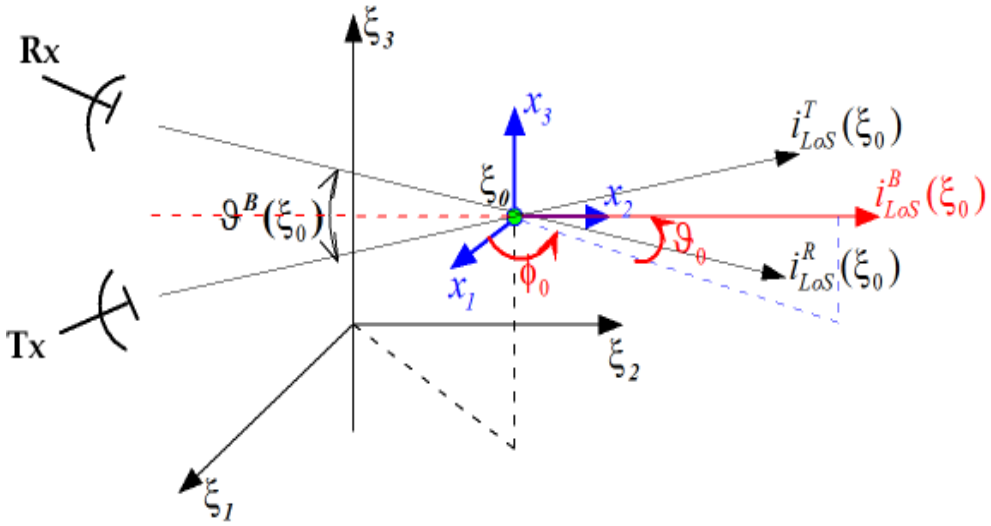


Figure 1.2: Reference system

Two different reference systems have to be considered. One is an absolute reference system $T_\zeta$ and the other one is a mobile reference system $Tx$, with the origin sited in a point $\zeta_0$ belonging to the target and with the axis parallel to the axis of $T_\zeta$. Let consider the transmitter on the $\zeta_0$ plane, for a fixed

element of the receiving array, the bi-static base band received signal [7] can be written as in eq. 1.1

$$s_r(\phi,\zeta_3) = \int_v \frac{g(\zeta)}{R_{T,\zeta}(\phi,\zeta_3)R_{R,\zeta}(\phi,\zeta_3)} \cdot e^{-j\frac{2\pi}{\lambda}(R_{T,\zeta}(\phi,\zeta_3)+R_{R,\zeta}(\phi,\zeta_3))}\, d\zeta \tag{1.1}$$

where $g(\zeta)$ is the reflectivity function of the target, $v$ is the spatial domain whereby the target reflectivity function is defined. $\phi$ and $\zeta_3$ are the cylindrical coordinates of the single receivers. $R_{T,\zeta}(\phi,\zeta_3)$ and $R_{R,\zeta}(\phi,\zeta_3)$ are respectively the distances between the transmitter and the receiver and a point $\zeta_0$ belonging to the target. Let define a small volume $v_0$ around $\zeta_0$, where all the scatterers belonging to such volume experience only the first term of the received signal of the eq. 1.2

$$\begin{aligned} s_r(\phi,\zeta_3) = &\int_{v_0} \frac{g(\zeta)}{R_{T,\zeta}(\phi,\zeta_3)R_{R,\zeta}(\phi,\zeta_3)} \cdot e^{-j\frac{2\pi}{\lambda}(R_{T,\zeta}(\phi,\zeta_3)+R_{R,\zeta}(\phi,\zeta_3))}\, d\zeta \\ &+ \int_{v-v_0} \frac{g(\zeta)}{R_{T,\zeta}(\phi,\zeta_3)R_{R,\zeta}(\phi,\zeta_3)} \cdot e^{-j\frac{2\pi}{\lambda}(R_{T,\zeta}(\phi,\zeta_3)+R_{R,\zeta}(\phi,\zeta_3))}\, d\zeta \end{aligned} \tag{1.2}$$

The second term of the eq. 1.2 can be considered as noise, if only the received signal from the scatterers in the volume $v_0$ is of interest. By considering the reference system $T_x$ embedded on the focusing point $\zeta_0$ and by setting the change of coordinates $\zeta = x + \zeta_0$, the eq.1.2 can be rewritten as 1.3

$$\begin{aligned} s_r(\phi,\zeta_3) = &\int_{v_0} \frac{f(x)}{R_{T,x}(\phi,\zeta_3)R_{R,x}(\phi,\zeta_3)} \cdot e^{-j\frac{2\pi}{\lambda}(R_{T,x}(\phi,\zeta_3)+R_{R,x}(\phi,\zeta_3))}\, dx \\ &+ \int_{v-v_0} \frac{f(x)}{R_{T,x}(\phi,\zeta_3)R_{R,x}(\phi,\zeta_3)} \cdot e^{-j\frac{2\pi}{\lambda}(R_{T,x}(\phi,\zeta_3)+R_{R,x}(\phi,\zeta_3))}\, dx \end{aligned} \tag{1.3}$$

where it is assesses that $f(x) = g(\zeta - \zeta_0)$ is the reflectivity function of the target related to the system of coordinate $T_x$. As can be noted from the eq. 1.3, the bi-static phase of the received signal is the sum of the mono-static phases of the transmitter and receiver, 1.4

$$\begin{aligned} \Psi_B(\phi,\zeta_3;x) = &\frac{2\pi}{\lambda}R_{T,x}(\phi,\zeta_3) + \frac{2\pi}{\lambda}R_{R,x}(\phi,\zeta_3) \\ &= \Psi_T(\phi,\zeta_3;x) + \Psi_R(\phi,\zeta_3;x) \end{aligned} \tag{1.4}$$

Properly assessing the dimension of the volume $v_0$ in order to fulfill the planar piecewise approximation, the bi-static phases became 1.5

$$\begin{aligned}\Psi_T(\phi,\zeta_3;\zeta_0) &= -\frac{2\pi}{\lambda}R_{T,0}(\phi,\zeta_3) + x\cdot\mathbf{i}^T_{los}(\phi,\zeta_3;\zeta_0)\\ \Psi_R(\phi,\zeta_3;\zeta_0) &= -\frac{2\pi}{\lambda}R_{R,0}(\phi,\zeta_3) + x\cdot\mathbf{i}^R_{los}(\phi,\zeta_3;\zeta_0)\end{aligned} \tag{1.5}$$

where $R_{T,0}(\phi,\zeta_3)$ is the distance between the transmitter and the focusing point, $R_{R,0}(\phi,\zeta_3)$ is the distance among the receivers and the focusing point, $\mathbf{i}^T_{los}(\phi,\zeta_3;\zeta_0)$ is the Line of Sight (LoS) of the transmitter and $\mathbf{i}^R_{los}(\phi,\zeta_3;\zeta_0)$ is the LoS of the receiver. The planar piecewise approximation consists in assuming that the distances among the all scatterers in the volume $v_0$ and the origin of the reference system $T_x$ are smaller than the distances between the focusing point $\zeta_0$ and the transmitter and receiver. By using the eq. 1.5, the bi-static phase becomes 1.6

$$\Psi_B(\phi,\zeta_3;\zeta_0) = -\frac{2\pi}{\lambda}\left(R_{T,0}(\phi,\zeta_3) + R_{R,0}(\phi,\zeta_3) + \mathbf{k}(\phi,\zeta_3;\zeta_0)x\cdot\mathbf{i}^B_{los}(\phi,\zeta_3;\zeta_0)\right) \tag{1.6}$$

where $\mathbf{i}^B_{los}(\phi,\zeta_3;\zeta_0)$ is the bi-static LoS along the bisector of the bi-static angle $\theta_B(\phi,\zeta_3;\zeta_0)$ and $\mathbf{k}$ is defined as 1.7

$$k(\phi,\zeta_3;\zeta_0) = |\mathbf{i}^T_{los}(\phi,\zeta_3;\zeta_0) + \mathbf{i}^R_{los}(\phi,\zeta_3;\zeta_0)| = cos(\theta_B(\phi,\zeta_3;\zeta_0)) \tag{1.7}$$

Under these assumptions, the received signal becomes 1.8

$$\begin{aligned}s_r(\phi,\zeta_3) = &\frac{e^{-\frac{2\pi}{\lambda}(R_{T,0}(\phi,\zeta_3)+R_{R,0}(\phi,\zeta_3))}}{R_{T,0}(\phi,\zeta_3)+R_{R,0}(\phi,\zeta_3)}\int_{v_0} f(x)\cdot e^{-j\frac{2\pi}{\lambda}\left(\mathbf{k}(\phi,\zeta_3;\zeta_0)x\cdot\mathbf{i}^B_{los}(\phi,\zeta_3;\zeta_0)\right)}\,dx\\ &+\int_{v-v_0}\frac{f(x)}{(R_{T,x}(\phi,\zeta_3)+R_{R,x}(\phi,\zeta_3)}\cdot e^{-j\frac{2\pi}{\lambda}\left(R_{T,x}(\phi,\zeta_3)+R_{R,x}(\phi,\zeta_3)\right)}\,dx\end{aligned} \tag{1.8}$$

the eq. 1.8 stresses that the received signal can be divided in two parts, one concerning the useful signal coming from the scatterers in the volume $v_0$ and the other one concerning the unwanted signal, that can be thought as a background noise in the final image.

## 1.2 3D SAR image focusing

The focusing operation consists of a spatial dependent (because of the near filed) complex function that multiplies the received signal in order to align the

signal phases and to equalize the signal amplitudes from the considered point, specifically the function is given by eq. 1.9

$$F(\phi,\zeta_3;\zeta_0) = R_{T,0}(\phi,\zeta_3 R_{R,0}(\phi,\zeta_3 e^{-j\frac{2\pi}{\lambda}\left(R_{T,0}(\phi,\zeta_3)+R_{R,0}(\phi,\zeta_3)\right)} \tag{1.9}$$

Therefore, the compensated received signal can be rewritten as eq. 1.10

$$s_{RC}(\phi,\zeta_3;\zeta_0) = s_{RC}^{(v_0)}(\phi,\zeta_3;\zeta_0) + s_{RC}^{(v-v_0)}(\phi,\zeta_3;\zeta_0) \tag{1.10}$$

where

$$s_{RC}^{(v-v_0)}(\phi,\zeta_3;\zeta_0) = F(\phi,\zeta_3;\zeta_0)\int_{v-v_0}\frac{f(x)}{(R_{T,x}(\phi,\zeta_3)+R_{R,x}(\phi,\zeta_3)}\cdot e^{-j\frac{2\pi}{\lambda}\left(R_{T,x}(\phi,\zeta_3)+R_{R,x}(\phi,\zeta_3)\right)}\,dx \tag{1.11}$$

$$s_{RC}^{(v_0)}(\phi,\zeta_3;\zeta_0) = \int_{v_0} f(x)\cdot e^{-j\frac{2\pi}{\lambda}\left(\mathbf{k}(\phi,\zeta_3;\zeta_0)x\cdot\mathbf{i}_{los}^{B}(\phi,\zeta_3;\zeta_0)\right)}\,dx \tag{1.12}$$

It's worth noting that the alignment of the signal phases is correct only for the point $\zeta_0$, whereas all other scatterers in the volume $v_0$ are affected by some residual errors. Out of the volume $v_0$, the alignment doesn't properly work, therefore the term $s_{RC}^{(v-v_0)}(\phi,\zeta_3;\zeta_0)$ represents a manner of superimposed noise floor to the useful signal $s_{RC}^{(v_0)}(\phi,\zeta_3;\zeta_0)$. Let assuming valid this hypothesis the received signal is given by 1.13

$$s_{RC}(\phi,\zeta_3;\zeta_0) \cong\ s_{RC}^{(v_0)}(\phi,\zeta_3;\zeta_0) = \int_{v_0} f(x)\cdot e^{-j\frac{2\pi}{\lambda}\left(\mathbf{k}(\phi,\zeta_3;\zeta_0)x\cdot\mathbf{i}_{los}^{B}(\phi,\zeta_3;\zeta_0)\right)}\,dx \tag{1.13}$$

In order to ensure the validity of the eq. 1.13, a criterion for setting the volume $v_0$ has to be clarified. Let define the volume $v_0$ as 1.14

$$v_0 = \left\{x : \left|\frac{2\pi}{\lambda}\left(R_{T,x}(\phi,\zeta_3)+R_{R,x}(\phi,\zeta_3)\right) - \frac{2\pi}{\lambda}\left(R_{T,0}(\phi,\zeta_3)+R_{R,0}(\phi,\zeta_3)\right)\right| \le \frac{\pi}{2}\right\} \tag{1.14}$$

Under the criterion of eq. 1.14, the volume $v_0$ is called depth of focus.

## 1.3 Mapping on the spatial frequencies

By exploiting the scalar product $x\cdot\mathbf{i}_{los}^{B}(\phi,\zeta_3;\zeta_0)$, the compensated received signal can be rewritten as in eq. 1.15

$$x\cdot\mathbf{i}_{los}^{B}(\phi,\zeta_3;\zeta_0) = x_1\cos(\theta_0(\phi,\zeta_3))\cos(\phi_0(\phi,\zeta_3))+x_2\cos(\theta_0(\phi,\zeta_3))\sin(\phi_0(\phi,\zeta_3))+x_3\sin(\theta_0(\phi,\zeta_3) \tag{1.15}$$

where $\phi_0(\phi, \zeta_3)$ and $\theta_0(\phi, \zeta_3)$ are, respectively, the azimuth and the zenith angles defining the direction of the unit vector $\mathbf{i}_{los}^{B}(\phi, \zeta_3; \zeta_0)$. By substituting the eq. 1.15 in the eq. 1.13, the eq. 1.16 is obtained

$$s_{RC}(\phi, \zeta_3; \zeta_0) = \int_{v_0} f(x) \cdot e^{-j\frac{2\pi}{\lambda}\mathbf{k}(\phi,\zeta_3;\zeta_0)(x_1\cos(\theta_0(\phi,\zeta_3))\cos(\phi_0(\phi,\zeta_3))+x_2\cos(\theta_0(\phi,\zeta_3))\sin(\phi_0(\phi,\zeta_3))+x_3\sin(\theta_0(\phi,\zeta_3))}\, dx \tag{1.16}$$

Let define the spatial frequencies as follows 1.17

$$\begin{aligned} X_1(\phi, \zeta_3; \zeta_0) &= \frac{f_0}{c}\mathbf{k}(\phi, \zeta_3; \zeta_0)\cos(\theta_0(\phi, \zeta_3))\cos(\phi_0(\phi, \zeta_3)) \\ X_2(\phi, \zeta_3; \zeta_0) &= \frac{f_0}{c}\mathbf{k}(\phi, \zeta_3; \zeta_0)\cos(\theta_0(\phi, \zeta_3))\sin(\phi_0(\phi, \zeta_3)) \\ X_3(\phi, \zeta_3; \zeta_0) &= \frac{f_0}{c}\mathbf{k}(\phi, \zeta_3; \zeta_0)\sin(\theta_0(\phi, \zeta_3)) \end{aligned} \tag{1.17}$$

therefore the eq. 1.16 can be rewritten as eq. 1.18

$$s_{RC}(X_1, X_2, X_3; \zeta_0) = W(X_1, X_2, X_3; \zeta_0) \int_{v_0} f(x) \cdot e^{-j\frac{2\pi}{\lambda}(x_1X_1+x_2X_2+x_3X_3)}\, dx \tag{1.18}$$

where

$$W(X_1, X_2, X_3; \zeta_0) = \begin{cases} 1 & (X_1, X_2, X_3) \in D(\zeta_0) \\ 0 & otherwise \end{cases} \tag{1.19}$$

with $D(\zeta_0)$, domain in the space of the spatial frequencies in which the signal $s_{RC}(X_1, X_2, X_3; \zeta_0)$ is defined, by means of the transformation of eq. 1.17. Such domain is dependent on the coordinates of the focusing point.

## 1.4 Reconstruction of the reflectivity function

The eq. 1.18 assesses that the received signal after the focusing procedure is the 3D Fourier transform of the reflectivity function $f(x)$ in the volume $v_0$, limited by the 3D window $W(\cdot)$. As consequence, by applying an Inverse

Discret Fourier Transform (IDFT), the reflectivity function of the target can be estimated by means of 1.20

$$\hat{f}(x;\zeta_0) = \iiint_{D(\zeta_0)} s_{RC}(X_1, X_2, X_3) e^{-j\frac{2\pi}{\lambda}(x_1X_1+x_2X_2+x_3X_3)}\, dX_1\, dX_2\, dX_3 \tag{1.20}$$

The eq. 1.20 can be rewritten as follow 1.21

$$\hat{f}(x;\zeta_0) = f(x) \otimes w(x;\zeta_0) \tag{1.21}$$

where $x \in v_0$, $\otimes$ means the convolution operator and $w(x;\zeta_0)$ represents the 3D IDFT of $W((X_1, X_2, X_3;\zeta_0)$, that is the impulsive response of the system, also called PSF.

# Chapter 2

# Microwave Electronic Imaging Security and Safety Access system

## 2.1 Introduction

It has been recently proved that Millimeter Waves (MMW) [1] are suitable for imaging metallic and non metallic objects, Since MMWs propagate through clothing, they allow the detection of concealed weapons. It is well known that high resolution radar imaging is typically obtained by combining wide bandwidth signals and synthetic aperture processing. High range resolution is obtained by is obtained by using modulated signals whereas high cross range resolution is achieved by coherently processing the target echoes at different aspect angles of the target. Anyway, theoretical results have shown that when the aspect angle whereby the target is observed is sufficiently wide, high resolution target images can be obtained by using CW radars [2], therefore allowing to reduce hardware costs. In a similar way, three dimensional radar imaging can be performed by coherently processing the backscattered field as a function of two rotation angles about two orthogonal axes [3]. Three dimensional target radar imaging can be efficiently obtained by means of a 3D Fourier Transform when the far-field (planar wave) approximation holds. Otherwise, the wavefront curvature has to be accounted for. In the chapter 1 an imaging algorithm based on a bi-static and near field spherical wave illumination was described. The algorithm has been developed under the MELISSA project. The system MELISSA is a body scanner whose purpose is the detection of concealed objects. The added value of the system is the capability to provide an electromagnetic image of the concealed objects.

## 2.2 system requirements and design

In this section, the imaging system requirements are assessed. The final application of the system should be the detection of concealed weapons, therefore one of the several applications of such system could be human safety operations in airport environment. The MMWs are suitable for this intent because they penetrate clothes and, at the same time, they are reflected by the human body and some potential concealed objects. The imaging requirements that the final system has to satisfy is that the resolution in any direction has to be less or at maximum equal to $1cm$. In the following an analysis for the system design is conducted.

### 2.2.1 Working frequency

In the working scenario in which the MELISSA system is thought to operate, the best applicants frequencies are in the $Kband$ of the electromagnetic spectrum. The choice has to be done between two possible operating frequencies, 35 $GHz$ or 16.5 $GHz$. In particular, the frequency has to be chosen by taking into account

- The spatial resolutions
- The number of elements of the receiving array

In fact, the spatial resolutions, both in the horizontal and vertical planes, are linearly dependent by the wavelength. Higher the frequencies are, finer the spatial resolutions became. Furthermore, in order to avoid the Grating lobes issue, the space among the elements of the receiving antenna has to be at maximum equal to $\lambda/2$. The imaging region whose the system has to scan and to reconstruct is about $2m$ in the vertical dimension, all the elements of the array have to receive the whole backscattered field by the target, for apply the SAR technique, this means that the array should have a length bigger or at least equal to $2m$. If the length of the array is $2m$ and the frequency is 35 $GHz$ (that correspond to a wavelength of $8.6mm$), the number of element with a step of $\lambda/2$ would be 465. Instead, in the case of the frequency 16.5 the required number of elements would be 220, about the half. The final operating frequency is going to be a trade-off between a simpler and cheaper hardware solution for the receiving array, and the deterioration of the spatial resolutions.

### 2.2.2 Distance between sensors and target: " the near field issue "

The mechanical structure that contains the hardware and the target (human being plus potential concealed objects) is called Shelter. Such element has to be enough large in order to contain the person and not to cause a sense of oppression and at the same time, it should be small enough to be portable and easily moved. For such reasons, the dimension of the shelter (fig. 2.1) are $2.70m$ of height, $2m$ of width and $2.70m$ of depth.

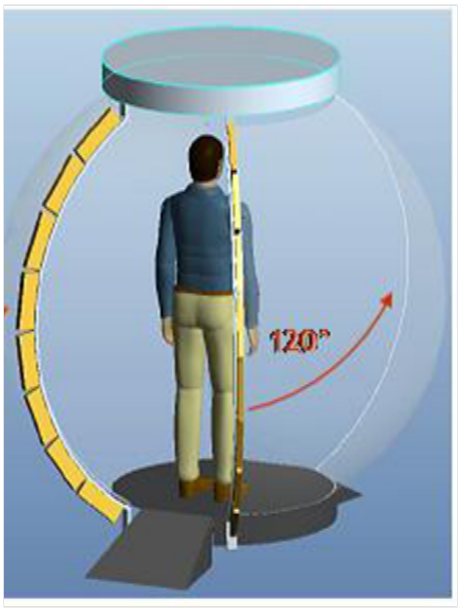


Figure 2.1: Representation of the shelter

Once the dimensions of the shelter has been designed, the distance between the sensors (transmitter and receiving array) are fixed, therefore, the far field condition can be analyzed. Conventionally, the far field condition [4] is satisfied if the eq. 2.1 is valid.

$$R > \frac{2D^2}{\lambda} \tag{2.1}$$

where $D$ is the maximum dimension of the radiating element (both from the point of view of the antenna or the target), $R$ is the distance of the observation point and $\lambda$ is the wavelength. Let consider the transmitter point of view, in such case $D$ is the maximum size of the radiating element of the antenna and R is the distance between target and transmitter. If a $\lambda/2$ dipole is used as radiating element, the maximum dimension is $D = 8.6mm@35GHz$ and

$D = 18.2mm@16.5GHz$. The radius of the shelter is equal to $1m$, the target is located in the center therefore the distance between target and transmitter is $R = 1m$. By substituting these values in the eq. 2.1, it can be easily verified that the far field condition, from the point of view of the transmitter, is valid for both the considered frequencies. The conclusion is that the target is in the far field region of the transmitter. Let consider now the more interesting case, that is the validity of the eq. 2.1 from the target point of view. When the receiving elements are considered, typically the target can be seen as an equivalent antenna that irradiates the incident field. In such case, $D$ is the maximum dimension of the target and $R$ is the distance between target and receiver. Now the values are $D = 2m$, $R = 1$, if they are putted in the eq. 2.1 it can be verified that the condition is not satisfied. By inverting the equation 2.1, the maximum dimension of the target for which the condition would be verified can be calculated, as shown in eq. 2.2

$$\begin{aligned} D &\cong 6.56cm@35GHz \\ D &\cong 9.54cm@16.5GHz \end{aligned} \tag{2.2}$$

In conclusion, the receiving array is not in the far field region of the target, this implies that the incident wavefront on the array cannot be considered as plane but it is a spherical wavefront. As consequence, conventional SAR techniques cannot be utilized for the imaging purpose, but a new algorithm has to be designed (see section 1.1) in order to take into account the near filed condition.

### 2.2.3 Geometric resolutions

As can be figured out from the fig.1.2 of the section 1.1, the geometry is a bi-static configuration. In fact, the array is composed by only one radiating element, located in the center of the array, and by $n_a$ receiving dipoles, far apart of $\lambda/2$. As already stated in the previous section 2.2.2, the receiving array is in the near field region of the target, moreover the aspect angle variation (i.e. the variation of the view angle in which the target is seen by the array) is large. As consequence, the conventional theory for spotlight SAR [5]- [6], cannot be applied for the calculation of the geometric resolutions.

#### Vertical resolution

The vertical resolution can be approximately evaluated in the spatial frequencies domain, as the inverse of the dimension of the region in which the received signal is defined. Let consider the figure 2.2

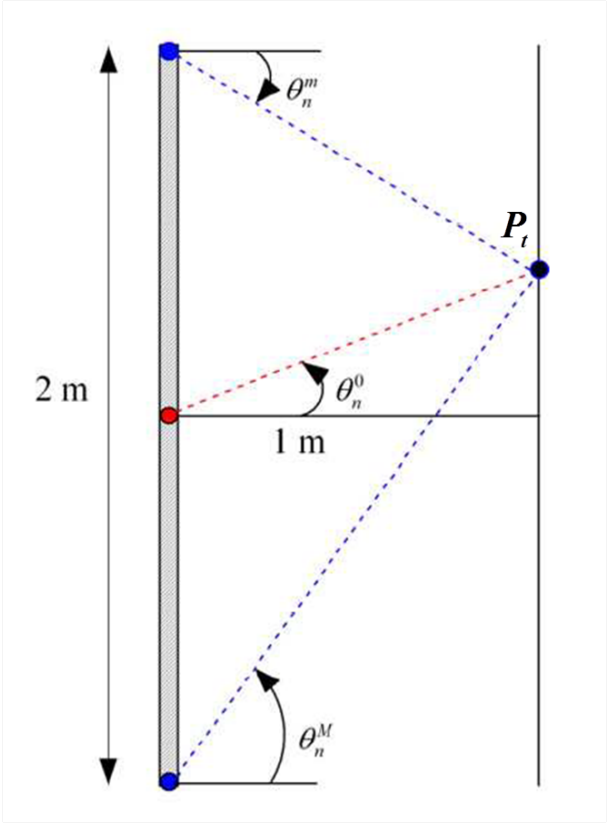


Figure 2.2: Geometry for calculate the vertical resolution: mono-static case

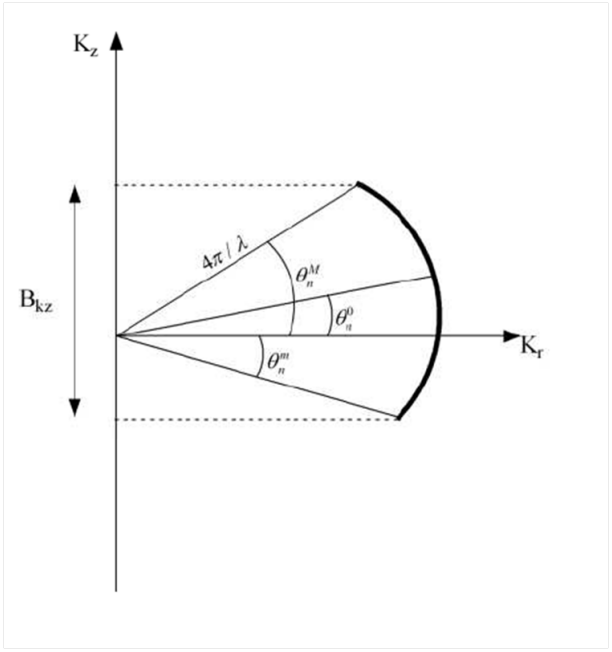


Figure 2.3: Signal representation in the frequencies spatial domain: mono-static case

In fig. 2.2 the geometry for the calculation of the vertical resolution is shown. The antenna receiver is a linear array of 2 m of length, the two more external sensors are indicated with a blue filled circles, the point $P_t$ is a generic scatterer belonging to the scene to reconstruct. The angle $\theta_n^0$ is the angle of view with whom the sensor in the middle position of the array observes the point $P_t$. $\theta_n^M$ and $\theta_n^m$ are respectively the maximum and the minimum angles of view. Let assume that all the elements of the array are receiving elements, in this condition the occupancy of the signal in the spatial frequencies domain is that of fig. 2.3 and the resolution along the vertical coordinate, in the mono-static case, can be approximated as in eq. 2.3.

$$D \cong \frac{2\pi}{B_{kz}} = \frac{\lambda}{4[\sin(\theta_n^M) - \sin(\theta_n^m)]} \tag{2.3}$$

For the bi-static case, it would be more complicated to calculate the vertical resolution, nevertheless the Bistatically equivalent monostatic (BEM) [8]

geometry can be defined. As stated in [8] an equivalent mono-static sensor can be thought in the direction of the bisector of the bi-static angle. The figure 2.4 shows the geometry used for the calculation of the vertical resolution in the bi-static case.

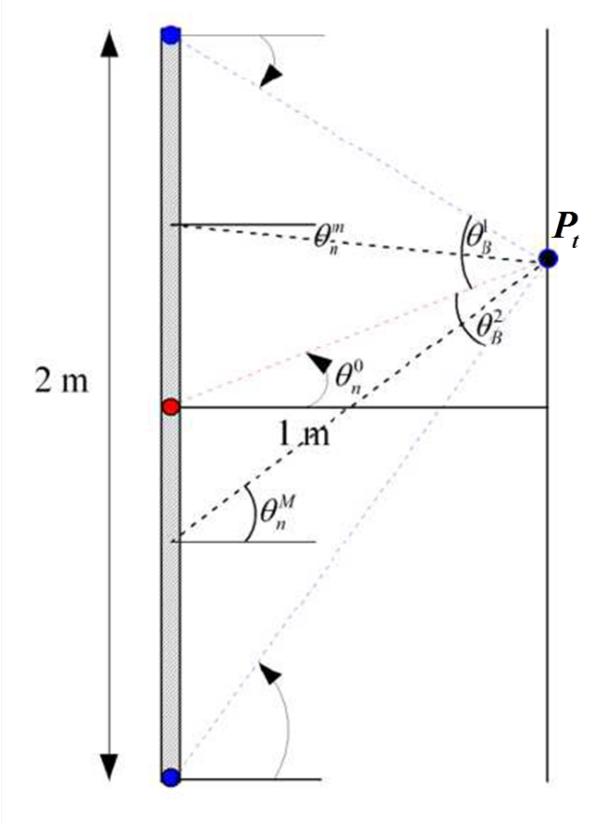


Figure 2.4: Geometry for calculate the vertical resolution: bi-static case

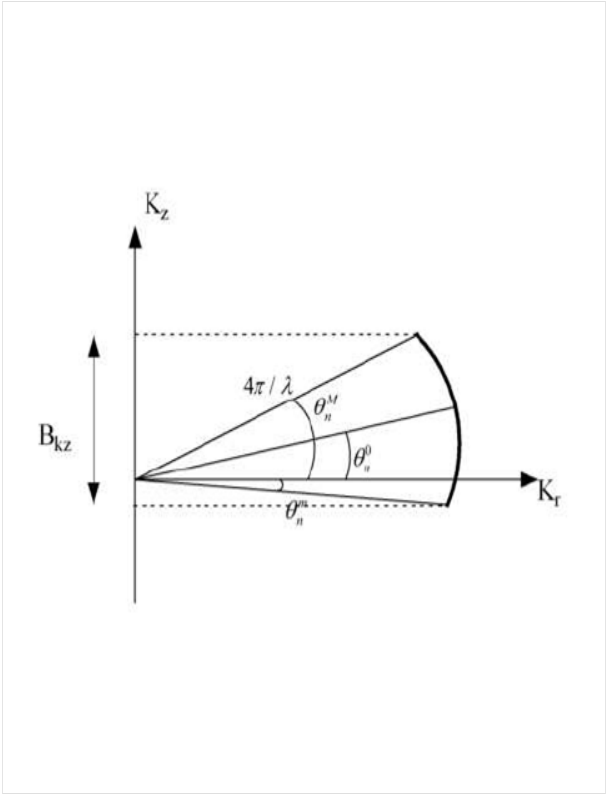


Figure 2.5: Signal representation in the frequencies spatial domain: bi-static case

In fig. 2.4 the angles $\theta_n^M$ and $\theta_n^m$ are now, respectively, the maximum and minimum angles of view of the two equivalent mono-static sensors located on the bisector of the bi-static angles $\theta_B^2$ and $\theta_B^1$, concerning the two external sensors. The signal in the spatial frequencies domain is shown in the figure 2.5. Just for providing a numerical example of the spatial and frequency variability of the vertical geometric resolutions, in tab. 2.1 and tab. 2.2 are calculated, respectively, the theoretical resolutions for a scatterer located in the position (0,0,0) and for another scatterer in the potion (0,0,1), by varying the frequency, in both the mono-static and bi-static case.

| | mono-static | Bi-static |
|---|---|---|
| $f_0 = 16.5GHz$ | $6.36mm$ | $11mm$ |
| $f_0 = 35GHz$ | $3mm$ | $5.6mm$ |

Table 2.1: Vertical resolutions: scatterer in (0,0,0)

| | mono-static | Bi-static |
|---|---|---|
| $f_0 = 16.5GHz$ | $10mm$ | $21mm$ |
| $f_0 = 35GHz$ | $4.8mm$ | $10mm$ |

Table 2.2: Vertical resolutions: scatterer in (0,0,1)

### Horizontal resolution

Typically, bi-dimensional SAR images of targets with high resolutions are obtained by transmitting wide band signals and by exploiting the relative movement between the antenna and the target. Therefore, wide bands are necessary for achieving high range resolutions, whereas high cross range resolutions are obtained by coherently integrating the received signals for different aspect angles. Notwithstanding, theoretical results [2] assess that bi-dimensional images with high spatial resolutions can be also obtained by transmitting only one frequency but by observing the target around different angular directions, in the range $[0, 2\pi]$. The theoretical spatial resolutions cannot be calculated in a closed form, other than which in one case that will be considered in the following. The reasons are:

- The system is spatial variant, therefore the PSF and as consequence the resolutions depend on the point where the target is
- The geometry is bi-static, so the vertical resolutions also depend on the bi-static angle, whom it changes according the different couple transmitter-receiver that is taken into account.
- In order to reduce the mutual coupling between the transmitter and the receivers, they could be separated by interposing an absorbent panel among them. In this situation, the geometry would be bi-static also in the horizontal plane, further complicating the geometry and then calculating the resolutions.

The bi-static geometry, both in the vertical and horizontal plane, will be studied in the following.

### Signal model

Let assume that the target is small enough in relation to the distance between the target and the transmitter, for a couple formed by the transmitter and one of the receivers, and in the case that the geometry of the system is

as illustrated in fig.1.1, that is with the transmitter aligned at the receiving array, the received signal [2] can be written as in eq. 2.4

$$s_r = \iint_{(x,y)} f(x,y) e^{-j\frac{4\pi}{\lambda}(x\cos(\phi)+y\sin(\phi))}\,dx\,dy = \iint_{(x,y)} f(x,y) e^{-j2\pi(xX+yY)}\,dx\,dy \tag{2.4}$$

where $X = \frac{2}{\lambda}\cos(\phi)$ and $Y = \frac{2}{\lambda}\sin(\phi)$. As can be figured out from the eq.2.4, the received signal $s_r$ can be calculated by means of a 2D Fourier Transform (FT) of the reflectivity function $f(x,y)$, calculated on a circumference of radius equal to $\frac{2}{\lambda}$ . The FT of the PSF of the system can be defined as in eq. 2.5

$$H(X,Y) = \delta(\sqrt{(}X^2+Y^2) - \frac{2}{\lambda}) \tag{2.5}$$

The received signal 2.4 can be re-written as the product between the FT of the reflectivity function and the PSF.

$$S_r(X,Y) = F(X,Y)\cdot H(X,Y) \tag{2.6}$$

Finally, the PSF of the system can be calculated as an Inverse Fourier Transform (IFT) of the eq. 2.5, and in polar coordinates it becomes 2.7

$$h(\rho,\theta) = \frac{4\pi}{\lambda} J_0\left(\frac{4\pi}{\lambda}\rho\right) \tag{2.7}$$

The eq. 2.7 assesses that an ideal scatterer (isotopic and point-like) located in the center of the reference system has a PSF equal to a zero order Bessel function [2], so it has a spatial resolution equal to $\delta\rho \cong 0.2\lambda$, in both directions in the horizontal plane. Fig.2.6 shows the reconstructed image in the horizontal plane obtained by using the algorithm of the section 1.1, of an ideal point located in the center of the reference system and observed for an angle of $2\pi$.

As already stated, the PSF is spatial variant, so for the scatterers very close to the center of the system and scanned for an angle equal to $2\pi$, the PSF is that of fig.2.6 and the resolution in the horizontal plane can be calculated in a closed form by using the eq. 2.7. Otherwise, in all other cases, the resolutions change by moving away from the center of the system, the eq.2.7 is not more valid so it is not possible to calculate the resolutions in a closed form, moreover, the PSF loses its circular symmetry and as consequence, the resolutions in the horizontal plane are different between the $x$ and $y$ axis. Anyway, the horizontal resolutions are related to the size of the region where the received signal is defined, in the frequencies spatial domain. moreover, the resolutions in both the horizontal dimensions, can be evaluated by approximating the arc

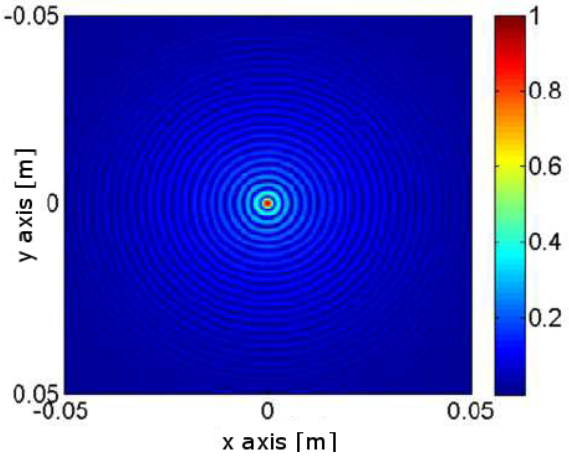


Figure 2.6: PSF in the horizontal plane of an ideal scatterer in (0,0,0)

in the frequencies domain as a rectilinear segment. Finally, the resolutions are evaluated as the inverse of the arc length in both directions, as illustrated in fig. 2.7

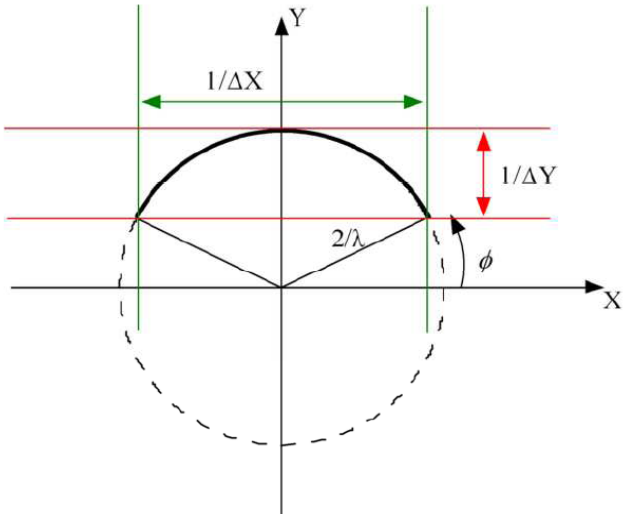


Figure 2.7: Signal representation in the spatial frequencies domain, if just one frequency is transmitted

The figure 2.7 illustrates the situation in which the CW transmitter only one frequency transmits. If a stepped frequency technique is adopted, or more in general, a bandwidth signal is transmitted, the above mentioned consideration are still valid. In particular, the region in the spatial frequencies domain

where the signal is defined will become a circular crown, instead of an arc, as in the single frequency case.

**Signal model: Bi-static geometry both in vertical and horizontal plane**

As already mentioned before, if the transmitter is separated from the line of the receiving array, the geometry becomes bi-static also in the horizontal plane. The reason for which the sensors might be separated would be because we would like to reduce the mutual coupling between the transmitting antenna and the receivers. Retracing the equations from 2.4 to 2.7, we now calculate the PSF of the system, by considering a scatterer located in the origin of the reference system, in the case of a bi-static geometry both in vertical and horizontal plane.

$$s_r = \iint_{(x,y)} f(x,y) e^{-j\frac{4\pi}{\lambda}K(x\cos(\phi)+y\sin(\phi))}\,dx\,dy = \iint_{(x,y)} f(x,y) e^{-j2\pi(xX+yY)}\,dx\,dy \tag{2.8}$$

where $X = \frac{2}{\lambda}K\cos(\phi)$ and $Y = \frac{2}{\lambda}K\sin(\phi)$. In this case, yhe spatial frequencies are multiplied by a factor $k$ that is given by the eq: 2.9

$$K = \cos\left(\frac{\theta_B}{2}\right) \tag{2.9}$$

The factor $K$ [8], depends on the bi-static angle $\theta_B$, and it causes a distortion of the spatial frequencies and therefore a worsening of the spatial resolutions. The PSF of the system becomes now 2.10.

$$h(\rho,\theta) = \frac{4\pi}{\lambda}K J_0\left(\frac{4\pi}{\lambda}\rho\right) \tag{2.10}$$

Therefore, the spatial resolutions can be evaluated as $\delta\rho \cong \frac{0.2\lambda}{K}$.

### 2.2.4 Volume of focus

In the conventional SAR system, the focusing operation is performed onto an area around one scatterer, called as focusing point. The focusing procedure consists in the removal of the contribute concerning to the relative movement between the antenna and the focusing point, in the phase of the received signal. The phase term is perfectly compensated, that is removed, just for the focusing

point. For all the other scatterers close to such point, an error phase has to be taken into account. Such phase error can be considered as negligible if it is less then $\pi/2$. This criterion suggests a way for defining the focusing region [5] as 2.11

$$V_0 = \left\{ \mathbf{x} : \left| \frac{\mathbf{2}\pi}{\lambda}(\mathbf{R_{T,x}}(\phi, \zeta_\mathbf{3}) + \mathbf{R_{R,x}}(\phi, \zeta_\mathbf{3})) - \frac{\mathbf{2}\pi}{\lambda}(\mathbf{R_{T,0}}(\phi, \zeta_\mathbf{3}) + \mathbf{R_{R,0}}(\phi, \zeta_\mathbf{3})) \right| \leq \frac{\pi}{\mathbf{2}} \right\} \tag{2.11}$$

In the eq. 2.11, $\mathbf{x}$ is the position vector of the considered point in the space, $R_{T,x}$ and $R_{R,x}$ are respectively, the distances between a point belonging to the focusing area with the transmitter and the same point with the receiver. Moreover, $R_{T,0}$ and $R_{R,0}$ are the distances between the focusing point with the transmitter and the focusing point with the receiver.

### 2.2.5 Radiometric resolution

The radiometric resolution or the *radiometric resolving limit* is the minimum difference of intensity that a sensor is able to detect. In other words, it defines the system capacity to discriminate objects with similar electric permeability coefficients and therefore with similar reflectivity coefficients at the microwaves. For our purpose, the MELISSA system should be able to detect concealed objects with reflectivity property very close to those of the human skin, as for instance, plastics, liquids and powders. The radiometric resolution is determined by:

- the coherent integration time of the sensors. In the final design of the system, the scan time and the number of array elements have to be dimensioned also by considering the radiometric resolving limit requirement.
- the analog digital converter. The number of bits used for the signal representation influence on the quantization noise.
- the imaging algorithm used for the reconstruction. An imaging algorithm reconstructs the reflectivity function of the target after the convolution with the PSF of the system. As consequence, the side lobes level could influence the backscattered signal coming from those low reflecting materials.

The latter interference, that significantly affects the radiometric resolution, is very difficult to calculate in theory, because the PSF is space variant, because it depends on the scan angle and it also depends on the receiving array size.

### 2.2.6 Criteria for Sampling in Frequency, Azimuth and Vertical coordinate

In this section are discussed the criteria for the sampling in the scan angle direction ($\phi$) and in the vertical direction ($\zeta$), in order to avoid aliasing errors. Furthermore, a criterion for the sampling in frequency is performed, in case that for the final system design it decides to transmit a bandwidth signal and not only a monochromatic signal. The idea is to evaluate the maximum spectral occupancy of the received signal in each conjugate domain, and to apply the Nyquist's sampling criterion for each one of them. Let assume the target composed by a sum of point-like scatterers, so the received signal can be though as a sum of complex oscillations ($e^{-j2\pi f T_f}$), where each one of them identifies a point of coordinate $(\rho_p, \theta_p, \zeta_p)$ on the target. The variables $f$ and $T_f$ are respectively the frequency and the delay time of the considered point. These two variables are each the conjugate of the other in the Fourier domain. In the case of the transmitter jointly liable with the array receiver, the coordinates of the radiating element are $(R, \phi, 0)$ while the coordinates of the receiving array are $(R, \phi, \zeta)$, therefore the distances between the point and the transmitter and receiver are, respectively 2.12

$$\begin{aligned} R_T &= \sqrt{R^2 + \rho_p^2 - 2R\rho_p \cos(\phi - \theta_p) + \zeta_P^2} \\ R_R &= \sqrt{R^2 + \rho_p^2 - 2R\rho_p \cos(\phi - \theta_p) + (\zeta - \zeta_P)^2} \end{aligned} \tag{2.12}$$

Let define the phase of the signal as $\Psi(f, \phi, \zeta) = 2\pi \frac{f}{c}(R_T + R_R)$

#### Sampling in angle

The conjugate variable of $\phi$ in the Fourier domain, that represents the phase variation due to the changing of the angle in the azimuth direction $\phi$, is equal to 2.13

$$f_\phi = \frac{1}{2\pi} \frac{\partial \Psi(f, \phi, \zeta)}{\partial \phi} = \frac{f}{c} R\rho_p \sin(\phi - \theta_p) \left[ \frac{1}{R_T} + \frac{1}{R_R} \right] \tag{2.13}$$

The maximum and minimum values of $f_\phi$ define the maximum spectral occupancy of the signal in the conjugate domain of $\phi$.

The signal is a pass band like with a spectral occupancy $B_\phi = f_{\phi max} - f_{\phi min}$, so by applying the Nyquist sampling frequency criterion for pass band signals

we get that the spacing in angle should be 2.14

$$\Delta\phi \leq \frac{1}{B_\phi} \tag{2.14}$$

### Sampling in the vertical dimension

The conjugate variable of $\zeta$ in the Fourier domain, that represents the phase variation due to the changing of the high in the vertical direction $\zeta$, is equal to 2.15

$$f_\zeta = \frac{1}{2\pi}\frac{\partial\Psi(f,\phi,\zeta)}{\partial\zeta} = \frac{f}{c}\frac{\zeta-\zeta_P}{R_R} \tag{2.15}$$

The maximum and minimum values of $f_\zeta$ define the spectral occupancy of the signal in the conjugate domain of $\zeta$.

The signal is a pass band like with a spectral occupancy $B_\zeta = f_{\zeta max} - f_{\zeta min}$, so by applying the Nyquist sampling frequency criterion for pass band signals we get that the spacing in angle should be 2.16

$$\Delta\zeta \leq \frac{1}{B_\zeta} \tag{2.16}$$

### Sampling in frequency

In the case of a radiating element transmitting a bandwidth signal like a stepped frequency waveform, a sampling criterion has to be formulate. The conjugate variable of $f$ in the Fourier domain, that represents the phase variation due to the changing of the transmitted frequency $f$, is equal to 2.17

$$T_f = \frac{1}{2\pi}\frac{\partial\Psi(f,\phi,\zeta)}{\partial f} = \frac{R_T+R_R}{c} \tag{2.17}$$

The maximum and minimum values of $T_f$ define the spectral occupancy of the signal in the conjugate domain of $f$.

$$B_{T_f} = T_{fmax} - T_{fmin} = \frac{(R_T+R_R)|_{max} - (R_T+R_R)|_{min}}{c} \tag{2.18}$$

where $(R_T+R_R)|_{max}$ means the maximum bi-static distance of the couple transmitter-receiver, from a point $\zeta_p$ on the target. The signal is a pass band

like with a spectral occupancy $B_{T_f}$, so by applying the Nyquist sampling frequency criterion for pass band signals we get that the spacing in the frequency domain should be 2.19

$$\Delta f \leq \frac{1}{B_{T_f}} \tag{2.19}$$

## 2.3 System Analysis and Design

Previously, in section 2.2, a theoretical treatment of the main system requirements have been done. Particularly, the near field issue, the geometric and radiometric resolutions, the the depth of focus, the working frequency and the sampling criteria have been analyzed. In this section, all these aspects are deeply analyzed with the help of numerical simulations and further elements for the system design are going to be assessed.

### 2.3.1 Antenna Design

The sensor has to illuminate the whole human body and it has to receive the backscattered signal from the potential concealed targets, located on it. The sensor is composed by only one transmitting antenna element and an array of $N_a$ receiver antenna elements. Concerning the transmitter, the waveform to transmit will be designed in the next section and, the hardware design is out of the purpose of this work, it is enough for us to asses that it must illuminate the whole human body, so a requirement could be a wide beam width in the vertical plane. Concerning the receiver, each single element must have a beam width big enough in order to receive the backscattered signal from the whole human body. The vertical movement in order to apply the SAR technique is simulated by means of a time multiplexing of the single elements. In other words, when an element acquires the signal for a time slot, all the others are switched off. The goal of this paragraph is to design the number of antenna elements of the receiving array, the spacing of them and the antenna size in the vertical plane. Particularly, the spacing among all the single elements has to be $\lambda/2$ [9], in order to avoid the interferences in the construction of the beam, also known as grating lobes. The number of the elements and the antenna size in the vertical plane depend on the requirements in term of the geometric resolutions of the system. For the MELISSA system the following requirements have to be satisfied:

- the geometric resolutions must be less than $1cm$ in any dimension.

- the spacing among the elements is $\lambda/2$.
- because of the shelter size (section 2.2.2), the human body is at $1m$ of distance from the sensor.
- the region of interest that has to be reconstructed is about $2m$ in the vertical dimension, due to the fact that the standard height of a human being do not exceed $1.90m$.

Starting from the above listed requirements, the number of elements can be designed, as figure 2.8 shows.

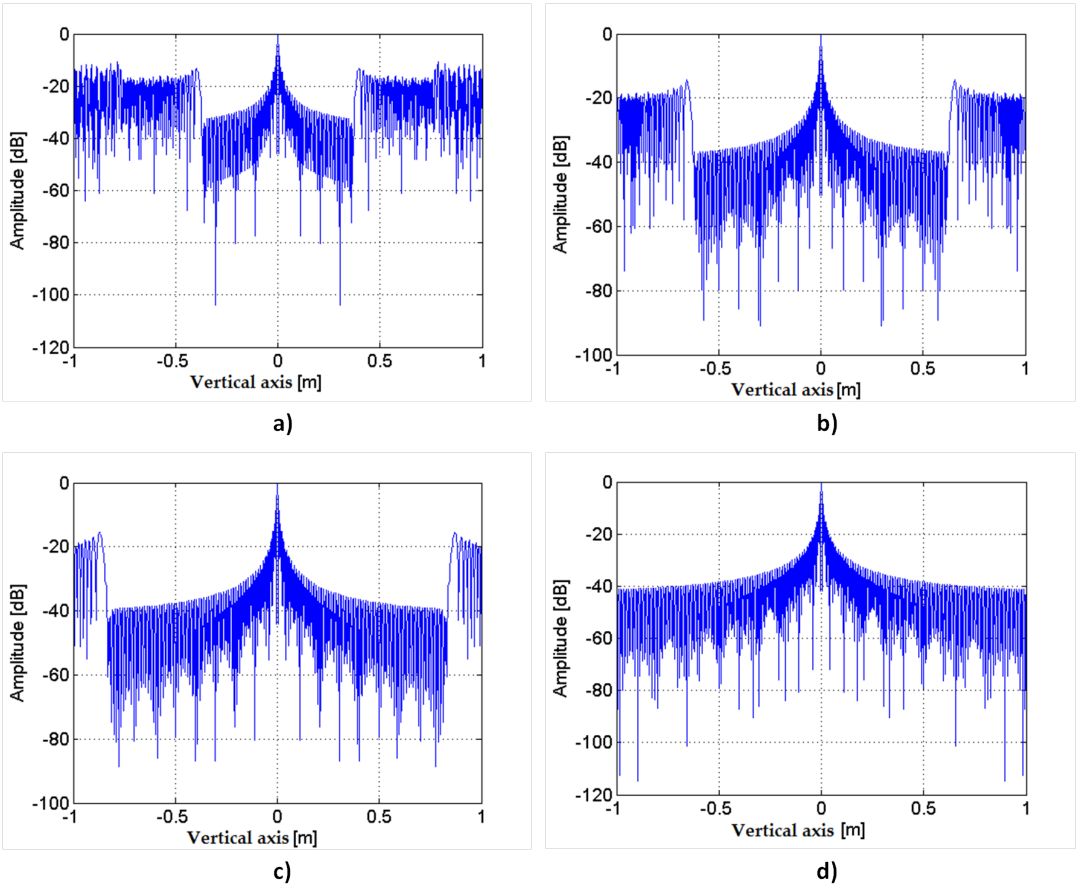


Figure 2.8: Vertical profile by varying the number of antenna elements: a) #91 elements, b) #151 elements, c) #201 elements, d) #251 elements

From the figure 2.8 can be figured out that, if we would like to reconstruct an area of $2m$ in the vertical plane, we should use a receiving array with at

least 251 antenna elements, in order to be sure that no interferences occur. Since the MELISSA system requires a reconstruction area just of $2m$ in the vertical size, we decide to use an array of 256 antenna elements spaced of half of the wavelength.

### 2.3.2 Spatial frequencies analysis

In this section is going to be demonstrated through numerical simulations that the PSF is spatially dependent. It is done by analyzing the received signal in the spatial frequencies domain in different focusing points belonging to the target, figures 2.9-2.10.

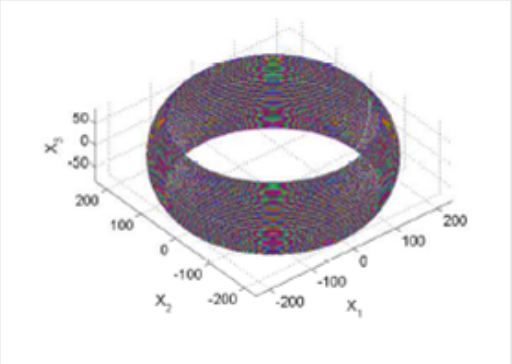


Figure 2.9: Spatial frequencies domain of the focusing point in (0 cm, 0 cm, 0cm)

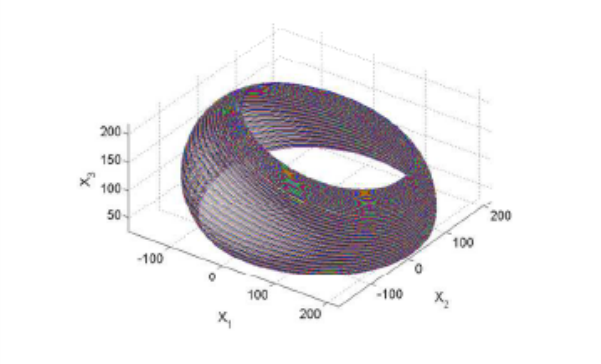


Figure 2.10: Spatial frequencies domain of the focusing point in (50 cm,40 cm, 70cm)

Both figures have been obtained by simulating a scan angle equal to $2\pi$, if it is less than $2\pi$, the domain is only a portion of that shown in figures 2.9 and 2.10.

### 2.3.3 Geometric resolutions analysis

#### Vertical resolutions

In this section the geometric resolution in the vertical plane is evaluated by simulating a system geometry as shown in figure 1.1. The scan angle is $\alpha = 2\pi$, the vertical resolution is calculated for two different focusing points of coordinates (0,0,0) and (0,0,1m), in order to evaluate the loss of resolution between the scatterer located in the centre of the system and the farthest scatterer of the imaging volume. The whole reconstructed imaging volume is $2m$ of length in the vertical dimension. The array size is $2m$, therefore if a frequency of $35GHz$ is used, the number of antenna elements should be equal

to 465, instead if a frequency of $16.5GHz$ is used, the number of the antenna elements should be equal to 221. The theoretical vertical resolutions are given by the equation 2.3. In figure 2.11 the vertical resolution at $-3dB$ for the scatterer located in the centre of the system, in the case of $f_0 = 35GHz$ and $f_0 = 16.5GHz$, is calculated.

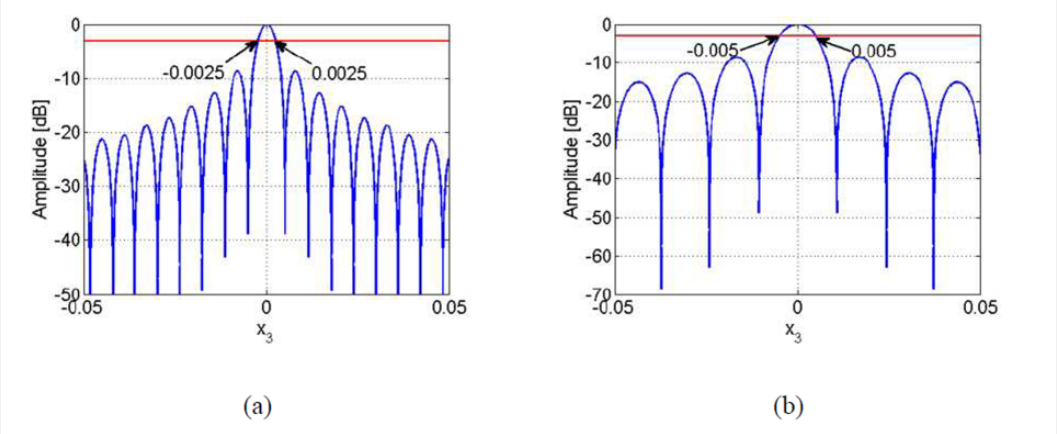


Figure 2.11: Vertical profile of the point of coordinate (0,0,0) with a) $f_0 = 35GHz$ b) $f_0 = 16.5GHz$

In figure 2.12 the vertical resolution at $-3dB$ for the farthest scatterer of the imaging volume, in the case of $f_0 = 35GHz$ and $f_0 = 16.5GHz$, is also shown.

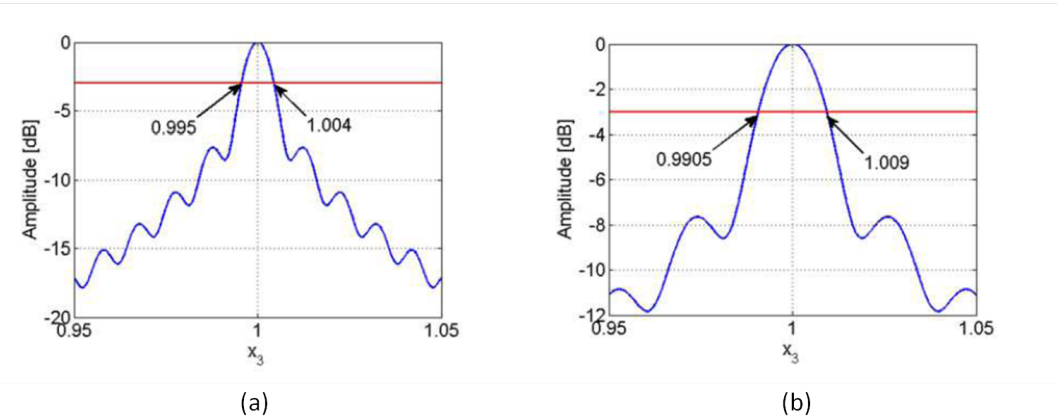


Figure 2.12: Vertical profile of the point of coordinate (0,0,1) with a) $f_0 = 35GHz$ b) $f_0 = 16.5GHz$

The vertical resolutions that can be figured out from the figures 2.11 -2.12 are listed in the table 2.3.

| | (0,0,0) | (0,0,1) |
|---|---|---|
| $f_0 = 35GHz$ | $5mm$ | $9mm$ |
| $f_0 = 16.5GHz$ | $10mm$ | $19mm$ |

Table 2.3: Vertical resolutions at $-3dB$

Comparing the figures 2.11 and 2.12 the following considerations can be done:

- The array factor is a sinc like function in the Broadside direction, instead this is not still true in the End-fire direction. In fact, the figure 2.11 shows that for the scatterer $(0, 0, 0)$, the vertical profile has the typical behavior of a sinc function, instead the figure 2.12 confirms as this is not valid for the scatterer (0,0,1), located at the extreme side of the imaging volume. It's worth noting that the Side Lobe Level (SLL) is slightly higher than $-13dB$, typical value of a sinc function.

- The calculated vertical resolutions are very close to the theoretical of table 2.1 and 2.2 )

- The vertical resolutions obtained by using a working frequency of $16.5GHz$ are about twice of that obtained with a frequency of $35GHz$.

**Horizontal resolutions**

As already stated in the section 2.2.3, the horizontal resolutions in a closed form can be only calculated for a scatterer located in the origin of the reference system and by scanning an angle of $2\pi$. In this section, the PSF in the horizontal plane for scatterers located in different points in the imaging volume are analyzed, furthermore simulations with different scan angles are performed in order to validate the previously presented theoretical results and to valuate the loss of resolutions that occurs if a smaller scan angle than $2\pi$ is used. Figure 2.13 shows the PSF of the point of coordinate $(0, 0, 0)m$, instead figure 2.14 shows the PSF of the point of coordinate $(0.5, 0.4, 0.7)m$. Both figures have been obtained by using two working frequencies, $35GHz$ and $16.5GHz$, by scanning an angle of $2\pi$. The inner black circle in both figures, indicate the level at $-3dB$.

The horizontal resolutions at $-3dB$ that can be figured out from the figures 2.13 and 2.14 are listed in the table 2.4. According to the theoretical horizontal resolutions, $(\delta_\rho = 0.19\lambda)$, a point located in the centre of the reference system provides the following results: $\delta_{x1}|@35GHz = \delta_{x2}|@35GHz \cong 1.634mm$ and $\delta_{x1}|@16.5GHz = \delta_{x2}|@16.5GHz \cong 3.4mm$.

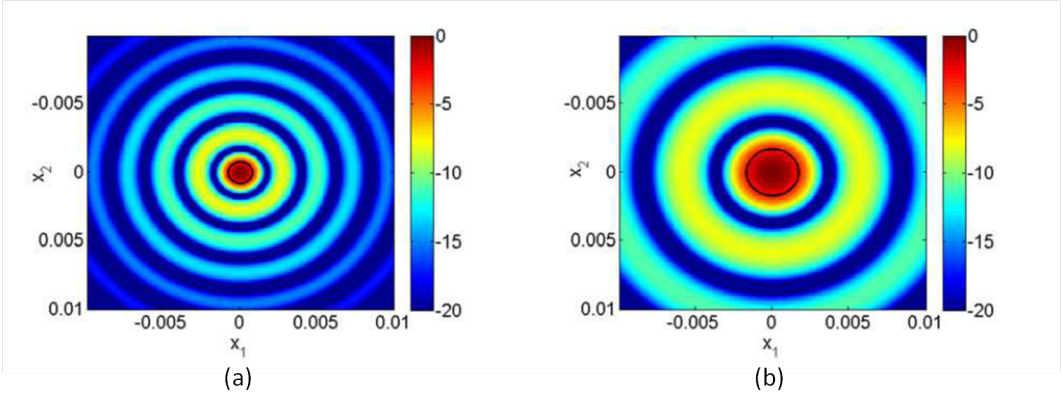


Figure 2.13: PSF in the horizontal plane of the scatterer (0,0,0) by scanning an angle of $2\pi$, with a) $f_0 = 35GHz$ b) $f_0 = 16.5GHz$

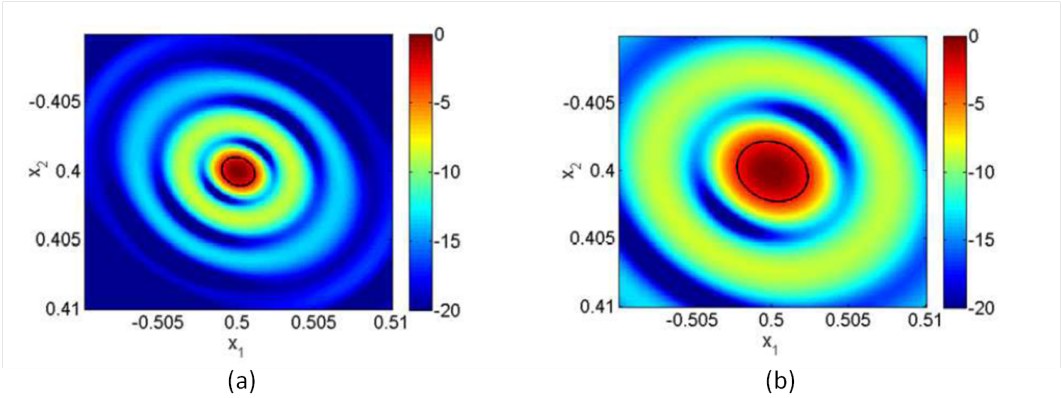


Figure 2.14: PSF in the horizontal plane of the scatterer (0.5,0.4,0.7) by scanning an angle of $2\pi$, with a) $f_0 = 35GHz$ b) $f_0 = 16.5GHz$

Obtained data confirms that the theoretical resolution is very close to the simulated one. Furthermore, the PSF in the horizontal plane changes depending on the considered point in the imaging volume, as consequence also the spatial resolutions change.

In the section 2.2.3 is discussed how to calculate the geometric resolutions for a scan angle along the horizontal direction smaller than $2\pi$. In the following, some simulations with a scan angle equal to $\alpha = 2/3\pi$ are provided. The simulation geometry is that of figure 2.15.

The resolutions are valued as the $-3dB$ value of the PSF main lobe and they are compared with the values obtained by approximating the arc in the spatial frequency domain with a straight line, as previously stated.

As can be noted from the figures 2.17,2.16 the main axis of the obtained

| | | (0,0,0) | (0.5,0.4,0.7) |
|---|---|---|---|
| $\alpha = 2\pi$ | $f_0 = 35GHz$ | $\delta_{x1} = 1.6mm$<br>$\delta_{x2} = 1.6mm$ | $\delta_{x1} = 2.2mm$<br>$\delta_{x2} = 2.2mm$ |
| $\alpha = 2\pi$ | $f_0 = 16.5GHz$ | $\delta_{x1} = 3.5mm$<br>$\delta_{x2} = 3.5mm$ | $\delta_{x1} = 4.6mm$<br>$\delta_{x2} = 4.6mm$ |

Table 2.4: Horizontal resolutions at $-3dB$

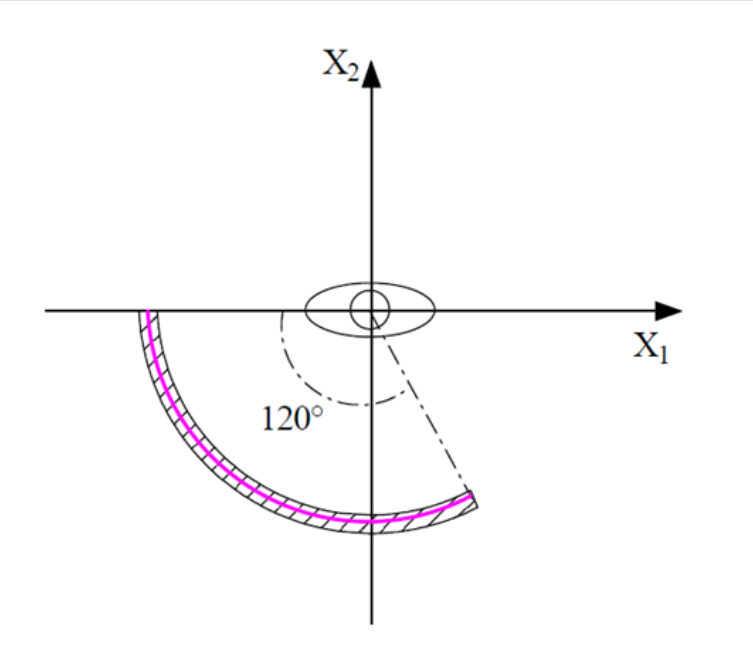


Figure 2.15: Simulation geometry: the transmitter (colored line) moves jointly with the receiver.

PSF are differently oriented respect the axis $x_1$ and $x_2$. This occurs because of the geometry, particularly it has to be referred to the array initial position. In this case, the $x_1$ coordinate at the beginning is equal to $x_1 = -1$, therefore the scanning geometry is asymmetric for the $x_2$ axis. The resulting geometry in the spatial frequency domain in that shown in figure 2.18.

From the figure 2.18 can be noted as the two reference systems $(X_1, X_2)$ and $(X_1', X_2')$ differ of 30° each other, therefore the PSF(red ellipsoid in 2.18) gets finer resolutions along the axis $x_1$. The horizontal spatial resolutions of the two reference systems can be evaluated as one over the size of the spectral domain along the axis $X_1, X_2$ and $X_1', X_2'$. The theoretical spatial resolutions against those measured as the values at $-3dB$ of the PSF main lobe are listed in the table 2.5.

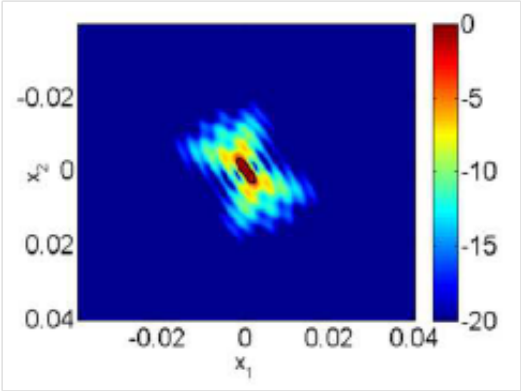


Figure 2.16: Horizontal PSF with a scan angle of 120°@35$GHz$

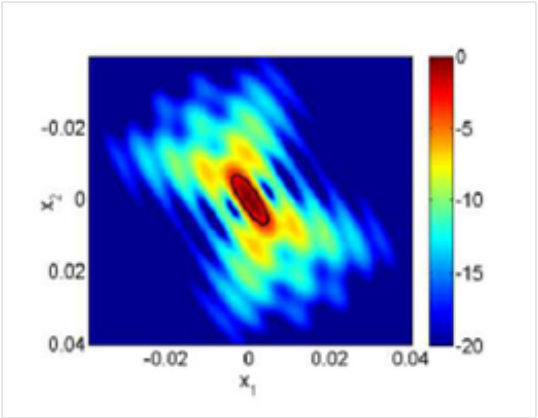


Figure 2.17: Horizontal PSF with a scan angle of 120°@16.5$GHz$

| | Theoretical | | $-3dB$ | |
|---|---|---|---|---|
| $f_0 = 35GHz$ | $\delta_{x1} = 2.8mm$ | $\delta_{x1'} = 2.5mm$ | $\delta_{x1} = 2.5mm$ | $\delta_{x1'} = 2.2mm$ |
| | $\delta_{x2} = 4.9mm$ | $\delta_{x2'} = 8.6mm$ | $\delta_{x2} = 4.0mm$ | $\delta_{x2'} = 7.5mm$ |
| $f_0 = 16.5GHz$ | $\delta_{x1} = 6.0mm$ | $\delta_{x1'} = 5.1mm$ | $\delta_{x1} = 5.6mm$ | $\delta_{x1'} = 5.0mm$ |
| | $\delta_{x2} = 10mm$ | $\delta_{x2'} = 18mm$ | $\delta_{x2} = 8.8mm$ | $\delta_{x2'} = 16mm$ |

Table 2.5: Horizontal resolutions at $-3dB$ Vs theoretical resolutions

### 2.3.4 Radiometric resolutions analysis

The radiometric resolution determines the capability of the algorithm to detect different kind of materials. Each material has its answer in terms of scattered electric field, for instance the human body skin scatterers differently respect potentially concealed weapons under or over it. We are only interested on the reflected field, so the transmitted field though the target cannot be taken into account, further more we consider non magnetic materials so each object can be only modeled by means of the real part of its relative electric permettivity $\Re\{\xi_r(f)\}$. Assuming this kind of model, the radiometric resolution becomes for us the minimum variation of $\xi_r(f)$ able to produce a contrast in the reconstructed image. For a surface plane of dielectric material on whom impact a plane wave with a polarization parallel to such surface, the reflection coefficient can be defined as 2.20

$$R = \frac{|E_r|}{E_t} = \frac{|1-n|}{|1+n|} \tag{2.20}$$

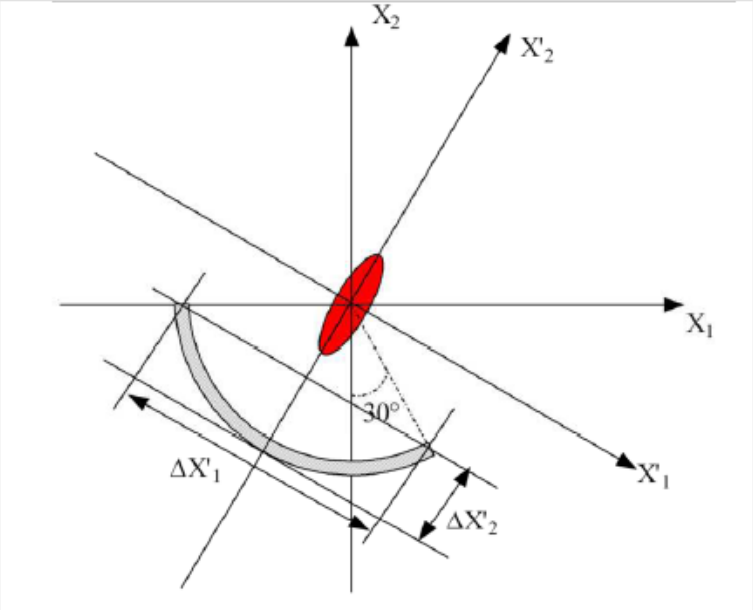


Figure 2.18: Signal representation in the spatial frequency domain for a scanning angle of 120°

where $n = \sqrt{\xi_r}$ is the refraction index. By putting the reflection coefficient of eq.2.20 in the model of the received signal of eq.1.1, a target composed by a particular kind of material can be simulated. We simulate a plane composed by several point like scatterers with a reciprocal distance of $\lambda/4$ and an amplitude equal to $R$. This model is valid only for surfaces small enough and located in the origin of the reference system such that the incident wave can be approximated as plane. In order to evaluate the radiometric capability of the algorithm, a target with reflection properties similar to the human skin has been simulated, furthermore others materials as plastic (PolypropylenePolypropylene (PP)), explosive (Triamino-Trinitobenzene Triamino-Trinitobenzene (TATB)) and a perfect conductor (acPEC) have been simulated and overlapped to the former. In tab. 2.6 are listed the dielectric materials properties existing in literature [10–12] for frequencies close to $16GHz$ that have been utilized for evaluate the contrast in the reconstructed image of figure 2.19.

As can be figured out from the figure 2.19, the algorithm can well detect different materials as Perfect Conductor (PEC) over skin, TATB over skin and PP over skin. Furthermore, from the image can be seen that the PEC material scatterers more than the explosive and the latter scatters more than the plastic.

| Material | Relative Permittivity $\xi_r$ |
|---|---|
| Skin(dry)@16.5$GHz$ | 24.995 |
| Polypropylene@9.4$GHz$ | 2.26 |
| TATB@16$GHz$ | 3.8 |
| Metallo PEC | - |

Table 2.6: Dielectric properties

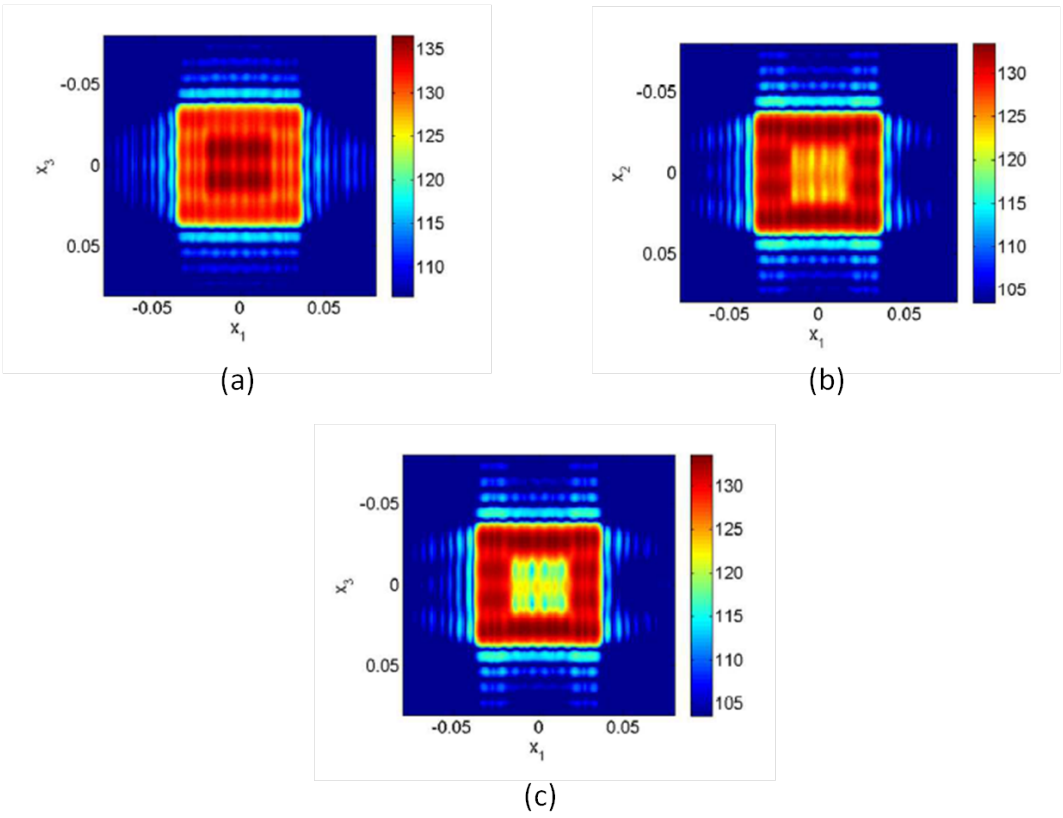


Figure 2.19: Reconstructed image in the vertical plane of three different targets overlapped to the skin - a) Pec + Skin b) TATB + Skin c) PP+Skin

### 2.3.5 Direct Signal Interference

The received signal can be modeled as 2.21

$$S_{rx}(\phi, \zeta_3, f) = S_t(\phi, \zeta_3, f) + S_d(\phi, \zeta_3, f) \tag{2.21}$$

where $S_t(\phi, \zeta_3, f)$ is the useful signal backscattered from the target and $S_d(\phi, \zeta_3, f)$ is the unwanted direct interference between the transmitter and

receivers antenna. The algorithm operates linear operations, so in the spatial domain, the reconstructed image concerning the focusing point $x_0$ is 2.22

$$\begin{aligned} S_{rx}(x_1, x_2, x_3; x_0) &= FT\{S_{rx}(\phi, \zeta_3, f) \cdot F(\phi, \zeta_3, f; x_0)\} \\ &= FT\{S_t(\phi, \zeta_3, f) \cdot F(\phi, \zeta_3, f; x_0)\} + FT\{S_a(\phi, \zeta_3, f) \cdot F(\phi, \zeta_3, f; x_0)\} \\ &= S_t(x_1, x_2, x_3; x_0) + S_a(x_1, x_2, x_3; x_0) \end{aligned} \quad (2.22)$$

where $S_t(\phi, \zeta_3, f)$ is the backscattered signal from the target, $S_a(\phi, \zeta_3, f)$ is the signal interference, and $FT$ is the Fourier operator. From the eq. 2.22 can be seen that the coupling interference can be eliminated by subtracting the images $S_{rx}(x_1, x_2, x_3; x_0)$ and $S_a(x_1, x_2, x_3; x_0)$, where the latter can be obtained by performing the measurements without the target. In the table 2.7 are listed the used parameters for the simulation.

| | |
|---|---|
| Scan angle | 30° |
| Central Frequency | $16.5GHz$ |
| Bandwidth | $1GHz$ |
| ♯ of frequencies | 5 |

Table 2.7: System parameters for direct interference cancellation

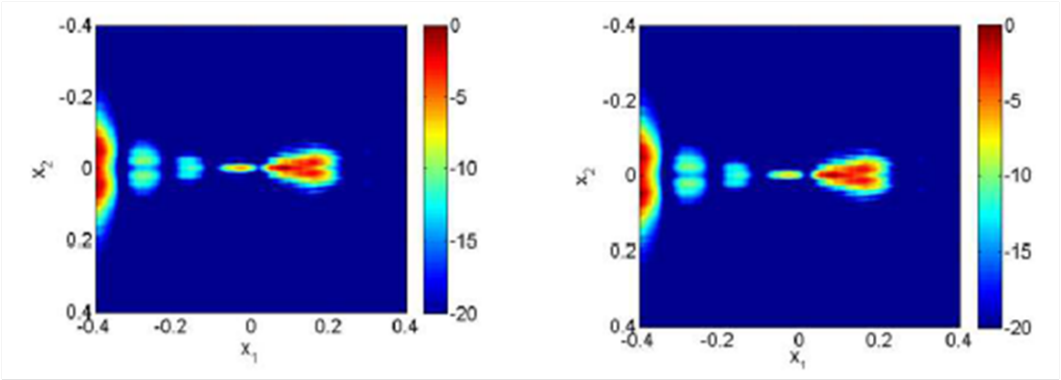


Figure 2.20: Reconstructed image (a) Received signal (b) Only direct signal

In figure 2.20 are shown the images obtained by simulating a direct signal without target about $40dB$ stronger than the useful signal. In figure 2.21 are reported the reconstructed images obtained by processing the backscattered signal, only from the target, and that obtained by subtracting from the image

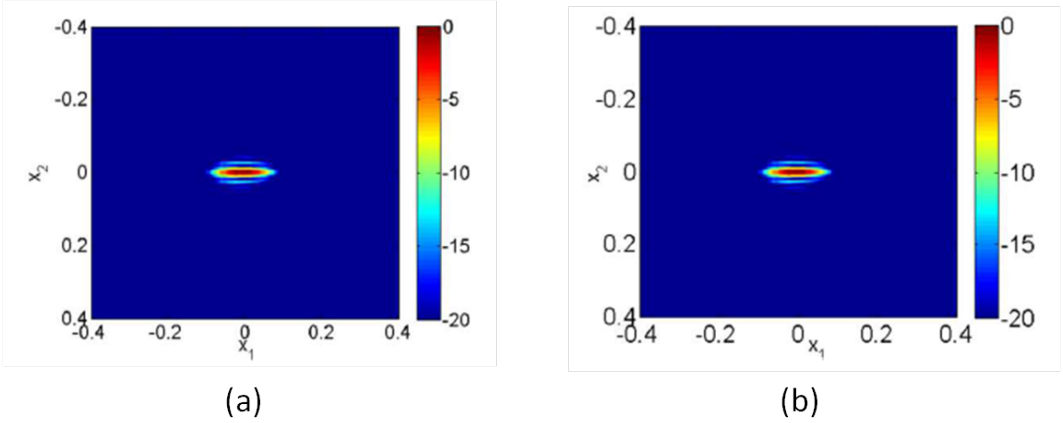


Figure 2.21: Reconstructed image (a) only target (b) obtained by subtracting the two images

of the whole received signal and that concerning only the environment without the target. By comparing figures 2.21(a) and 2.21(b) can be figured out that the two images are very similar, so the method used to reduce the direct signal interferences is efficient.

### 2.3.6 Waveform Bandwidth design

In this section some simulations are performed in order to evaluate if a bandwidth is required for the image reconstruction or just a single frequency waveform can be used, when an angle smaller than 360° is scanned. We simulated a cylinder of radius $r = 0.1m$ and height $h = 0.2m$ composed by several ideal point like scatterers, in order to simulate a continuous surface. The transmitter and the receiving array move together for a scanning angle of 120°. The transmitted signal is a stepped frequency waveform with a step of $\Delta f = 150MHz$ (see section 2.2.6).

In order to evaluate the benefits arising from the use of a wide band signal, in terms of spatial resolution and side lobes reduction, in figure 2.22 are compared some images of the target, in the horizontal plane, obtained by varying the bandwidth of the transmitted signal, until a maximum of $9GHz$. From the comparison of the images can be figured out that a wide band signal is necessary to reconstruct the three dimensional shape of the cylinder. In particular to have low enough side lobes level (-30dB), is required the use of a signal with bandwidth grater or at maximum equal to $6GHz$.

## 2.4 Sum up: final system design

The work presented in the first part of the thesis has been done for the design of a body scanner system, within the MELISSA project. The new algorithm presented in the chapter 1 has been developed in order to design the system, starting from the imaging requirement of a potential spatial resolution $\Delta\rho \leq 1cm$ in the three dimensional space, in the theoretical case of a scanned angle of 360°. From the analysis performed in section 2.3.3, the working frequency that would let us to fit the imaging requirement would be $f_0 = 35GHz$. Nevertheless, the frequency $f_0 = 16.5GHz$ let us to halve the costs for the receiving array. Therefore we decide to use the central frequency $f_0 = 16.5GHz$, although accepting a worsening of the spatial resolutions, as shown in the tables 2.3 and 2.4, for the resolution in the vertical and horizontal planes, respectively. Furthermore, a scan angle of 360° would result in a prohibitive scan time, for real time applications, so we decided to scan an angle of 120°, trading off worse spatial resolutions, see table 2.5, with smaller scan time. Once we decided to perform a scanning, in the horizontal plane, smaller than 360°, a wide band signal is required in order to reconstruct the three dimensional shape of the target, as demonstrated in section 2.3.6. The waveform we decided to transmit is a stepped frequency signal, composed by 64 frequencies, with a step of $100MHz$, for a totally bandwidth of $6.4GHz$, therefore, the radiating element has to be designed in order to transmit within the range of $13.4GHz - 19.7GHz$. The receiving array consists of 256 single elements, spaced of $\lambda/2$, see section 2.3.1, with $\lambda = 9.1mm@16.5GHz$, as consequence it is $2.32m$ of height . In order to implement the SAR technique in the vertical dimension, each single element acquires one of the 64 frequencies, of each $300ns$, for a time slot of $19.2\mu s$. The system completes a scan in the vertical dimension in $\mathbf{T_v} = 19.2\mu s \cdot 256 = \mathbf{4.91ms}$. The mechanical handling in the horizontal dimension has to be designed starting from the scan angle, that we already decided to fix at 120°. The radius of the shelter is about $1m$, the equivalent movement of 120° is a linear distance of about $2m$. In order to scan such distance, we decided to move the array with a velocity of $0.96m/s$, and to acquire 512 samples during the movement. Finally, the required time for the total acquisition of the system is $\mathbf{T_f} = T_v \cdot 512 = \mathbf{2.516s}$.

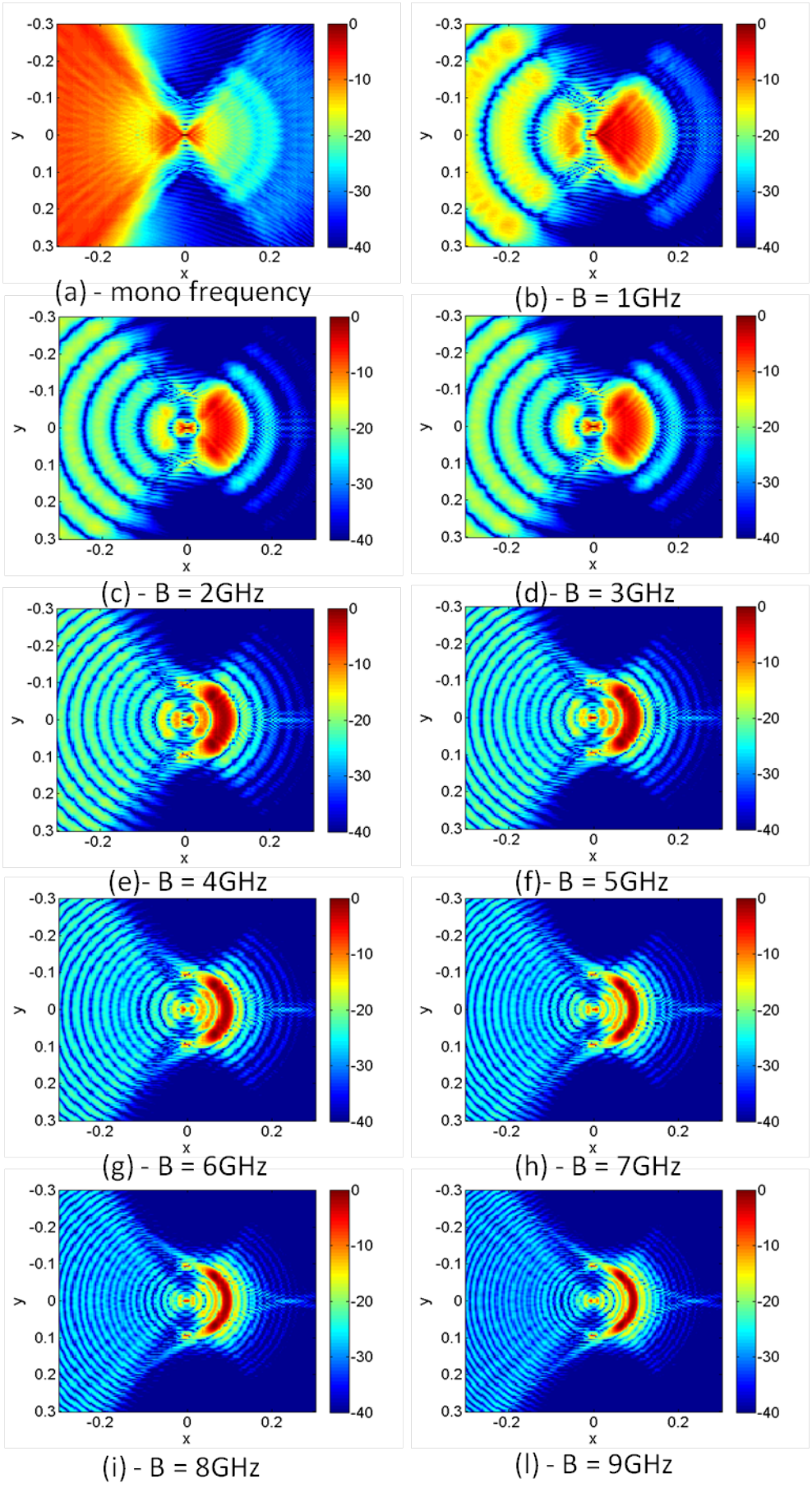


Figure 2.22: Reconstructed image in the horizontal plane, scanning angle of 120°

# Chapter 3

# Real Data Results and Analysis

## 3.1 First target: Cylinder

The data used to test the performance of the proposed imaging algorithm have been acquired in an anechoic chamber with a controlled experiment type. The antenna used to transmit the signal is a horn antenna, while the receivers are Waveguide Horn Antennas. In this experiment were transmitted signals at 5 different frequencies, centered around the central frequency $f_0 = 35GHz$ and equally spaced of $\Delta f = 250MHz$, such as to synthesize a signal with bandwidth $B = 1GHz$.

The transmitter and the receiver are distant from each other 60° in the horizontal plane. In order to reduce the coupling between transmitter and receiver, a panel covered with absorbent material has been interposed in the middle 3.1.

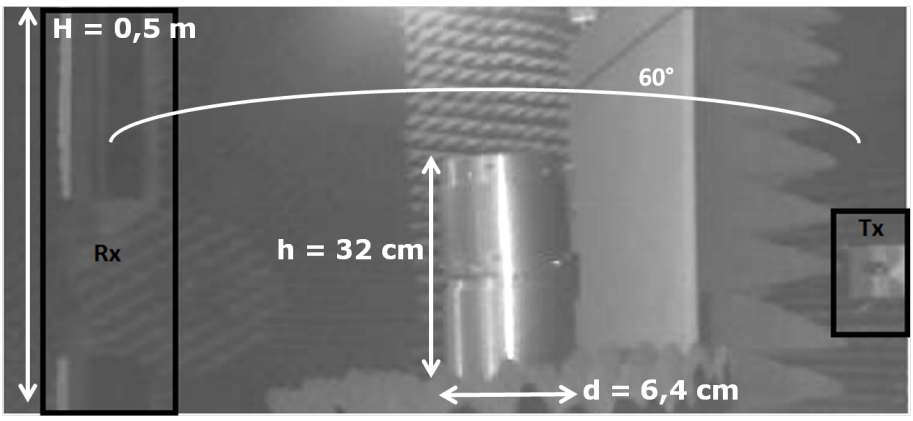


Figure 3.1: Target used for the measurements

The vertical array consists of 125 receiving antennas, equally spaced of 4 mm. So the array receiver is 0.5m high. Each receiving element receives the signal at different time intervals, so as to emulate a SAR system. The target is placed on a turn-table covered with absorbent material. After each acquisition of the entire array , the turn-table is rotated of 0.228°, until a total angle of 30° is scanned 3.2.

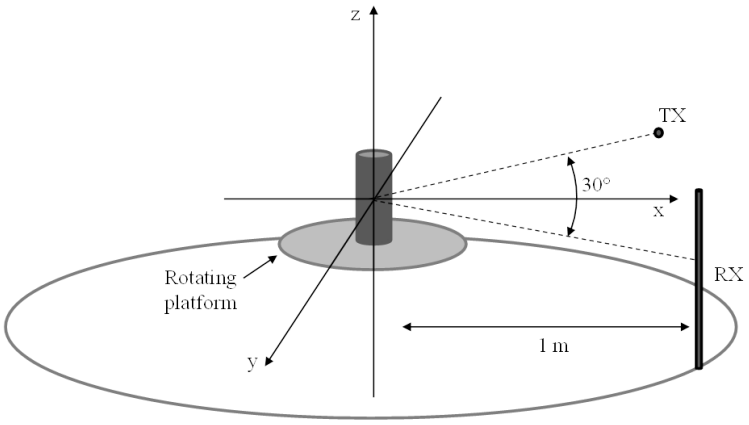


Figure 3.2: Real data acquisition geometry

The target is placed at $1m$ from the transmitter. it is $32cm$ high and it has a diameter of $6.4cm$. As can be seen from figure 3.1, the target is not a perfect cylinder but it is composed of two cylinders, placed one above the other. Unfortunately, some imperfections of the target can be noticed, for example the presence of bolts at the center and at the top of it, as well as the misalignment of the two cylinders.

In figures 3.3,3.4,3.5 are shown the images obtained by processing the acquired data, only for the central frequency, in the vertical and horizontal planes, respectively.

The reference system has been considered such that the $x_1$ axis matches with the range, and the $x_2$ axis with the cross-range. As depicted in figure 3.2, the scan geometry matches with that of a BEM radar which moves in the angular range $[-15°, 15°]$. Therefore, referring to the BEM radar, the resolutions along the two main axes, the range and cross-range, can be estimated as the inverse of the size of the domain within the received signal is defined, as in eq. 3.1 and 3.2.

$$\delta x = \frac{1}{\frac{2}{\lambda}(1 - cos(15°))} \cong 12.5cm \tag{3.1}$$

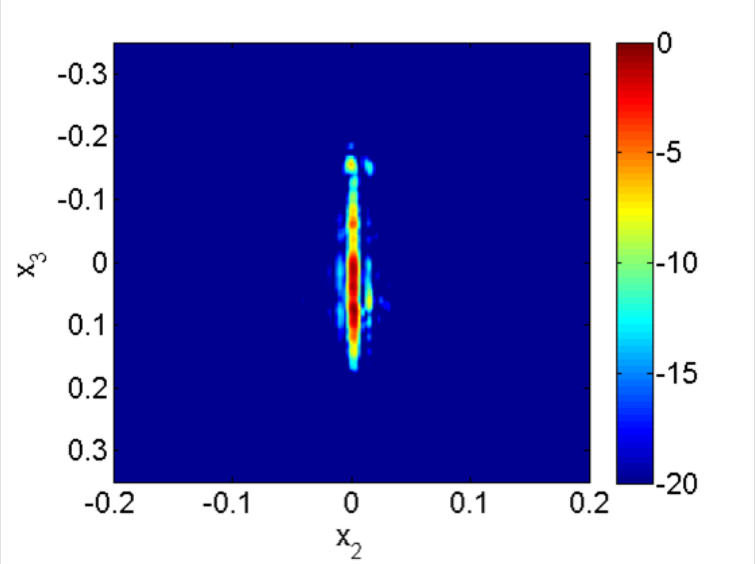


Figure 3.3: Reconstructed image of the cylinder of fig. 3.1, in the $x_2 - x_3$ vertical plane

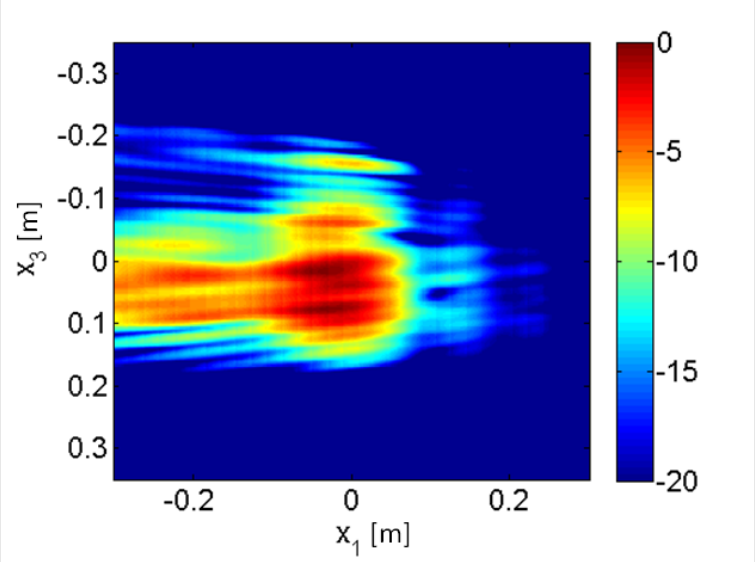


Figure 3.4: Reconstructed image of the cylinder of fig. 3.1, in the $x_1 - x_3$ vertical plane

$$\delta y = \frac{1}{\frac{4}{\lambda}(sin(15°))} \cong 5mm \tag{3.2}$$

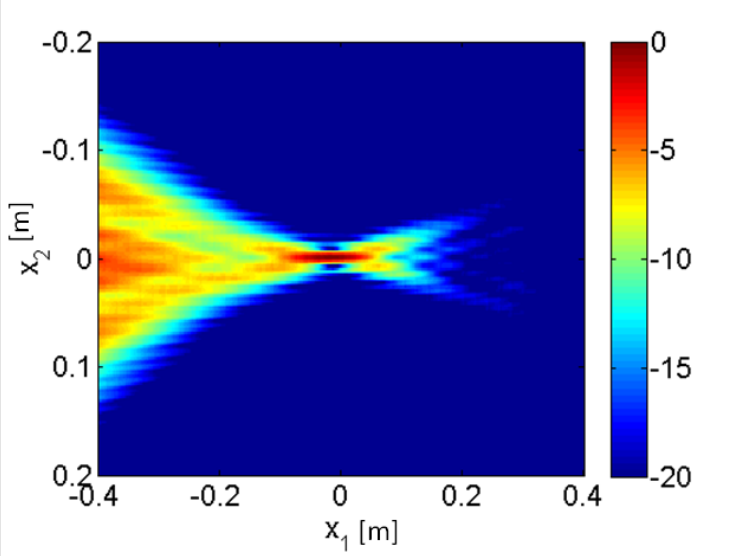


Figure 3.5: Reconstructed image of the cylinder of fig. 3.1, in the $x_1 - x_2$ horizontal plane

Equations 3.1 and 3.2 confirms the different spatial resolutions along the main axis.

From figure 3.3 can be figured out that the height of the target is estimated well enough. The absorbent panel that covers the turn-table on which the target is placed absorbs most of the backscattered radiated signal, which explains the lower reflectivity values for negative heights. It is worth noting that the irregularities (comparable with the wavelength) of the cylinder diffract more than a regular surface.

From figure 3.5 can be observed that because of the effect of interferences and pseudo solutions, the edge of the cylinder cannot be appreciated, in fact only a point that matches with its center is visible. Several interferences have radial direction, so they are combined in a constructive manner in the point that matches with the axis of the cylinder. This phenomenon can be reduced by using a wide band signal. For such reason, the whole bandwidth of the signal has been used by combine the five signals at different frequency. By processing the multi frequency signal, the obtained images are shown in figures 3.6 and 3.7.

By comparing the obtained images in the vertical plane, in the mono frequency case 3.4 and in the multi frequency case 3.6 and by comparing the obtained results in the horizontal plane, in the mono frequency case 3.5 and in the multi frequency case 3.7 can be assessed:

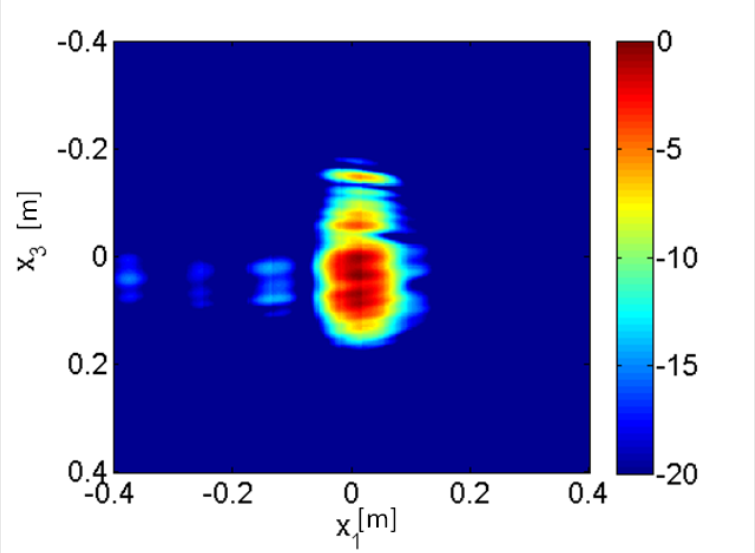


Figure 3.6: Reconstructed image of the cylinder of fig. 3.2, in the $x_1 - x_3$ vertical plane, by exploit the multi frequency signal

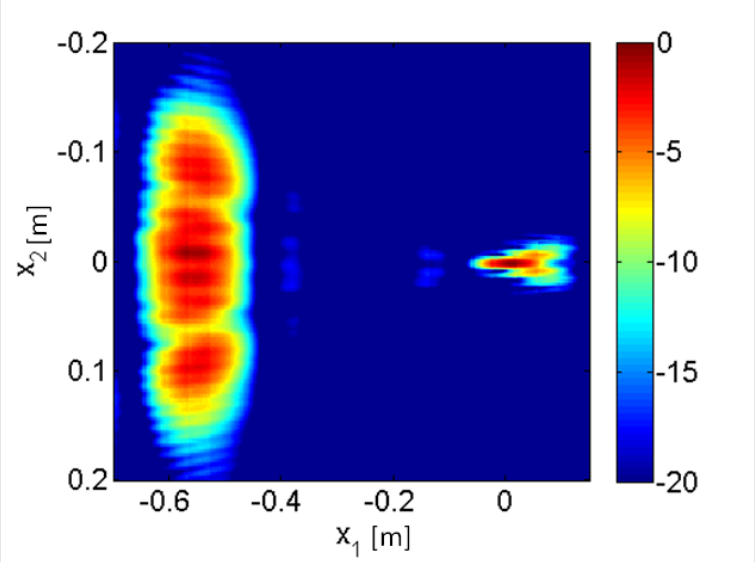


Figure 3.7: Reconstructed image of the cylinder of fig. 3.2, in the $x_1 - x_2$ horizontal plane, by exploit the multi frequency signal

- The side lobes are greatly reduced.
- The range ($x_1$) resolution is improved.

- The area of high intensity that persists for negative ranges is a folding of the spectrum due to the sampling in the frequency domain. In fact, from the figure 3.7 can be seen that the distance between the two regions of strong intensity is about $0.6m$, value equal to the repetition period of the spectrum, given by the equation 3.3

$$\Delta x = \frac{c}{2\Delta f} = \frac{3 \cdot 10^8}{2 \cdot 250 \cdot 10^6} \cong 0.6m \tag{3.3}$$

- Nevertheless, the edge of the cylinder cannot seen yet, but this is most likely due to the fact that the range resolution is still too large compared to the radius of the cylinder itself.

## 3.2 Second target: Panel with different materials

In order to the evaluate the performance of the algorithm in terms of the radiometric resolution, so the ability to discriminate materials with different characteristics, a measurement campaign was done with a target composed of four different materials: copper, ceramic, plastic, and a liquid with similar properties to the human skin. The measurements in the anechoic chamber was performed by using the setup shown in fig. 3.8(a), while in fig. 3.8(b), the geometry of scanning is depicted.

Data have been obtained by transmitting five different frequencies, equally spaced of $250MHz$, for a totally bandwidth of $1GHz$. The central frequency is $16.5GHZ$, the panel lies on a turn table that scan an angle in the horizontal plane of $60°$, the vertical array consists of 55 elements equally spaced of $9mm$.

Figure 3.9 shows two images representing the target in two horizontal planes at different heights, $x_3 = 0m$ (a) and $x_3 = 0.1m$ (b). The images are obtained by processing the only data at the central frequency.

From figures 3.8(a)-(b) can be figured out that the actual position of the target cannot be determined, because the target totally lies on the vertical plane.

Figures 3.10 (a)-(h) show the reconstructed target in the vertical plane, for different values of $x_1$.

As can be seen from the images 3.10, they mainly differ in the size of the target and for the intensity values. The whole panel should be of dimensions $0.3m\,x\,0.3m$ and the size of each single patch of material are $0.15m\,x\,0.15m$.

For a better image reconstruction, the multi - frequency data must be processed. Figure 3.11 shows the same situation of figure 3.9, but it has been

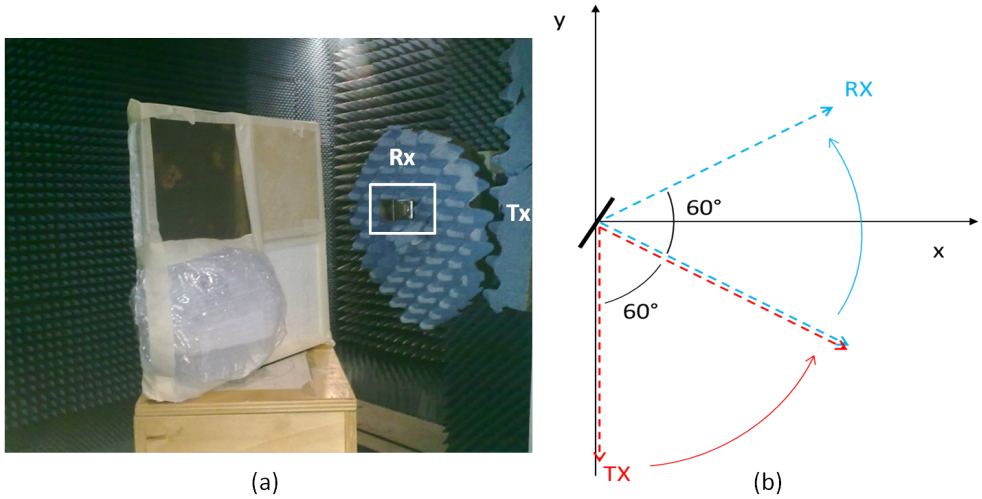


Figure 3.8: (a) - Measurement setup for the panel multi-material (copper in the upper left corner, ceramic in the upper right corner, liquid in the lower left corner, plastic in the bottom right corner). (b) - Geometry of scanning: the angle between transmitter and receiver is 60° and the scanning is performed for an angle of 60°

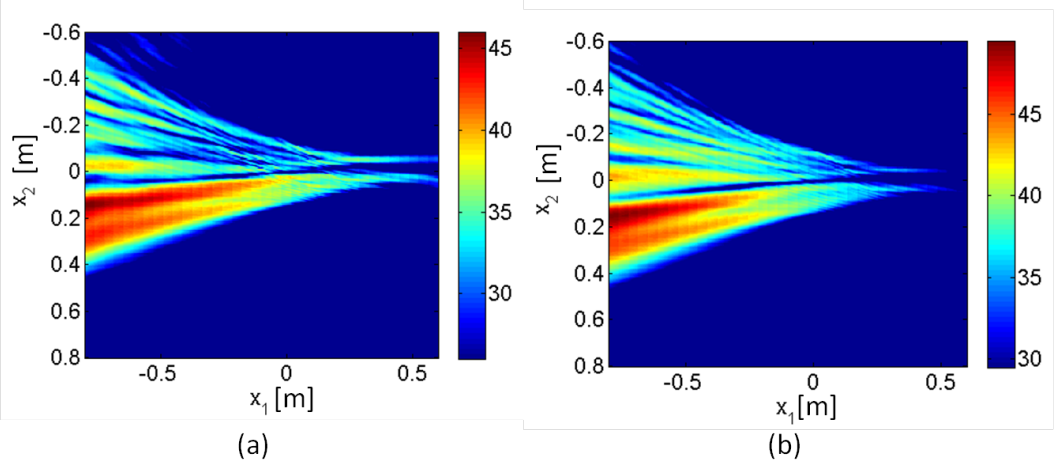


Figure 3.9: Reconstructed image of the target depicted in fig. 3.8 for (a) $x_3 = 0$ - (b) $x_3 = 0.1$

obtained by exploiting the data bandwidth.

As can be seen from the figure 3.9, after processing the multi frequency data, it can be understand that the target lies at $x_1 \cong -0.15m$. The other signal contribute of strong intensity value, located at about $x_1 \cong= -0.75m$ is

the folding due to the frequency spacing of the stepped waveform.

Figure 3.12 shows the reconstructed image of the target in the vertical plane, at $x_1 = -0.15m$, in the multi frequency case.

The analysis above mentioned, has been necessary in order to detect the actual position of the target in the range direction, because its position was not known from the measurements done.

The obtained results shown in the figure3.12, would seem state that the ceramic ( upper right corner) scatterers more than the copper ( upper left corner). Actually, the copper patch is slightly upwardly tilted, therefore the most of the backscattered signal is not intercepted by the receiving antenna. Moreover, the plastic scatterers less than other all materials, while the intensity of the liquid representing the human skin may be corrupted by the presence of the adhesive tape.

## 3.3 Third target: Panel with balls and padlock

In the last measurements we decided to detect different targets located on the same panel, in order to understand if the spatial resolutions are finer enough to detect close targets with different radiating properties. The setup is shown in figure 3.13.

First of all, the calibration measurements have been done. The answer of the anechoic chamber plus the strut panel without target have been measured. As already stated in section 2.3.5, these measurements can be used to reduce the direct signal interferences. The receiving antenna moves in the vertical direction in order to synthesize an array of 113 element equally spaced of $9mm$, for a total length of $1m$. The center of the panel is perfectly aligned whit the transmitter and with the central element of the receiving array, it is $1m$ far from both of them. Transmitter and receiver are separated by a distance of $39,68cm$ and between them an absorbing panel is placed in order to reduce the direct interferences. The central frequency is equal to $16.5GHz$, the transmitted signal is a stepped frequency waveform of 32 frequencies equally spaced of $203MHz$, for a bandwidth of $6GHz$. The turn table moves by scanning an angle of 120° in the horizontal plane. Figure 3.14 shows the reconstructed image of data without target, but only with the strut panel.

After that, the measurements with the target of figure 3.15 have been performed.

The reconstructed image of the target depicted in figure 3.15 is shown in figure 3.16.

As can be seen from the figure 3.16, the padlock is clearly visible, while the two balls are masked by the background. For this reason, by subtracting the image of fig. 3.14 at that of fig. 3.16, the background can be reduced and the targets became elated, see figure 3.17.

Moreover, a further measurement by adding other targets but always keeping the same setup has been performed. The new target is depicted in figure 3.18.

Because the setup is the same as the previous measurements, the background of fig. 3.14 can be used in order to reduces the direct signal interferences. Therefore, after this post processing technique, the reconstructed image concerning the target of fig. 3.18 is shown in figure 3.19.

From the figure 3.19 can be see that the padlock scatters more than all other objects and it is left turned of 90° respect the figure 3.16.

Unfortunately, the ball in the origin of the system has been partially deleted because it is located exactly in correspondence of the background, and then confused as being a part of it.

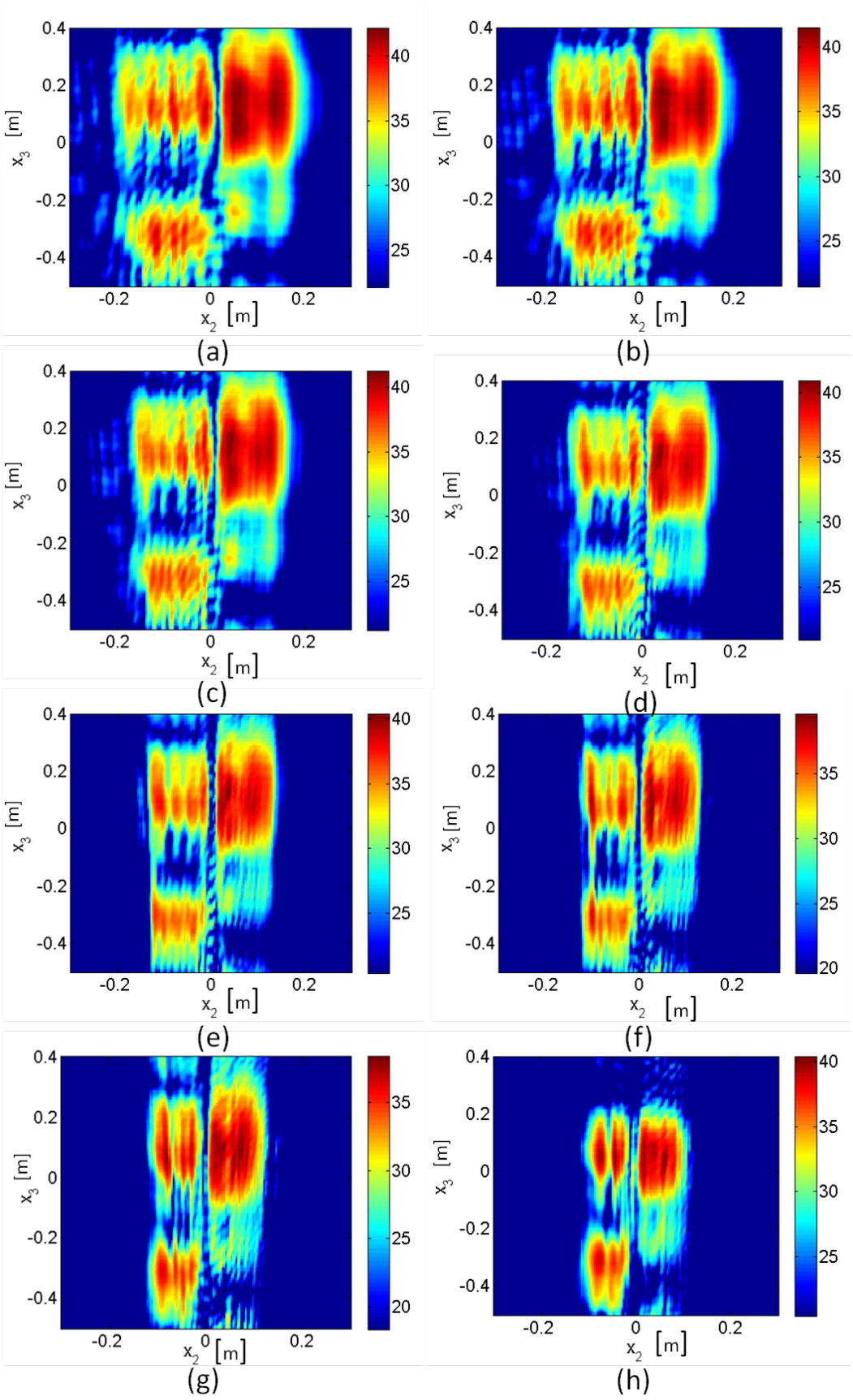


Figure 3.10: Reconstructed image of the target depicted in fig. 3.8 in the vertical plane for different values of $x_1$, mono-frequency case.

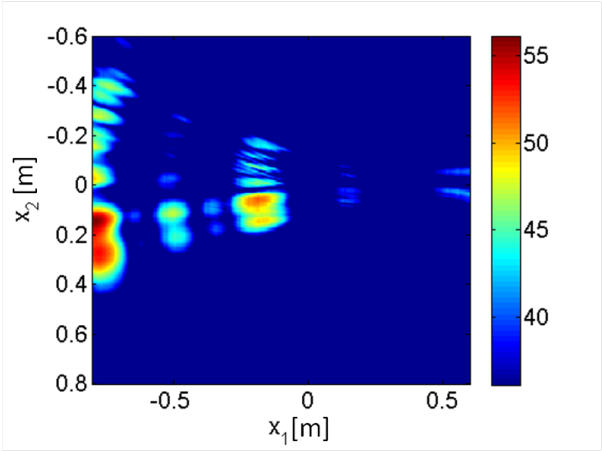


Figure 3.11: Reconstructed image of the target depicted in fig. 3.8 in the horizontal plane, multi frequency case.

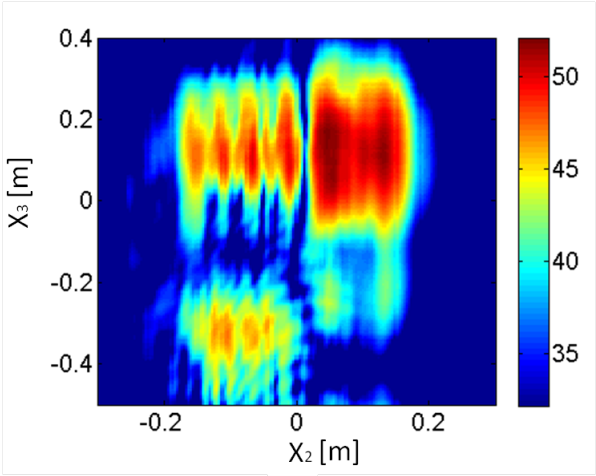


Figure 3.12: Reconstructed image at $x_1 = -0.13m$of the target depicted in fig. 3.8 in the vertical plane, multi frequency case.

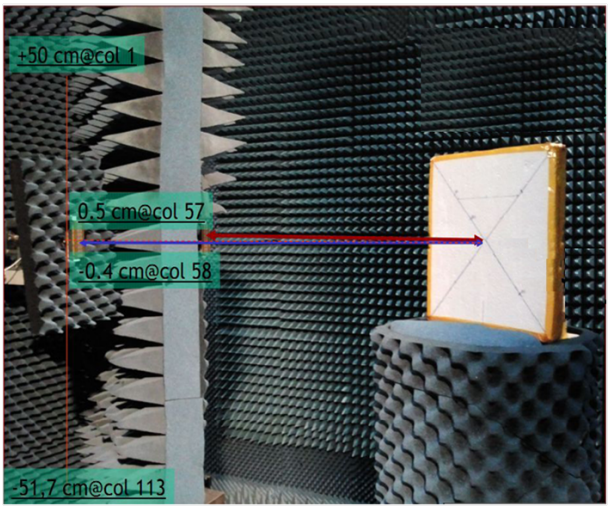


Figure 3.13: Measurement setup

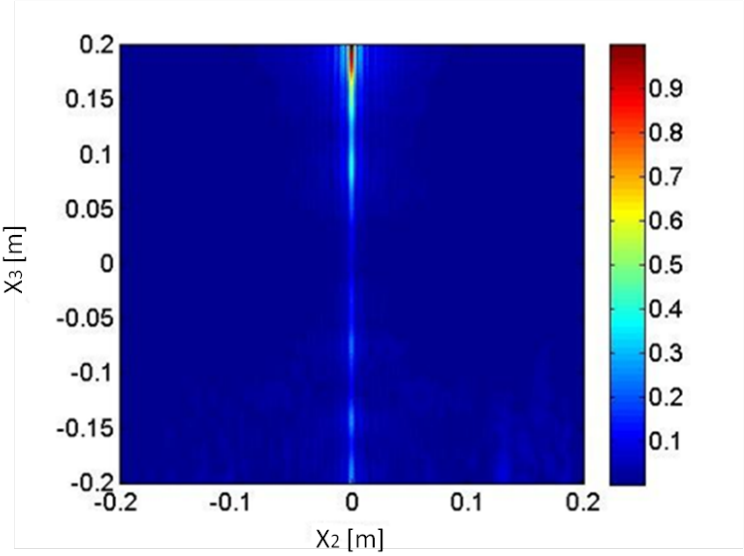


Figure 3.14: Reconstructed image of the background

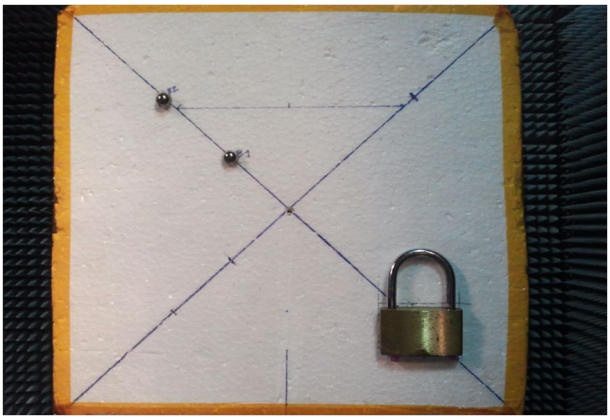

Figure 3.15: Target: Panel with two balls of $9mm$ of diameter and a padlock

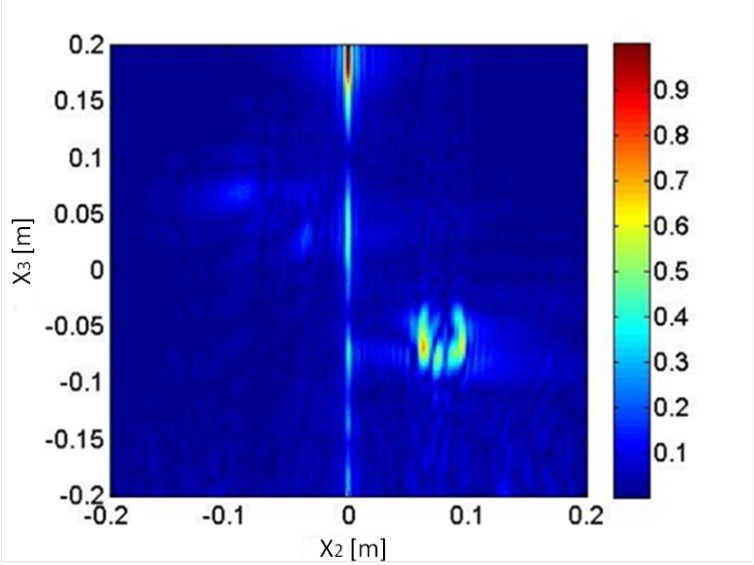


Figure 3.16: Reconstructed image of the target depicted in fig. 3.15

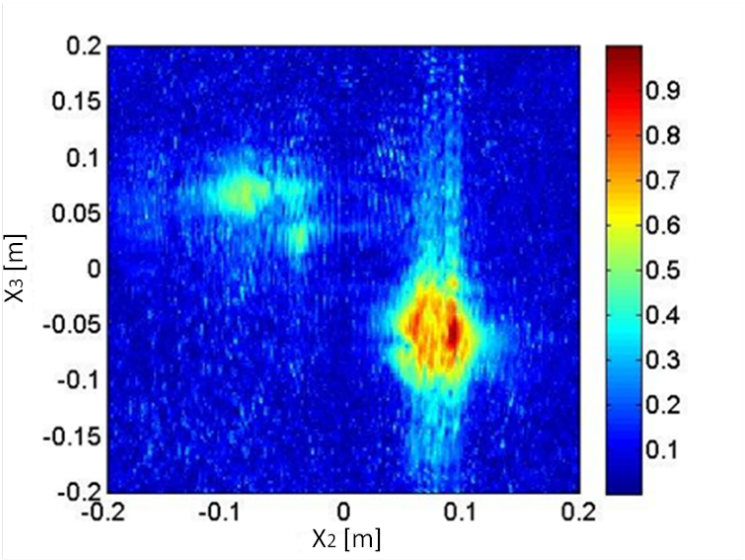


Figure 3.17: Reconstructed image of the target depicted in fig. 3.15, at which the background has been removed

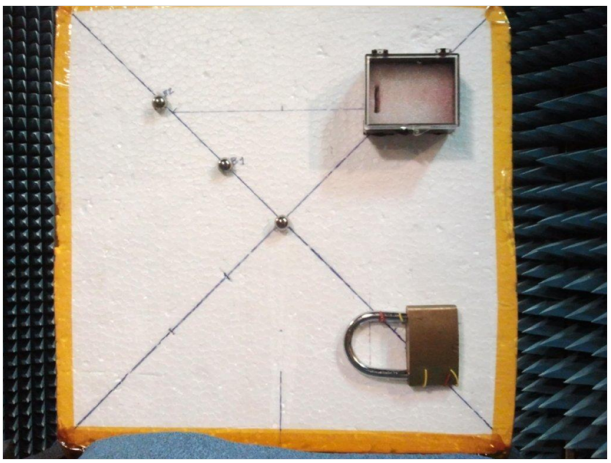

Figure 3.18: Target: three balls plus a padlock and a metal box

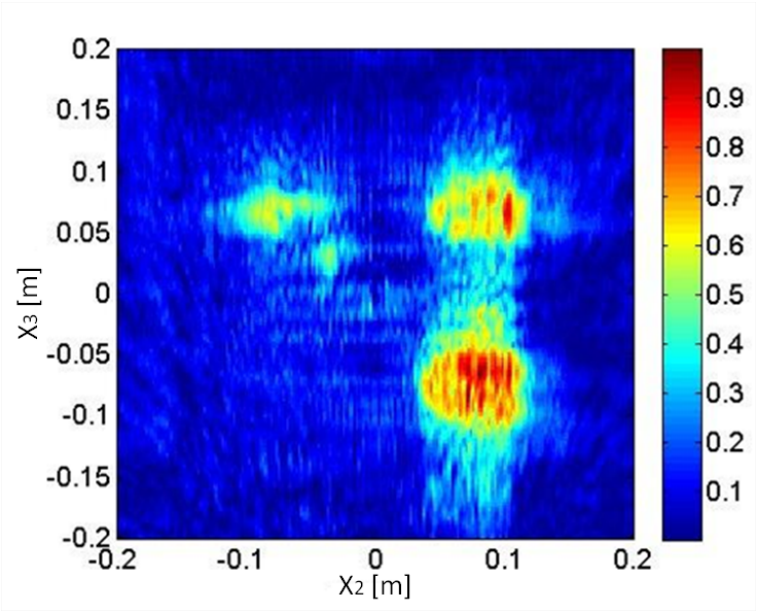


Figure 3.19: Reconstructed image of the target of figure 3.18

# Chapter 4

# Innovative ISAR Signal Processing

## 4.1 APIS: Array Passive ISAR adaptive processing

The second part of this thesis has been developed under the APIS project. APIS is defined as a multichannel, bi-static single receiver for array passive radar, capable of detecting targets and generating ISAR images of the detected targets for classification purposes. At the end of the project a prototype was built, see figure 4.1, it has been used for real data acquisition and the obtained results are discussed in the chapter 6.

In this work, we only concentrate on the ISAR processing. Purpose of the ISAR processing is to extract an electromagnetic bi-dimensional image of the target in order to determine the main geometric features of the target, allowing (when possible) recognition and classification.

## 4.2 Introduction

As recently demonstrated, passive radars are able to detect and track targets by exploiting IOs. In this work of thesis, it will be proven that the same concept can be extended to allow for P-ISAR imaging. A suitable signal processing is detailed that is able to form P-ISAR images starting from range-Doppler maps, which represent the output of a passive radar signal processing. Multiple channels DVB-T signals are used to demonstrate the concept as they provide enough range resolution to form meaningful ISAR images. The problem of grating lobes, generated by DVB-T signal, is also addressed and


Figure 4.1: APIS demonstrator

solved by proposing an innovative P-ISAR technique. Passive radar have been recently studied and implemented by a number of scientists and engineers, as demonstrated by the large impact in the literature and by the amount of system demonstrators and prototypes [13–15]. Passive radar have a number of obvious advantages over active radar systems: low cost, low vulnerability to electronic countermeasure, reduced Electro-magnetic pollution and counter-stealth advantage. On the other hand, since they exploit reflection from IOs, they do not use waveforms designed for radar purpose. The detection performance of passive radars based on analogue signals are strongly dependent on the signal content. On the contrary, digital waveforms as digital radio Digital Audio Broadcasting (DAB) and television Digital Video Broadcasting (DVB) provide much more efficient and attractive spectral properties since they use a Coded Orthogonal Frequency Division Multiplex (COFDM) modulation. Among digital IOs, DVB-T signals have a wide bandwidth that allows achieving good spatial resolution together with a very good spatial coverage. For effective ISAR imaging, a mandatory requirement is achieving fine range resolutions. More recent work has demonstrated that high range resolution passive radar can be enabled by using Multichannel DVB-T signals, which represents an important step towards passive radar imaging capabilities. As demonstrated in [17], a wideband signal of opportunity can be obtained by coherently adjoining N adjacent DVB-T channels, which produce a range resolution improvement by a factor N. Two further main ingredients are combined to define a framework for P-ISAR. The first one comes from recent Bistatic ISAR theoretical results . Specifically in [18], it was firstly proven that a BEM

geometry can be introduced that can replace the bi-static geometry and, secondly, that monostatic ISAR processing can be used to form bistatic ISAR images under certain constraints. As passive radars operate in bistatic configurations, bi-static ISAR must be considered and therefore results obtained in this field may be exploited. The last ingredient concerns the application of ISAR processing to defocused SAR images of non-cooperative moving targets. As recently proposed in [19], ISAR processing can effectively be used to refocus SAR images of moving targets by means of a novel approach, which is based on moving target detection and data back-projection. Arange Doppler (RD) map is typically obtained as an output of standard passive radar signal processing, which is usually addressed as Cross-Ambiguity Function (CAF). By interpreting such RD map as a non-focused target image, the same processing adopted in [19] can be applied to refocus such targets. The problem of grating lobes generated by the presence of gaps between adjacent DVB-T channels is also addressed and a new technique based on an extension of the Spatially Variant Apodization (SVA) technique is proposed. Results obtained by processing real data are presented that demonstrate P-ISAR capabilities. It should also be mentioned that the results presented in this thesis will be based on the use of only three adjacent DVB-T channels due to current hardware limitations. Nevertheless, the concept is demonstrated and improvement in terms of range resolution is expected by upgrading the hardware. It should also be pointed out that P-ISAR processing can easily be implemented in real-time and therefore it may represent a useful and low-cost passive radar system add-on. It should be noted that an attempt towards passive radar imaging has been made recently. The main differences arising between the proposed approach and that proposed in [20], [21] are to be found in: 1) the clutter suppression step, which, in the approach presented in this thesis, is defined in the RD domain and aims at suppressing all returns around the target, 2) the ISAR image formation algorithm which is based on the Image Contrast Based Autofocusing (ICBA) algorithm which was proposed in [22].

## 4.3 Basics on Passive Bistatic Radar (PBR)

The bistatic geometry [25–27] is shown in figure 4.2, where $T_x$ is the transmitter, $R_x$ is the receiver and the distance between them is the baseline $L$. The target lies at a distance $R_T$ from the transmitter and at a distance $R_R$ from the receiver. The triangle formed by the three points $T_x, Rx$ and the targets lies in the bistatic plane. The angle defined by the triplet $T_x - Target - Rx$

is called the bistatic angle $\beta$, it is equal to [25]

$$\beta = \Theta_T - \Theta_R \tag{4.1}$$

where $\Theta_T$ is the angle defined by the north direction and the line $T_x$ to the target, while $\Theta_R$ is the angle defined by the north direction and the line $Rx$ to the target, both angles are taken as positive when going clockwise from North.

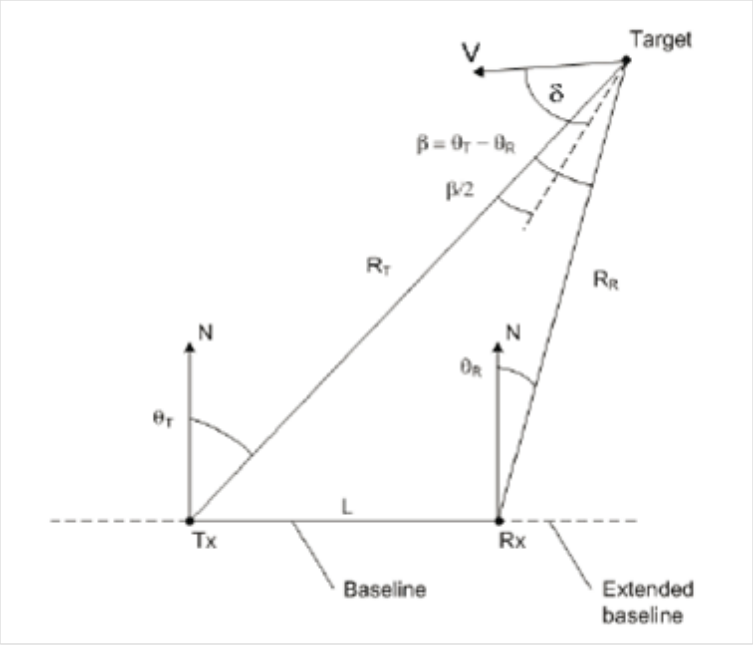


Figure 4.2: The bistatic geometry

A bistatic radar measures the target range as the range sum, $R_T + R_R$. In the $2D$ dimension this constitutes an ellipse while in the $3D$ space an ellipsoid. The formed ellipse is called an iso-range contour. Each target echo in a bistatic radar system will generate one constant range sum ellipse in $2D$ or a part of it. Consider a transmitter with an omni-directional antenna transmitting a signal with a bandwidth of $B = 100KHz$, giving a range resolution of $\Delta R = c/2B = 1500m$. Assume there is an omni-directional receiving station positioned $40km$ east of the transmitter. The bistatic radar resolution for this system is shown in figure 4.3, where the iso-range contours are plotted [27].

The Bisector of the bistatic angle $\beta/2$ is indicated in figure 4.2 with the dotted line, it halves the bistatic angle and it is orthogonal to the tangent of the iso-range contour at any point on the bistatic iso-range contour. The

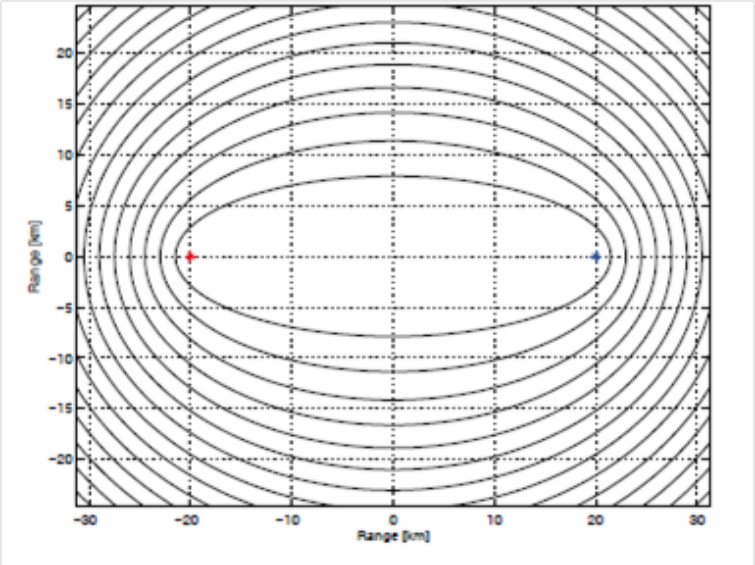


Figure 4.3: Bistatic range resolution. The distance between the contours are given by the signal bandwidth. $T_x(red), R_x(blue)$.

eccentricity, $e$, of the iso-range contour is [25]

$$e = \frac{L}{R_T + R_R} \tag{4.2}$$

where $0leele1$. For the monostatic case $R_T = R_RandL = 0$ resulting in $e = 0$. instead, when the target is on the baseline between the transmitter and the receiver, $L = R_T + R_R$, the eccentricity is $e = 1$. In this case there is no Doppler and range information available in the received signal. Therefore, the eccentricity can be regarded as a measure of how bistatic the $Tx - target - Rx$ geometry is, $e = 0$ being monostatic, and $e = 1$ meaning the transmitter, target and receiver being on a line with the $T_x$ facing the $R_x$.

## 4.4 Bistatic Passive Isar Imaging

The performance of a passive radar system strongly depends on the transmitted power and on the characteristics of the exploited IOs, which is used as a reference signal. As the range coverage increases when the transmitted power level increases, high-power transmitters, such as broadcast Frequency Modulated (FM), DAB radio, analogue and DVB television transmitters, are to be preferred. Among these, DVB-T transmitters should be considered the best candidates for passive radar purposes thanks to their high level of radiated

power and the good waveform performances in terms of range and Doppler resolution. A range resolution improvement can be obtained by considering multiple adjacent DVB-T channels as a single wideband signal, which represents an important step towards passive radar imaging capabilities. In Figure 4.4, the considered bistatic ISAR geometry is shown [18].

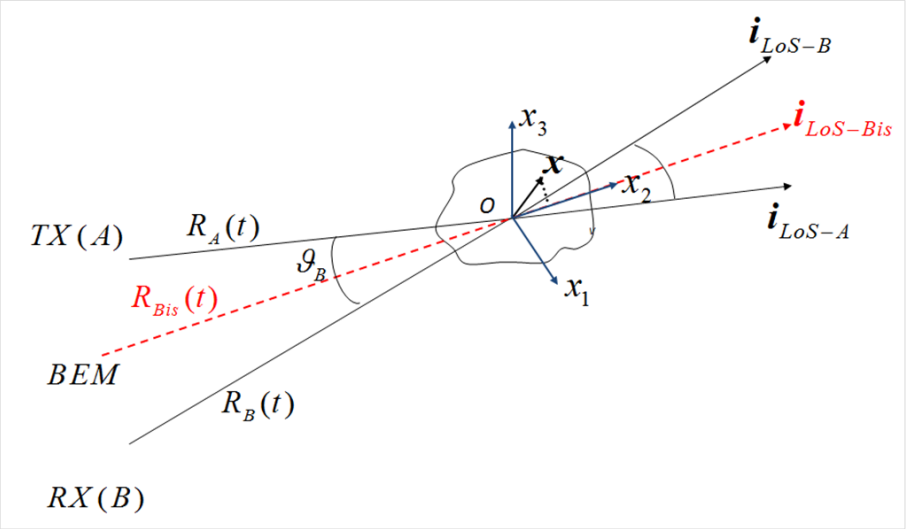


Figure 4.4: Bistatic ISAR geometry.

The analytical description of the signal model is the following

$$S_R(f,t) = W(f,t) \int_V \zeta(x) e^{j\frac{4\pi f}{c}[R_{Bis}(t)+K(t)\mathbf{x}\cdot\mathbf{i}_{LOS-Bis}(t)]}\, dx \tag{4.3}$$

where

$$W(f,t) = rect\left(\frac{t}{T_{Tobs}}\right) rect\left(\frac{f-f_0}{B}\right) \tag{4.4}$$

$$R_{Bis}(t) = \frac{R_A(t)+R_B(t)}{2} \tag{4.5}$$

$$K(t) = \left|\frac{\mathbf{i}_{LOS-A}(t)+\mathbf{i}_{LOS-B}(t)}{2}\right| = cos\left(\frac{\Theta_B(t)}{2}\right) \tag{4.6}$$

$$\mathbf{i}_{LOS-Bis}(t) = \frac{\mathbf{i}_{LOS-A}(t)+\mathbf{i}_{LOS-B}(t)}{|\mathbf{i}_{LOS-A}(t)+\mathbf{i}_{LOS-B}(t)|} \tag{4.7}$$

and where $S_R(f,t)$ represents the received signal in the conjugate Fourier domain of the RD map, specifically $(f,t)$ are the conjugate variables of range

and Doppler, the function $\zeta(x)$ represents a bistatic reflectivity function rather than a monostatic one, $\theta_B(t)$ is the bistatic angle which changes during the Coherent Processing Interval (CPI) depending on the motion of the target, $f_0$ represents the carrier frequency, $B$ is the transmitted signal bandwidth, $T_{obs}$ is the observation time, $V$ is the spatial region where the bistatic reflectivity function $\zeta(x)$ is defined, and function $rect(\cdot)$ yields 1 when $|\cdot| < 0.5$, and is 0 otherwise. It is worth pointing out that: $R_{Bis}(t)$ looks like an equivalent monostatic distance from point "O"and the radar. Although it is not a real monostatic distance, a new BEM LoS, $\mathbf{i}_{LOS-Bis}(t)$ is defined (i.e. the bisector of the bistatic angle) and then a distortion term $K(t)$ is introduced by changing in the bistatic geometry. It has been proven in [18] that a monostatic ISAR processor is able to form ISAR images also in the bistatic case, provided that the bistatic angle change rate is not too strong. It should however be noted that the image obtained by using a monostatic processor is compressed by a factor $K = K(0)$ both along the range and the Doppler coordinate. The term $K(t)$, given by 4.6, carries information about the change in time of the bistatic geometry. However, what significantly affects the ISAR image PSF is the change of the bistatic angle during the coherent integration time. In deriving the PSF, two assumptions are made that allow the application of the RD technique when reconstructing the ISAR image. These two assumptions are: 1) Far field condition and 2) short integration time. In [18] the conditions on the limitation with respect to the bistatic angle variation are discussed. The following relationships must be verified:

$$|\dot{\theta}(0)| < \frac{2\Delta r}{T_{obs} x_2^M |\sin\left(\frac{\theta(0)}{2}\right)|} \tag{4.8}$$

$$|\dot{\theta}(0)| < \left| \frac{c}{f_0 T_{obs}^2 x_1^M \Omega \sin\left(\frac{\theta(0)}{2}\right)} \right| \tag{4.9}$$

Where $\Delta r$is the range resolution, $x_2^M$ is the scatter with maximum distance from the focusing centre in the range dimension, $T_obs$ is the observation time, $\theta(0)$ is the bistatic angle at the central instant $t = 0$ and $|\dot{\theta}(0)|$ is the variation with respect to the time of the bistatic angle. Concerning the eq. 4.9, c is the speed of the light in the vacuum, $f_0$ is the carrier frequency, $\Omega$ is the effective rotation vector, $x_1^M$ is the scatter with maximum distance from the focusing centre in the cross-range dimension. Equations 4.8 and 4.9 provide two conditions in the range and cross-range dimension respectively that must be satisfied. Specifically the first one avoids any range migration induced by the bistatic angle variation within $T_{obs}$. The latter avoids chirp effects,

dependent on the bistatic angle variation, which cause defocusing effects on the ISAR image [18]. The main steps of a monostatic ISAR imaging processor are recalled in figure 4.5.

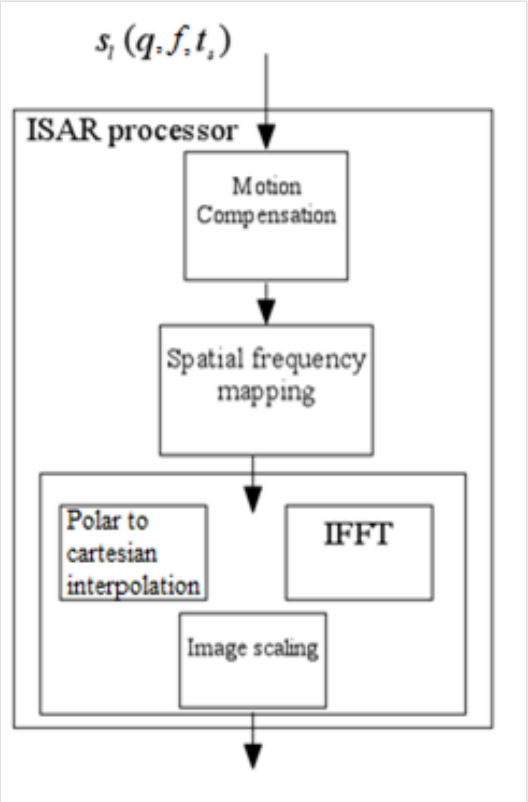


Figure 4.5: ISAR processing scheme

If more than one emitter of opportunity is used, several bistatic pairs can be formed. In order to coherently process more than one passive ISAR image, two considerations must be made:

- ISAR images have to be focused with respect to the same focusing point.
- The bistatic ISAR configurations may have different imaging planes. In this case multistatic coherent ISAR processing techniques must be suitably defined.

The general approach to the ISAR problem is depicted in the flow chart of figure 4.6, in which all cases are contemplated. It is worth noting that the most simple case is obtained when just one emitter of opportunity is used and multiple bands are exploited to achieve the desired range resolution. It

is the treated case in this thesis, where the classical bistatic ISAR imaging technique can be applied together with multi-frequency processing to obtain range compression.

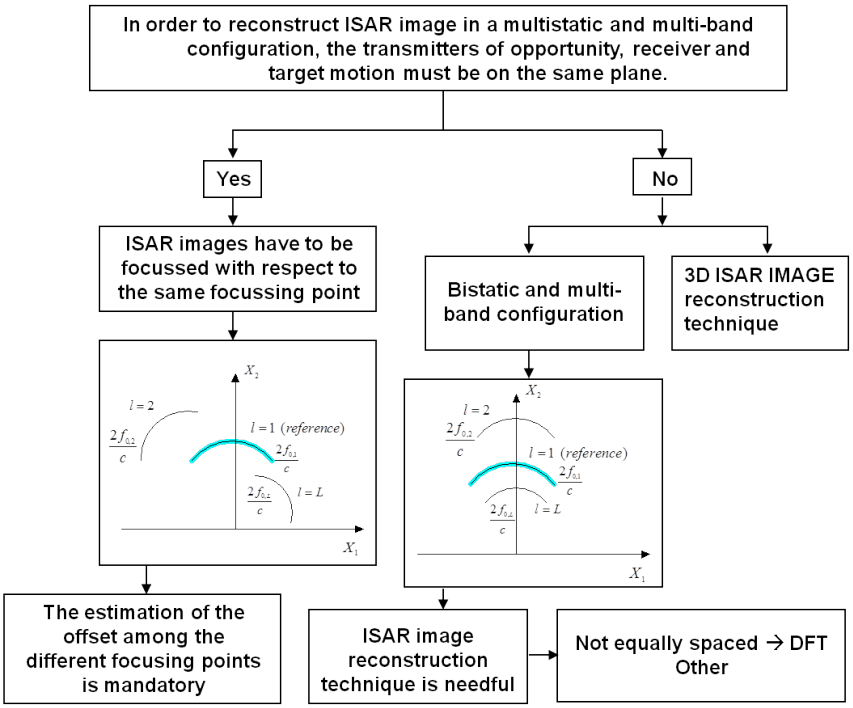


Figure 4.6: General ISAR processing flow chart

## 4.5 P-ISAR algorithm

Figure 4.7 shows the P-ISAR algorithm flow-chart used in this paper to process real data. The input of the processing chain is the RD map as produced by the CAF.

The signal containing the target's echo is extracted from the range-Doppler map after detecting the target. This procedure is carried out by selecting a rectangular window in the range-Doppler that contains the target's echo. This operation is essential because of the following reasons: a) Noise and clutter are strongly attenuated as only the components present in the range and Doppler cells where the target is contained are retained whereas the rest is filtered out; b) more than one target may be detected in the same range-Doppler map but only one target at a time can be processed by an imaging processor. The idea is to treat the RD image of the target as a unfocussed image. In fact, as

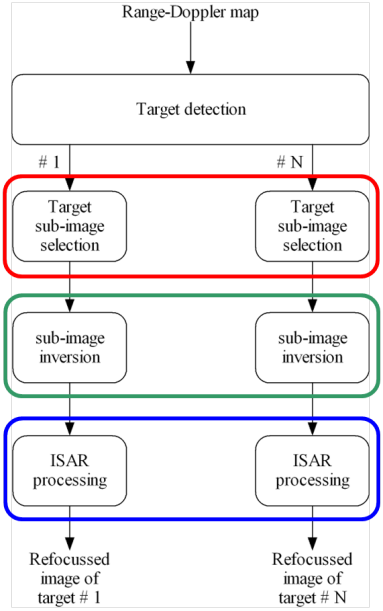


Figure 4.7: P-ISAR Algorithm flow chart

the target moves with respect to transmitter and receiver, it generates a non-stationary echo that does not map single scatterers in a stationary range and Doppler cell. This case could be compared to the case of SAR imaging, where the platform motion must be compensated for to map scatterer's echoes to the same range/azimuth cell to obtain a coherent integration for each image pixel. As the target motion is not known a priori, non-cooperative target imaging techniques must be employed, such as ISAR imaging [29,30]. ISAR processors are typically designed to work either in the fast-time/slow-time domain or in the frequency/slow-time domain. Therefore, the available data in the range-Doppler domain should be suitably transformed into one of the mentioned domains. This operation, in its most simple form, can be performed via FT, as shown in the case of non-cooperative target refocus in SAR images [19]. Once the data is transformed into a domain compatible with typical ISAR processor input, any ISAR processor may be used to form a focussed ISAR image of the target. Without loosing any generality, we will make use of the ICBA technique followed by a RD image formation [22]. To account for complex target motions, a time-windowing technique is also applied to the data to form well-focussed ISAR images [23]. Finally, the ISAR image is rescaled along the cross-range direction to obtain an image displayed in a spatial coordinate system [24]. More details can be found in [19], [31], [33].

### 4.5.1 Sub-image inversion

The natural input to an ISAR processor is data in the conjugate Fourier domain of the RD map, and not the RD map. Therefore the first step of the auto-focusing algorithm concerns the way of obtaining such a data from a RD map. The solution proposed consists of using a sub-image obtained by cutting a small area around the target and by inverting it in order to obtain an equivalent data containing only the targets echo and a little background noise. When the total aspect angle variation is not too large and when the effective rotation vector is sufficiently constant during the observation time, the RD technique represents an accurate and computationally effective tool for SAR/ISAR image reconstruction. Under this constraints, the polar grid in the spatial frequency domain (i.e. the conjugate Fourier domain of the ISAR image) can be assumed to be a nearly regularly sampled rectangular grid. Therefore, a two-dimensional Fast Fourier Transform (FFT) can be used to reconstruct the image. In this case the inversion algorithm consists of a Fourier Inversion, which is usually implemented via a two-dimensional Inverse Fast Fourier Transform (IFFT). This technique has been applied to SAR images of moving targets. The ISAR processor used to refocus moving targets is based on a RD approach. Specifically, a time window and an autofocus algorithm are applied to the data before using a 2D-FFT to form the target image. Autofocus [22], RD image formation and time-windowing [23]are briefly recalled below.

### 4.5.2 Autofocusing algorithm

Because of the relative motion between transmitter, receiver and target, the target may move through several range cells leading to a defocussed target radar image. The autofocus algorithm aims at removing the translational term due to the targets radial motion. This can be done by estimating the radial target motion parameters. By applying the far-field straight-iso-range approximation, the bistatic distance between the radar and the transmitter and receiver can be written as follows:

$$R_n(t) \cong R_A(t) + R_B(t) + |\mathbf{i}_{LOS-A}(t) + \mathbf{i}_{LOS-B}(t)|\mathbf{x} \cdot \mathbf{i}_{LOS-Bis}(t) \qquad (4.10)$$

where $R_A(t)$ and $R_B(t)$ are the distances between an arbitrary point on the target, namely the focusing point 0, and the transmitter and the receiver, respectively, $\mathbf{i}_{LOS-A}(t)$ and $\mathbf{i}_{LOS-B}(t)$ are the unit vectors that indicate the LoS for the transmitter and receiver, $\mathbf{x}$ is the vector locating an arbitrary scatterer and $\mathbf{i}_{LOS-Bis}(t)$ is defined as in equation 4.7.

The autofocus algorithm consists of removing the phase term $(2\pi f/c)[R_A(t)+R_B(t)]$ from the signal. For a relatively short observation time and a relatively smooth target motions, the distance $R_{Bis}(t) = R_A(t) + R_B(t)$ can be approximated by means of a quadratic form:

$$R_{Bis}(t) = R_{Bis}(t) + \nu_{rBis} \cdot t + a_{rBis} \cdot \frac{t^2}{2} \tag{4.11}$$

Where $\nu_{rBis}$ and $a_{rBis}$ are respectively the target velocity and acceleration components along the bistatic LoS, respectively.

The estimation of $R_{Bis}(t)$ resorts to the estimation of the target radial motion parameters. Let $\Theta = [\nu_{rBis}, a_{rBis}]$ be the vector containing the unknowns, the radial motion compensation problem can be recast as an optimization problem where the Image Contrast (IC) is maximized with respect to the unknown vector $\Theta$, as defined in 4.12

$$\hat{\Theta} = \arg\max_{\Theta} IC(\Theta) \tag{4.12}$$

where

$$IC(\Theta) = \frac{\sqrt{E\{[I(\Theta) - E[I(\Theta)]]^2\}}}{E[I(\Theta)]} \tag{4.13}$$

$E[\cdot]$ is the expectation operator and $I(\Theta)$ is the ISAR image magnitude after compensating the target motion by using $\Theta$. This can be expressed mathematically as in 4.14

$$I(\Theta) = \left| RD\left\{ S_{MF}(f,t) \cdot e^{-j\frac{2\pi f}{c} R_{Bis}(t)} \right\} \right| \tag{4.14}$$

Where $S_{MF}(f,t)$ is the signal in the data domain at the output of the matched filter, and $RD[\cdot]$ means the Range Doppler image formation, as clarified in the next section 4.5.3.

### 4.5.3 Image Formation

The image formation is based on a Fourier approach. RD images are formed by applying a 2D- FT to the motion compensated data. The Fourier approach can be applied when the total aspect angle variation is not too large and when the effective rotation vector is sufficiently constant. The effective rotation vector, namely $\mathbf{\Omega_{eff}}$, is the component of the target rotation vector, namely $\mathbf{\Omega_T}$, which contributes to the target aspect angle variation and therefore to the synthetic aperture formation. This latter can be obtained from the target rotation vector by applying a simple vector product, specifically,

$\mathbf{\Omega_{eff}} = \mathbf{i}_{LOS-Bis} \times (\mathbf{\Omega_T} \times \mathbf{i}_{LOS-Bis})$. Under these assumptions, the Doppler frequency of each scatterer which composes the target, can be considered constant, and the polar grid, where the data is defined, in the Fourier domain can be approximated with an uniformly sampled rectangular grid. Therefore, a two-dimensional FFT can be used to reconstruct the image. Let the complex valued ISAR image be defined as follows:

$$I(\Theta) = 2D - FT\{S_{MC}(f,t)\} \tag{4.15}$$

where $S_{MC}(f,t)$ is the signal after motion compensation, that is $S_{MC}(f,t) = S_{MF}(f,t) \cdot e^{-j\frac{2\pi f}{c}R_{Bis}(t)}$

### 4.5.4 Time Windowing

It has been stated, the RD technique can be successfully applied when the effective rotation vector does not change significantly during the observation time. However, the target's own motion may induce a non-uniform target's rotation vector. In order to minimize the target's rotation variation, CPI is controlled via a Time-Windowing approach. the technique used here is the automatic time-windowing technique proposed in [23], where an automatic selection of the time window is proposed. Specifically the time window position across the data and its length are automatically chosen in order to obtain one or more images with the highest focus. The criterion used to define the highest focused image is based on the IC. Therefore, the following optimization problem can be formulated

$$(\overline{t_{opt}}\ , \Delta t_{opt}) = \arg\max_{\bar{t}\ ,\Delta t}\{IC(\bar{t}\,\Delta t)\} \tag{4.16}$$

Because the variables $(\overline{t_{opt}}\ , \Delta t_{opt})$ are discrete, 4.16 represents a discrete optimization problem. Such a problem can be classified as a nonlinear knapsack problem. Such class of problems can be obviously be solved by using brute force. Nevertheless in order to avoid the use of an exhaustive search, in [23] a heuristic but effective method is proposed that is based on a double linear search.

### 4.5.5 Image Scaling

In order to determine the size of the target, it is preferable to have a fully scaled image. The range scaling can be performed by using the well known relationship $r = c\tau/2$, where $r$ is the range coordinate, $\tau$ is the time delay and $c$ is the light speed vacuum. On the other hand, cross range scaling requires

the estimation of the modulus of the target effective rotation vector. Recently, in [24] a novel algorithm is proposed to solve this problem. This algorithm is based on the assumption of quasi-constant target rotation. When the target rotation vector can be assumed constant within the coherent integration time, the chirp rate produced by the scattering centres can be related to the modulus of the target effective rotation vector by means of an analytical expression. Therefore each scattering centre carries information about the modulus of the target rotation vector through its chirp rate. The signal component of the scattering centres are therefore processed by means of a polynomial Fourier transform in order to estimate the chirp rate. The use of such a method, namely local polynomial Fourier transform (LPFT) requires the solution of an optimization problem. It has been largely proven in literature that the used of the IC and the Image Entropy (IE) are good parameters to assess the quality of the reconstructed ISAR image. In the proposed algorithm the IC will be used as a cost function to be maximized for estimating scattering centres chirp rate.

## 4.6 DVB-T signals and high range resolution

The DVB-T signal is organized in COFDM frames. Each frame consists of 68 OFDM symbols. Each symbol is formed by a set of data sub-carriers, pilots sub-carriers and Transport Parameter Signaling (TPS). The pilot and TPS sub-carriers are used for receiver synchronization and transmission parameter estimation, respectively [28]. The modulation power of scattered pilots have an average power that is higher than data sub-carriers. These pilots cause Doppler and range ambiguities that can be attenuated by applying a signal processing technique as presented in [16] . The range resolution improvement can be obtained by coherently adjoining more DVB-T signals from the same illuminator of opportunity and by processing such a signal as a single wideband signal. Figure 4.8 shows the autocorrelation function of a single channel DVB-T signal with a dashed line and a three-channel DVB-T signal with a solid line. The resolution improvement is clearly visible by comparing the main lobe width in both cases. The three DVB-T channels which compose the wideband signal, are transmitted by the same IO. Adjacent DVB-T channels are separate by gaps where no signal is transmitted. Such gaps are due to the DVB-T frame and are useful in order to reduce the cross-interference between adjacent channels and therefore in order to improve the quality of the transmitted signal. In the Italian DVB-T standard, 6817 among the available 7168 sub-carriers are used to transmit [16]. Therefore the gap between two adjacent DVB-T channels is of the order of 5% of the signal's spectrum. A passive radar generally presents

two receiving channels denoted as reference channel and target channel. The reference channel is used to capture the direct signal from the transmitter and provides a reference signal to be compared with the echo reflected by the target towards the surveillance antenna. The comparison is usually carried out by cross-correlating the reference and the target signals. Because either the target or the receiver or both may be moving during data acquisition a Doppler effect may be generated. To take into account such an effect, the cross-correlation is carried out by shifting the reference signal both in time and frequency. The result of this cross-correlation has been addressed in the literature as the CAF, which produces a range-Doppler map. The analytical expression of the CAF is shown in equation 4.17.

$$\chi(\tau,\nu) = \int s_{surv}(t) s^*_{ref}(t-\tau) e^{j2\pi f_d t}\, dt \tag{4.17}$$

where $s_{surv}(t)$ is the surveillance channel, $s_{ref}(t)$ is the refence channel,$f_d$ is the Doppler frequency, $\tau$ is the target delay time and $T_{obs}$ is the integration time. The 2-D function $\chi(\tau,\nu)$ is the input of the processing chain Passive Bistatic ISAR algorithm.

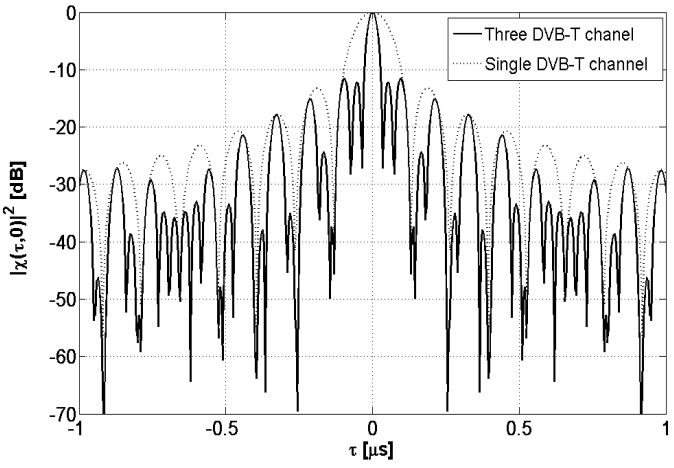


Figure 4.8: DVB-T ambiguity function

## 4.7 Grating Lobes Cancellation Algorithm

As mentioned before, a wide bandwidth signal can be obtained by adjoining adjacent DVB-T channels. To reduce cross-channel interference, DVB-T channels are separated by gaps where no signal is transmitted. Such gaps,

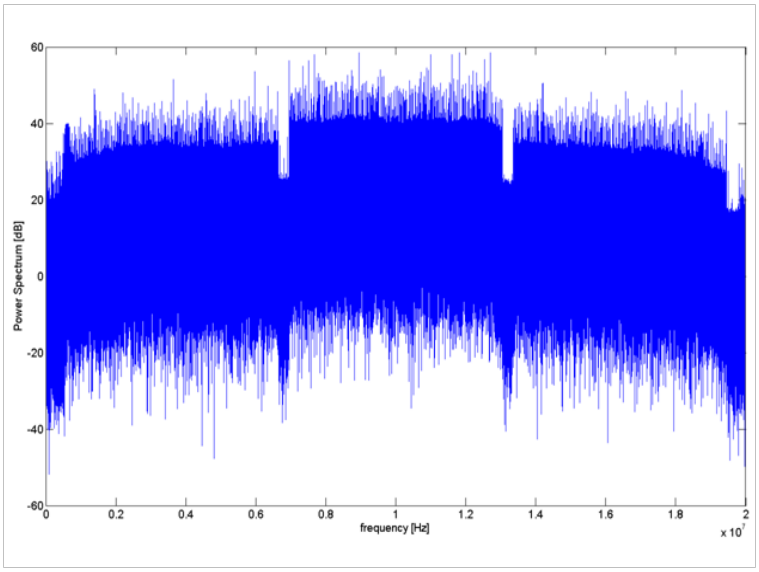


Figure 4.9: Spectrum of the multi-channel DVB-T signal

although necessary to guarantee high quality TV transmission, generate unwanted artifacts when multiple DVB-T channels are used for radar purposes. An example of a measured spectrum composed of three adjacent DVB-T signals is shown in Figure 4.9. As shown in Section 4.6 and displayed in Figure 4.8, the autocorrelation function of three adjoined DVB-T signals shows a resolution improvement equal to the number of channels. Nevertheless, it should be noted that gratings lobes appear close to the main lobe, which are due to the presence of gaps in the spectrum. Such grating lobes may be interpreted as additional scatterers in an ISAR image.

The problem of filling out spectral gaps has been already addressed in the literature. Particularly, in [34], a procedure to fill out the gaps formed by missing data is presented. The paper deals with the problem of sparse aperture collected data in active SAR imaging. In [35], a technique to extrapolate the spatial spectrum in both azimuthally and range directions so as to fill out the gaps is presented. Both papers are based on the Super - Spatial Variant Apodization (S-SVA) algorithm because a bandwidth extrapolation is needed in order to fill the wide gaps due to missing spectral components in active SAR applications. The procedure implemented in this paper has been designed for a P-ISAR scenario where the multichannel DVB-T spectral notches are quite small with respect to the signal bandwidth. In fact, the signal bandwidth is $7.61MHz$ while the canalization is equal to $8MHz$. In such conditions, a procedure based on a modification of the SVA algorithm proves satisfactory. Further details on the SVA algorithm, as mathematical discussion, can be

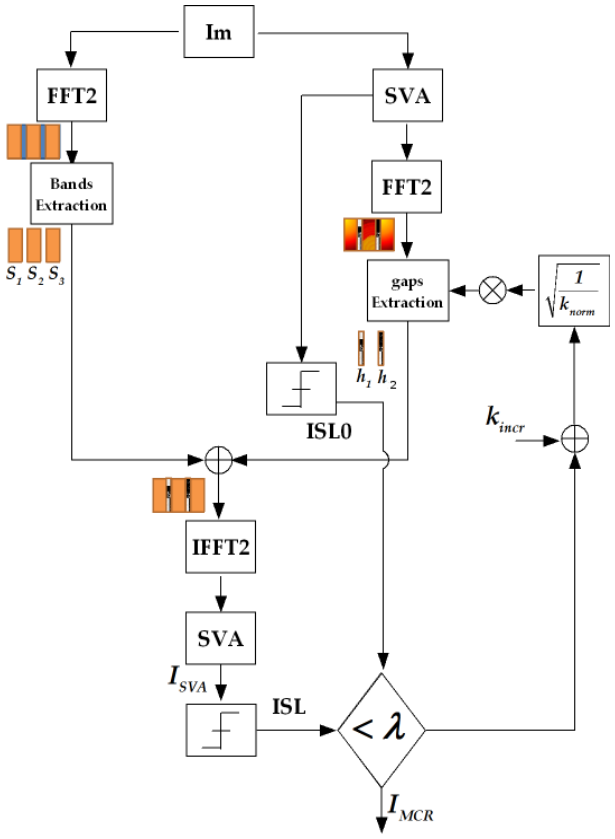


Figure 4.10: Algorithm flow chart of the Grating Lobe cancellation procedure

found in [32].

The flow chart of the proposed technique for the grating lobes cancellation is depicted in Figure 4.10.

The input of the algorithm is the P-ISAR image of the target at the output of the P-ISAR processor. The first step of the algorithm concerns the extraction of the spectral bands where the DVB-T signal is present . This is performed by back-projecting the ISAR image onto a raw data like domain and by selecting only the "useful" spectral content of the signal (spectral notches are filtered out). A SVA algorithm is applied in parallel to the same ISAR image and a two-dimensional Fourier transform 2D-FFT is performed. Since the SVA algorithm performs a bandwidth extrapolation, a partial filling of the gaps can be observed after this stage. At this point, the signal present in the spectral notches is selected and added to the useful signal, therefore performing a first gap filling. More spectral components may be pouring into the gaps by iterating this approach. Nevertheless, in order to reduce the number of iterations, the signal present in the gaps is multiplied by a normalization

factor, which is defined in equation (4.18)

$$k_{norm} = \frac{1}{2}\frac{\sum_{g=1}^{G} P_{Hg}}{\sum_{b=1}^{B} P_{Sb}} \tag{4.18}$$

where, $G$ is the number of bandwidth gaps, $B$ is the number of DVB-T channels, $P_{Hg}$ and $P_{Sb}$ are given by Equations (4.19),(4.20) respectively,

$$P_{Hg} = \frac{1}{NM}\sum_{j=1}^{N}\sum_{k=1}^{M}|h_g(j,k)|^2 \tag{4.19}$$

$$P_{Sb} = \frac{1}{NM}\sum_{j=1}^{N}\sum_{k=1}^{M}|S_b(j,k)|^2 \tag{4.20}$$

where $N$ and $M$ are the number of image rows and columns, respectively, $|h_g|$ is the extracted sub-band containing the gap and $|S_b|$ is the extracted sub-band containing the useful data. The normalization factor is used as a sort of image equalization, where the energy in the gaps (already partially filled at this step) is equalized to that of the useful bands. As a consequence, the Integrated Side Lobe level (ISL) of the equalized image becomes smaller than that of the non-equalized image.The re-combined spectral content is than remapped onto the ISAR image domain by means of a 2D-IFFT. A SVA iteration is finally performed to obtain the final apodized ISAR image. For the sake of completeness, the ISL is defined as follows:

$$ISL = 10log_{10}(\frac{\sum_{n\ni D}|I_{SVA}(n)|^2}{\sum_{n\in D}|I_{SVA}(n)|^2}) \tag{4.21}$$

where D is a two-dimensional mask that selects only the pixels belonging to the target. By applying such a mask, all pixels not belonging to the target are classified as image side lobes. The symbol $I_{SVA}$ represents the ISAR image, after applying the SVA and adjoining the useful bands to the filled out gaps. Finally, the ISL is compared with a threshold $\lambda$, where $\lambda$ is defined in equation (4.22)

$$\lambda = ISL0 + (\frac{10 * ISL0}{100}) \tag{4.22}$$

and where $ISL0$ is the integrated side lobe level of the data after the first apodization (see figure 4.10). If the ISL is smaller than $\lambda$, the final ISAR image $I_{MCR}$ is generated, otherwise further iterations are carried out. At each iteration, the normalization factor increases by a factor $k_{incr}$. The value of $k_{incr}$

is a trade off between the algorithm computational time and the accuracy of the estimated ISL, and it is a real number within the range $[0, 1]$. After each iteration, a smaller value of ISL is obtained until it becomes smaller than the preset threshold. The threshold $\lambda$ is defined as in equation (4.22), in order to obtain an image with a small ISL. Let consider the effect on a weak point target nearby a strong one. For such reason, a target with the geometry depicted in figure 4.11 has been simulated.

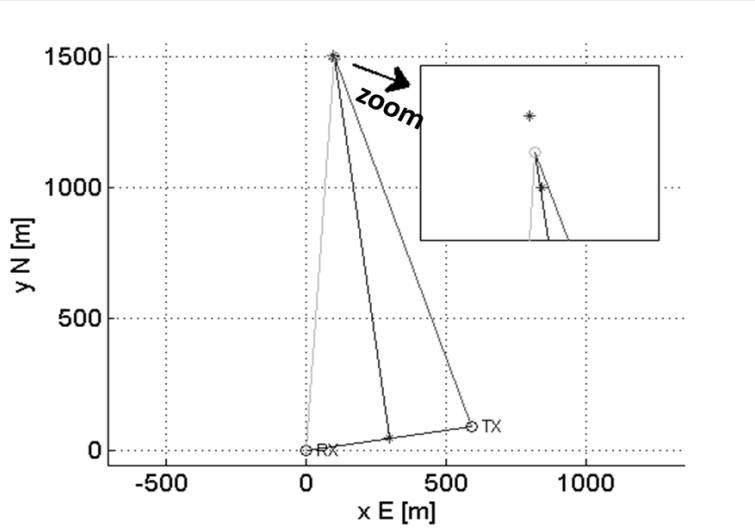


Figure 4.11: Simulation Geometry

The target is composed by two point-like scatterers apart $15m$ from each other in the range dimension, and with the amplitude of the scatterer one twice of the other one. The geometry is designed in order to obtain the projection of the target almost totally oriented in the range direction. The target moves with the same parameters used for the simulation in [32] . After the focusing procedure the result depicted in figure 4.12 is obtained. Such focused target is the input for the Grating Lobe Cancellation (GLC) algorithm, which provides the result shown in figure 4.13.

By comparing figures 4.12 and 4.13 can be figured out how the grating lobes level has been drastically reduced. Furthermore, Both scatterers are hereby acknowledged even though the scatterer with half amplitude of the other one is the most affected by the cancellation procedure. This fact does not occur if both scatteres have equally amplitude, as figure 4.14 and 4.15 demonstrate.

In fact, figures 4.14 and 4.15 show that both the scatterers are almost equally treated by the cancellation procedure.

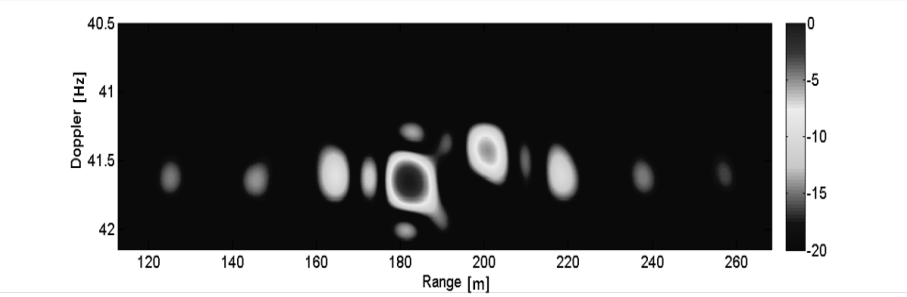


Figure 4.12: P-ISAR image before the GLC algorithm in the case of the scatterers with different amplitude

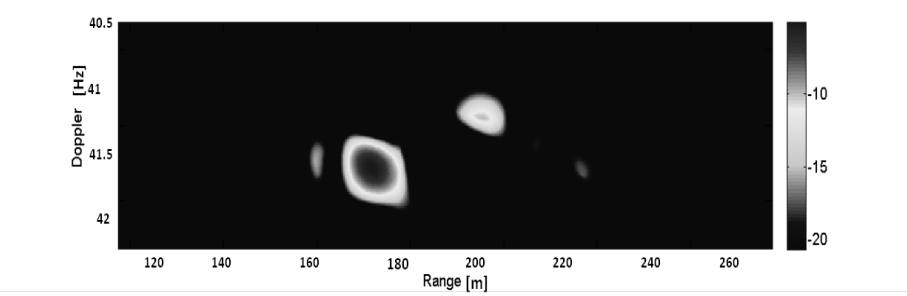


Figure 4.13: P-ISAR image after the GLC algorithm in the case of the scatterers with different amplitude

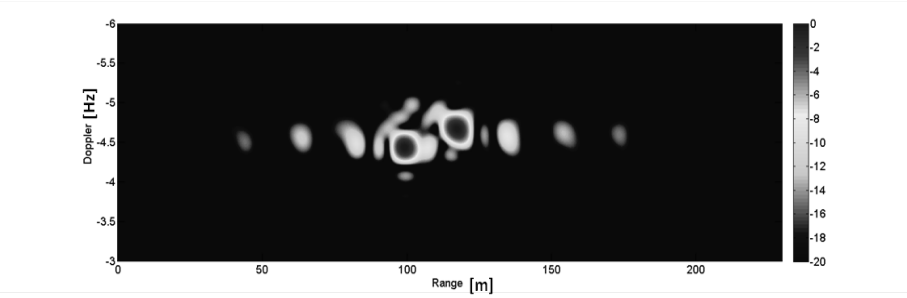


Figure 4.14: P-ISAR image before the GLC algorithm in the case of the scatterers with equal amplitude

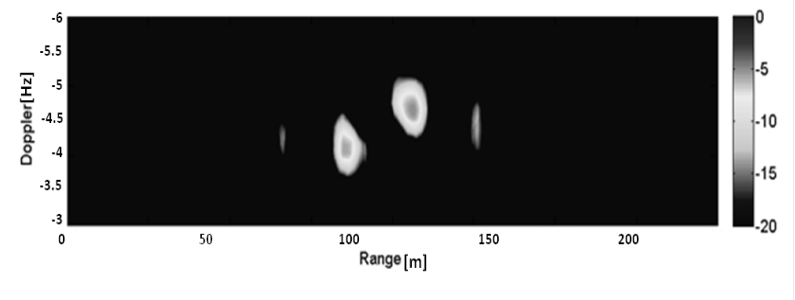


Figure 4.15: P-ISAR image after the GLC algorithm in the case of the scatterers with equal amplitude

# Chapter 5

# Numerical Results on Simulated Data

In this chapter some numerical simulations are presented in order to identify which are the capabilities of the Passive Isar Imaging. The real data, which will shown in the next chapter, have been acquired with only three adjacent DVB-T channels, for an observation time of a few seconds, due to the hardware limitations. In contrast to them, with simulated data we can try to push to the limit the Passive Isar imaging performance in order to understand its potentiality.

## 5.1 Isar Imaging results on aerial targets

### 5.1.1 CESSNA 172 target

The target is a point-like scatterer model of a CESSNA 172, as shown in figure 5.1, where the top view and side view of the target are shown. The data have been generated by using 10 adjacent channels, therefore the total bandwidth is $B = 80MHz$, so that the range resolution is of the order of about $2m$.

In order to achieve high cross-range resolutions, the target has to be illuminated for a long time. A data 60 seconds long has been generated in order to achieve a cross-range resolution less than $2m$. In order to save computation resources, the data has been generated so as to emulate a pulsed radar, instead of a continuous wave radar. Specifically, the data consists of 60 received pulses, with an observation time of $200ms$ and a Pulse Repetition Interval (PRI) of $1s$ . Then, a range Doppler map for each PRI is computed. After the extraction of the target from each range-Doppler map, a Doppler Fourier inversion

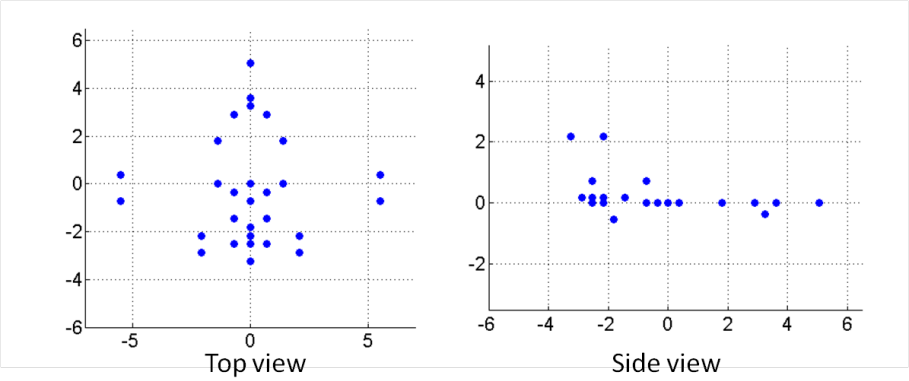


Figure 5.1: Point-like scatterer model of a CESSNA 172

is performed. Then, the same range profile from each data is selected such that the collected profiles will be one second distant each other. The obtained data represent the one second sampled bistatic range history of the target in the whole observation time. A further Fourier Transform along range coordinate transforms the data into a frequency-time format, which is the input data for the ISAR imaging algorithm. The main steps of the ISAR imaging preprocessing chain is reported in figure 5.2.

The simulations have been done to verify if good range and cross range resolutions could be fine enough to obtain a well defined target's image, by fixing the geometry and therefore the trajectory 5.3 of the target.

The total rotation vector of the target and, as consequence, the effective rotation vector has been estimated. Knowing these parameters, both the cross range resolution and the Image Projection Plane (IPP) can be calculated. Therefore a point-like model of the target has been projected on the IPP. Figure 5.4 shows the point-like scatterer target projected onto the estimated image plane, in the range-cross range plane and in the range-Doppler plane respectively.

The coefficient of scale between Doppler and cross-range is:

$$\delta_{cr} = \frac{c}{2f_0\Omega_{eff}\delta_{dopp}} \tag{5.1}$$

The estimated cross range resolution is $\delta_{cr} \cong 1.67m$ , 5.4(a). As it can be noted, 5.4(b) the target size in Doppler dimension is $\Delta_{dopp} \cong 0.084Hz$. It's worth noting that the target's Doppler size is smaller than the inverse of the PRI, that is the Doppler unambiguous window. This condition should be satisfied in order to avoid any aliasing effect. The Doppler resolution of the synthetic data is $\delta_{dopp} = \frac{1}{T_{obs}} \cong 0.0169Hz$.

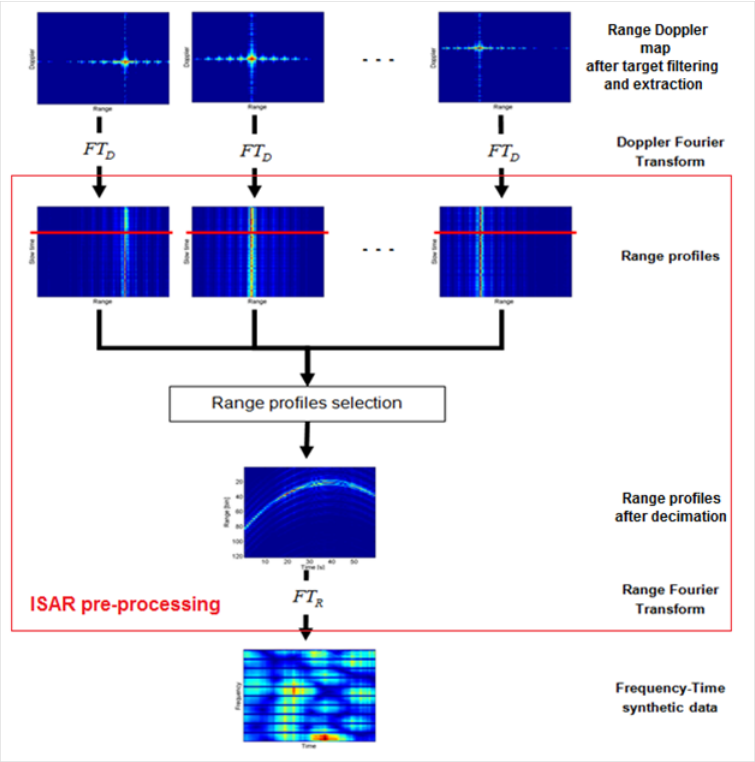


Figure 5.2: Block scheme of the pre-processing used for simulating the theoretical scenario (sub-image inversion of the figure 4.7

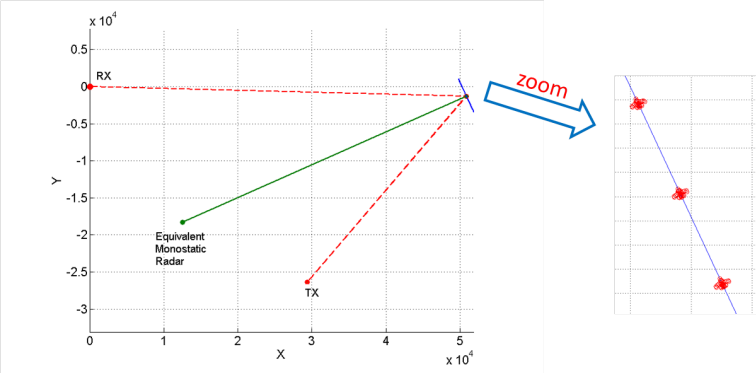


Figure 5.3: Bistatic geometry and zoom of the trajectory of the target

The images in figure 5.5 have been obtained by compensating the signal with the well known radial motion parameters, without using any kind of focusing algorithm. As it can be seen, the image is affected by quite high side lobes level in the range direction due to the DVB-T waveform framework,

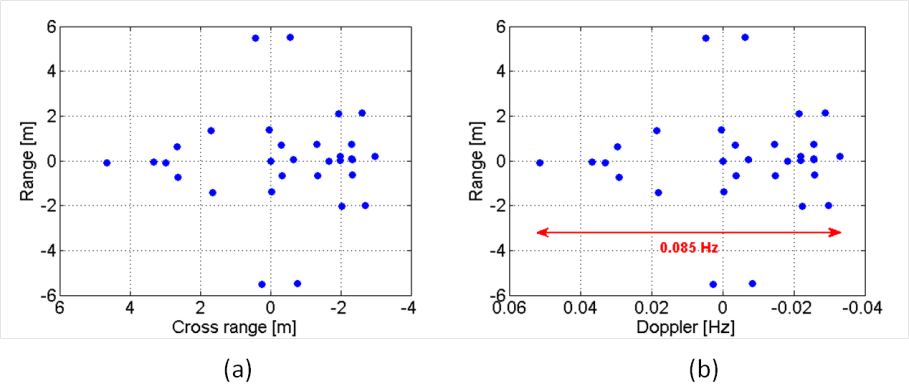


Figure 5.4: Target projected onto the estimated image plane (a) range-cross range (b) range-Doppler

specifically to the virtual carriers between adjacent channels.

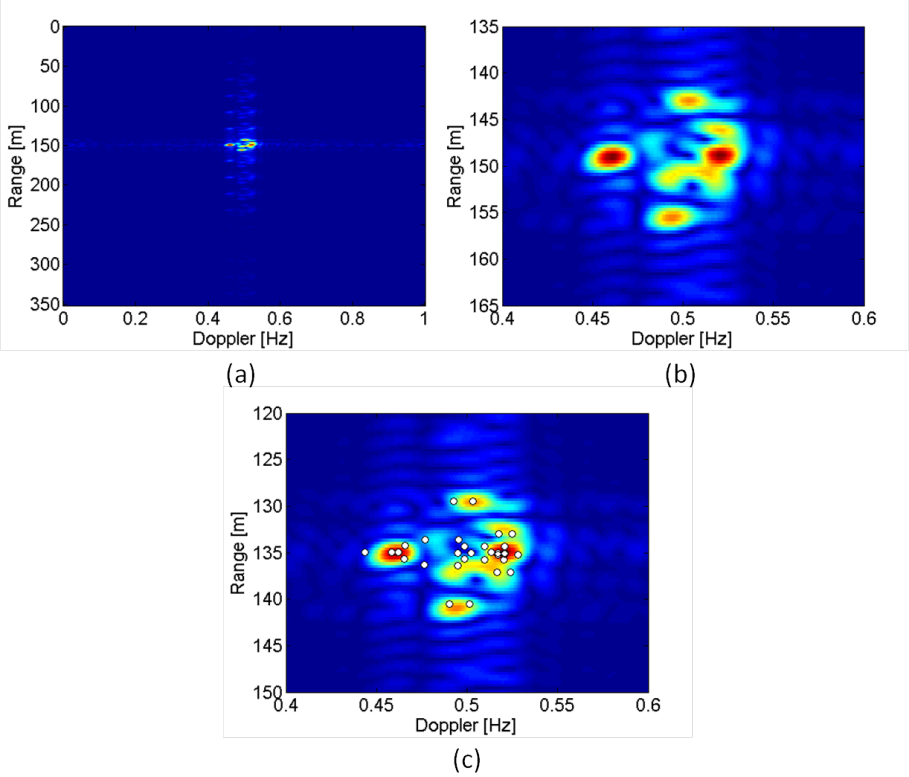


Figure 5.5: (a)-Target's ISAR image after focusing with known radial motion parameters (b)- zoom of the ISAR image (c) - zoom of the ISAR image with the superimposed point-like scatterers

In Figure 5.6 the obtained results by focusing the received signal with the autofocusing algorithm (see 4.5.2) are showed. When the total aspect angle variation is quite small, and the target rotation vector is considered constant during the observation time, the proposed ISAR algorithm is able to form a well focused image of non-cooperative targets. The estimated target's size along the Doppler axis is about $0.08Hz$, as expected. When the cross range scaling is performed on such data, because of the small size of the target, the following problems arise:

- The number of available scatterers to estimate the chirp rate is not sufficient to perform a good estimate of the effective rotation vector.
- Different scatterers with the same amplitude belong to the same range resolution cell, as a consequence, the estimated chirp rate results in a combination of such scatterers.

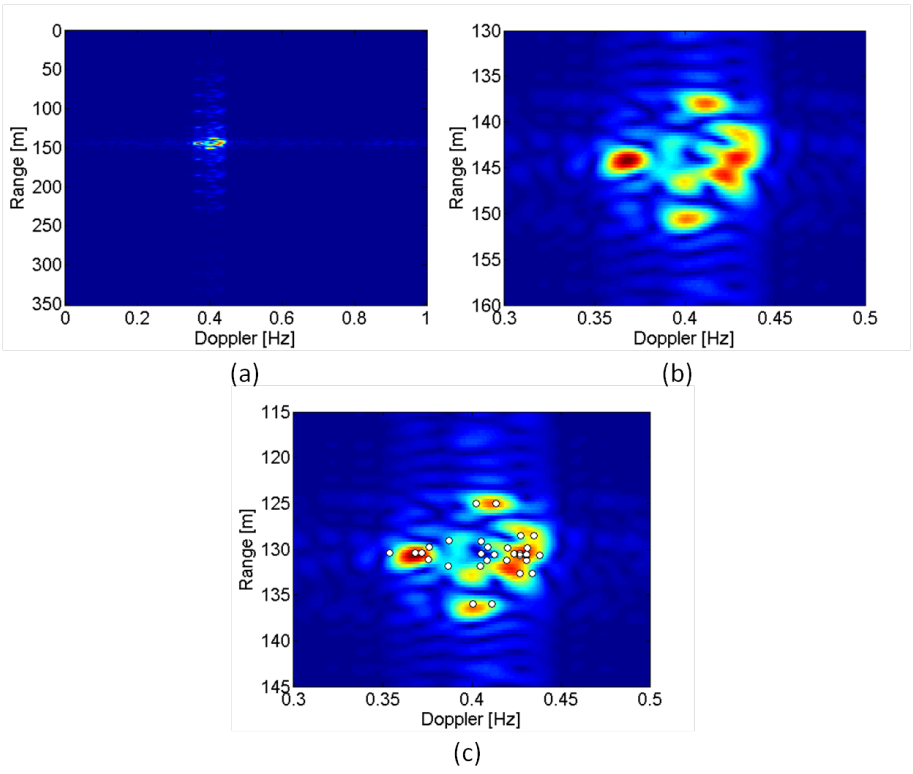


Figure 5.6: (a)-Target's ISAR image after focusing processing (b)- zoom of the ISAR image (c) - zoom of the ISAR image with the superimposed point-like scatterers

### 5.1.2 BOEING 747 target

The target is a point-like scatterer model of a BOEING 747, as shown in figure 5.7, where the top view and side view of the target are shown. Two simulations have been run that differ only by the number of adjacent DVB-T channels. This has been done with the aim of determining the minimum number of channels needed for a good understanding of middle sized targets. Specifically the first has been run by using 10 adjacent channels, the latter by using 3 adjacent channels. The expected range resolutions are about $2m$ and $6.8m$, respectively.

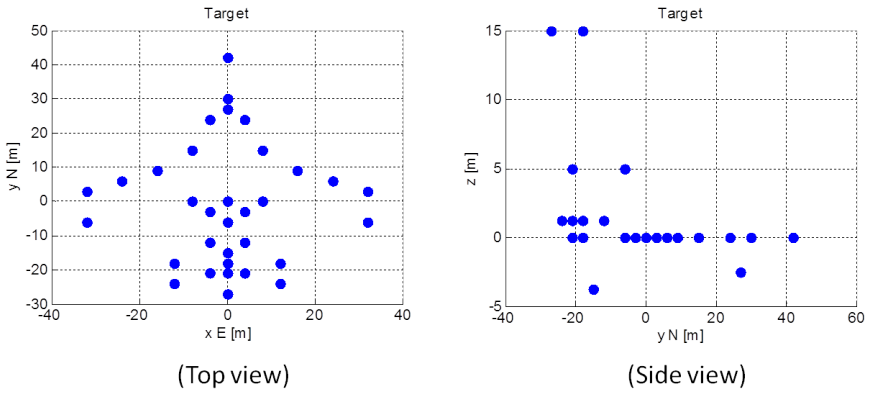


Figure 5.7: Point-like scatterer model of the Boeing 747 (a)-Top view (b)-Side view

The geometry is the same the previous case 5.3, only the target changes. Both the total rotation vector of the target and the effective rotation vector have been estimated. Therefore the cross range resolution and the IPP can be calculated. Figure 5.8 shows the point-like scatterer target projected onto the estimated IPP, in the range-cross range plane and in the range-Doppler plane respectively. The estimated cross range resolution is $\delta_{cr} \cong 1.93m$ , 5.8(a). As it can be noted, 5.8(b) the target size in the Doppler dimension is $\Delta_{dopp} \cong 0.5Hz$. The Doppler resolution of the synthetic data is $\delta_{dopp} = \frac{1}{T_{obs}} \cong 0.0208Hz$.

In Figure 5.9 the result obtained by using the proposed autofocusing 4.5.2 algorithm are shown. Specifically, figure 5.9-(a) show the ISAR image of the target obtained by exploiting 10 adjacent DVB-T channels, while figure 5.9-(b) that with 3 adjacent DVB-T channels. The estimated target size along the Doppler axis is $0.5Hz$ , as expected. As it can be noted, the shape of the target is well recognizable also by using 3 adjacent DVB-T channels. However, it is important to recall that a point-like model of the target has been used for the simulation . This hypothesis is valid when the scattering centers of the targets are larger than the wavelength and when each scattering center

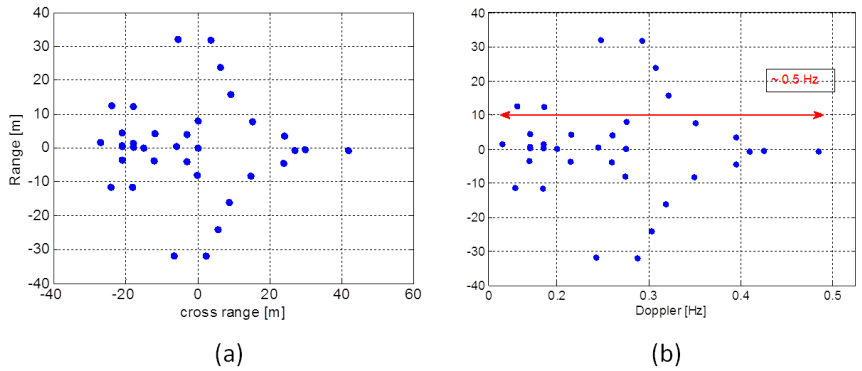


Figure 5.8: Target projected onto the estimated image plane (a) range-cross range (b) range-Doppler

is far from the other at least 10 times the wavelength. By considering the used frequencies and the middle sized target, these hypotheses could not be satisfied. Because of this, and because of shadowing and the back-scattering properties of the target, the actual ISAR image obtained by processing real data could be slightly different with respect the expected one. Therefore, it can be concluded that in order to obtain understandable ISAR images of middle sized targets, at least 3 adjacent DVB-T channels are necessary.

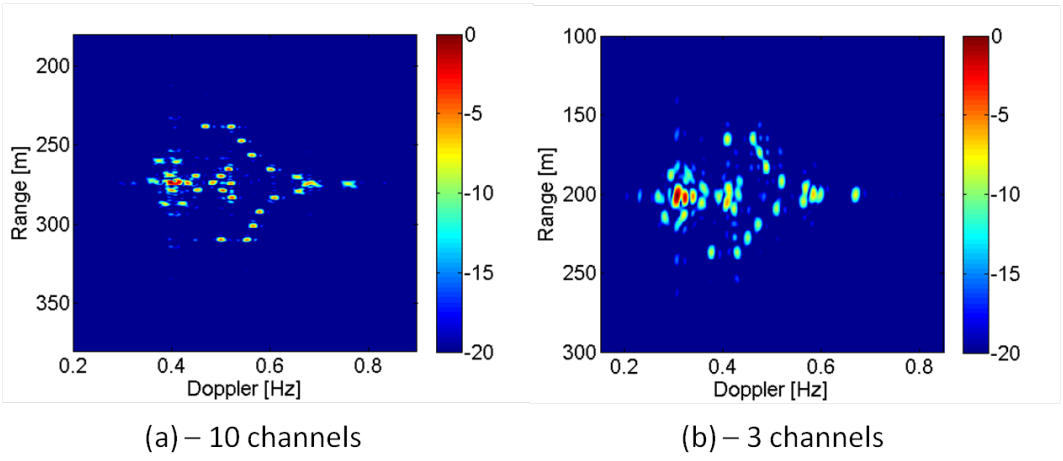


Figure 5.9: Target's ISAR image of the Boeing, obtained by exploiting (a)- 10 channels (b)- 3 channels

In this case, the size of the target is bigger than the previous one, so the cross range scaling algorithm can be applied. Particularly, in the figure 5.10 are shown the extracted scatterers and the regression line (red) with the estimated

chirp rate of each scattering center (blue dots).

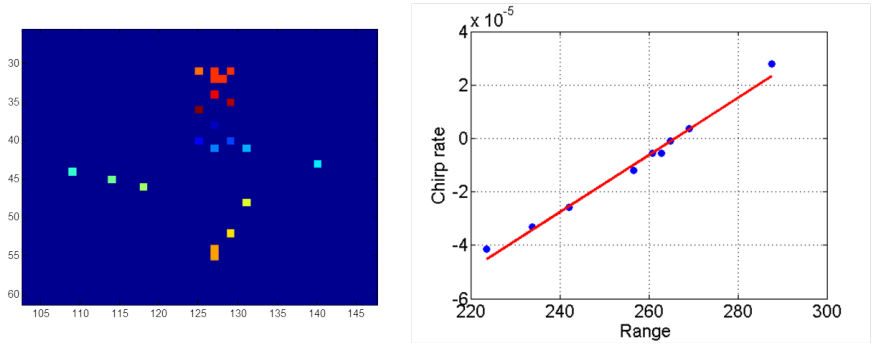


Figure 5.10: (a)- Extracted scatterers of the target (b)- Regression line of the Cross range scaling algorithm

These results are obtained by processing the ISAR image in figure 5.10-(a). As can be noted, the estimates fit the line well, therefore a good cross range scaling is expected. Similar results are obtained by processing the ISAR image in figure 5.10-(b). Figure 5.11 shows the fully scaled ISAR images of the target, in both cases.

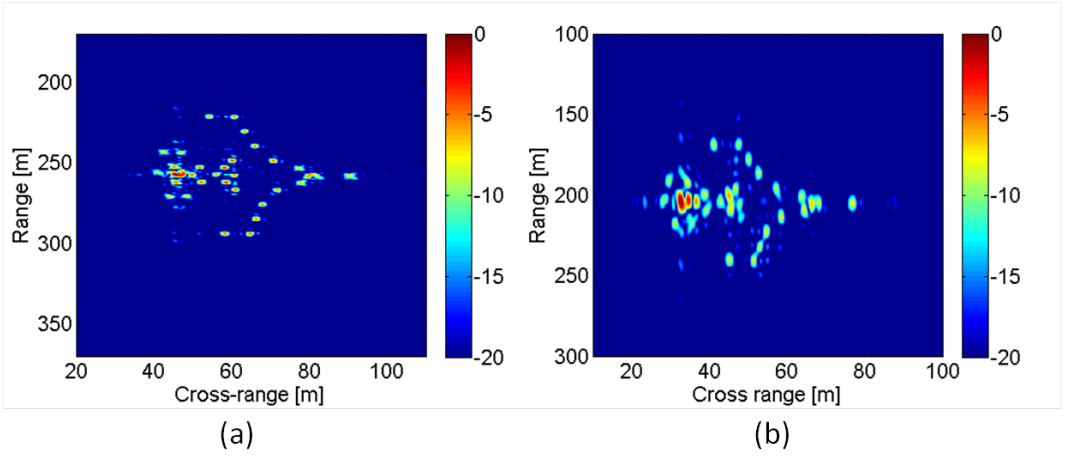


Figure 5.11: Fully scaled ISAR images of the target (a) - 10 channels (b) - 3channels

The size of the target are well reconstructed. It's worth noting that because of the bistatic geometry (i.e. due to the factor $K(t) = K(0)$ of the eq. 4.6 evaluated in the central instant t=0) and because of the projection onto the image plane, the size of the target are slightly different from the actual

dimensions. As already stated, the image is affected by quite high side lobes level in range direction due to the DVB-T waveform framework. Such lobes are rather grating lobes, which are due to the bandwidth gaps of the multi-channel DVB-T signal 4.7.

## 5.2 Isar Imaging results on maritime targets

The wide-band signal we simulated is composed by three adjacent DVB-T channels 4.9, for a totally bandwidth of $24MHz$, letting us to achieve a theoretically $6.25m$ of range resolution, in a mono-static condition. A quasi-monostatic configuration is performed in order to obtain a range resolution as close as possible to the monostatic maximum achievable range resolution, and also to contain the bistatic angle variation. The target used for the following simulation is represented in 5.12 where the top view and the side view of it are shown. The target is a point-like ship composed of 67 ideal point scatterers. The target is 250 m long, 50 m wide and 50 m high. The target motion is composed of a translational motion and angular motions, due for example to the sea state and to maneuvers. Specifically the target moves along a rectilinear trajectory with constant velocity $v = 21.6\,NM$, whereas the angular motions has been modeled as

$$\Omega(t) = \begin{bmatrix} \Omega_{roll}(t) \\ \Omega_{pitch}(t) \\ \Omega_{yaw}(t) \end{bmatrix} = \begin{bmatrix} A_r\omega_r cos(\omega_r t + \phi_r) \\ A_p\omega_p cos(\omega_p t + \phi_p) \\ A_y\omega_y cos(\omega_y t + \phi_y) \end{bmatrix} \tag{5.2}$$

Two different target trajectories have been considered in order to verify if the size of the target is well estimated.

**Experiment 1**

The geometry used in the simulation is represented in 5.13. The parameters used in this experiments are listed in 5.1

5.14 shows the ambiguity function at the input of the ISAR processing and in the bottom left corner the target sub image obtained by cropping a small area around it. Figure 5.15 shows instead the target ISAR image after the proposed algorithm, obtained by processing all the available data and therefore without using the time windowing approach. The target width is estimated to be about 55 m. The ISAR image obtained and plotted in 5.15 is well focused and the main scatterers are clearly visible. However, as evidenced in the ISAR image, side lobes are very high along the range coordinate. Such sidelines are due to the multichannel DVB-T waveform characteristics and cannot be easily

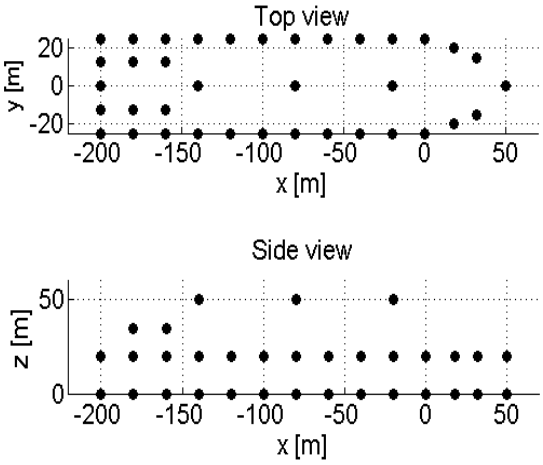


Figure 5.12: target

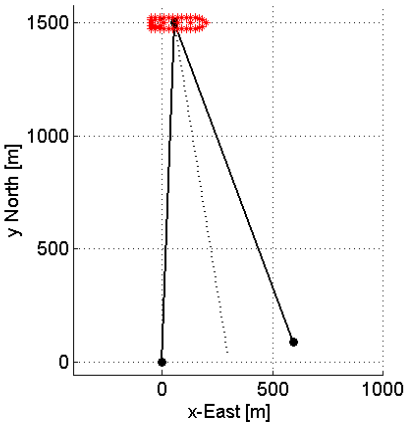


Figure 5.13: geometry

Table 5.1: Radar parameters

| | |
|---|---|
| $f_0$ | 800 MHz |
| $B$ | 24 MHz |
| $T_{obs}$ | 4 sec |
| $v$ | 21.6 NM |
| $(A_r, A_p, A_y)$ | (0,0,0.1) rad |
| $(\omega_r, \omega_p, \omega_y)$ | $(0, 0, \frac{2\pi}{20})$ |
| $(\phi_r, \phi_p, \phi_y)$ | $(0, 0, 0)$ |

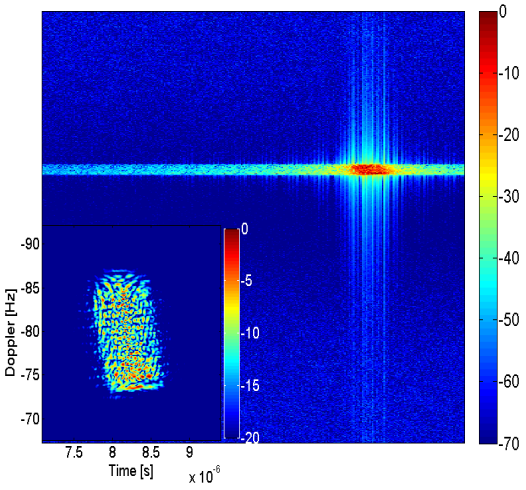


Figure 5.14: target sub image

Table 5.2: Radar parameters

| | |
|---|---|
| $(A_r, A_p, A_y)$ | (0,0,0.3 ) rad |
| $(\omega_r, \omega_p, \omega_y)$ | $(0, 0, \frac{2\pi}{30})$ |
| $(\phi_r, \phi_p, \phi_y)$ | $(0, 0, 0)$ |

reduced with simple weighting functions without trading it off with a significant loss of resolution. The Grtaing Lobe Cancellation algorithm4.7 addresses ans solves this issue.

### Experiment 2

The geometry used in the simulation is represented in 5.16. The parameters used in this experiment differ from the previous parameters only for the target angular motions which are reported in 5.2.

5.17 shows the ambiguity function at the input of the ISAR processing and in the bottom left corner the target sub image obtained by cropping a small area around it.

5.18 and 5.19 show instead the target's ISAR image after applying the proposed algorithm by using the all amount of data and by using the time windowing approach, respectively. As the target's own motion induce a non uniform target's rotation vector, the ISAR image obtained by processing all the available data is unfocused yet. A more focused ISAR image is obtained by controlling the CPI via a the time windowing approach 4.5.4.

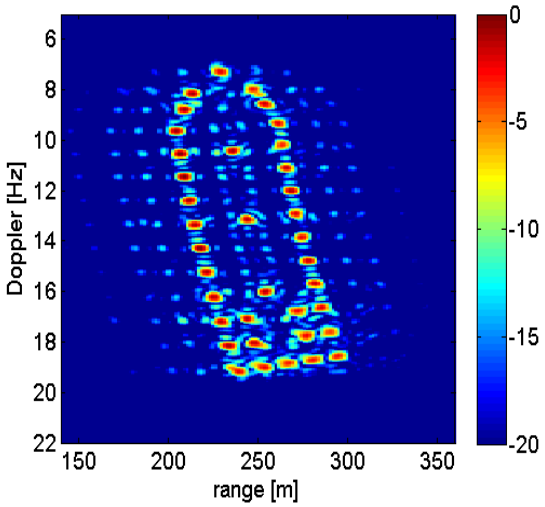


Figure 5.15: target ISAR image

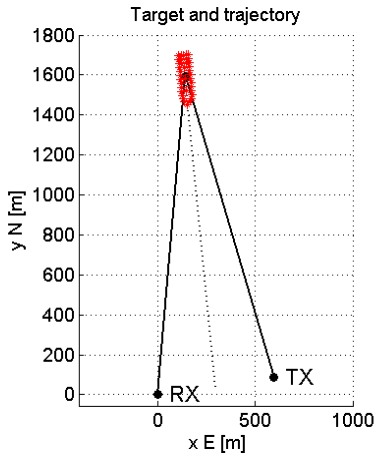


Figure 5.16: geometry

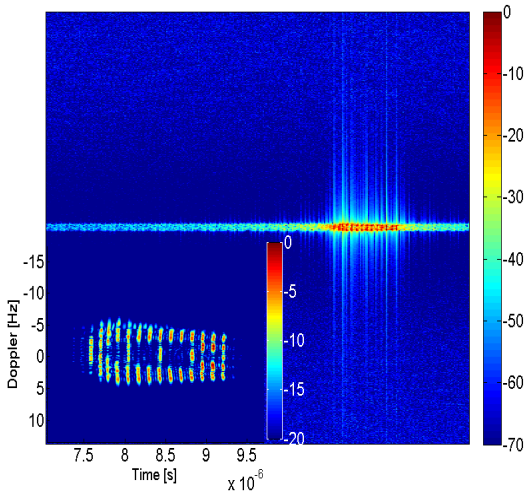


Figure 5.17: target sub image

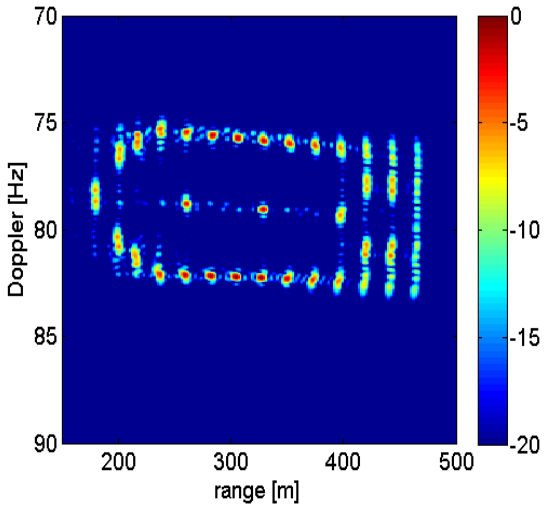


Figure 5.18: target ISAR image

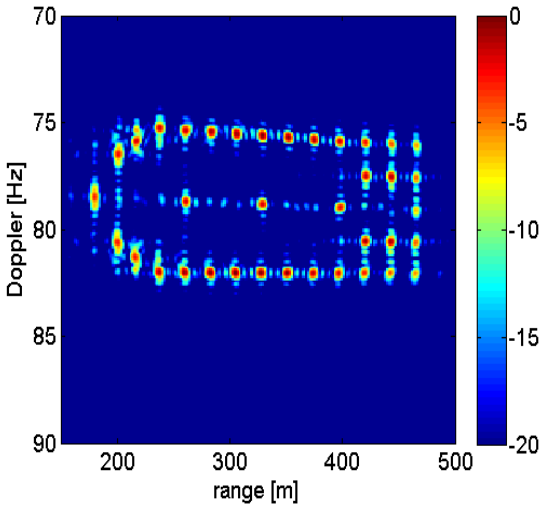


Figure 5.19: target ISAR image obtained by using the time windowing algorithm

## 5.3 Performance of the Grating Lobes cancellation algorithm

The cancellation algorithm is performed to the simulated P-ISAR image of figure 5.15, which its own spectral content is shown in figure 5.20. As can be noted the bandwidth gaps are clearly visible. In Figure 5.21 the P-ISAR image after the SVA algorithm is shown. It is worth noting that the grating lobes are still high even if they are slightly reduced. In figure 5.22 the relative spectrum is depicted, where the spreading that partially fill the gaps can be noted. In figure 5.23 the final result after the grating lobes cancellation algorithm is shown. As can be figured out the grating lobes are totally reduced by filling the gaps of its relative spectral content, as shown in figure 5.24.

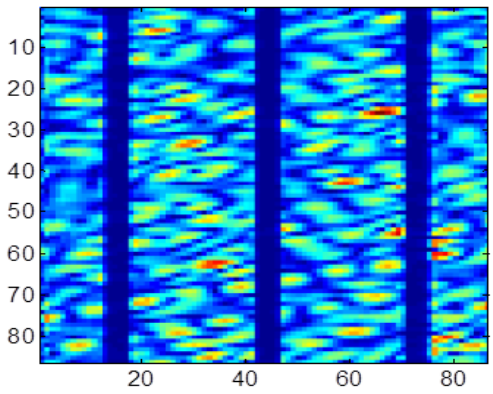


Figure 5.20: Spectral content of the signal before to fill out the gaps

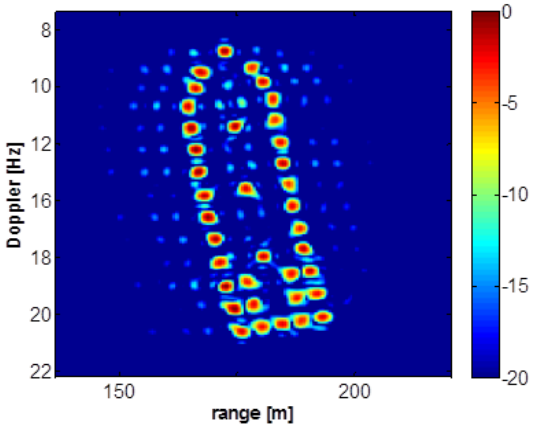


Figure 5.21: P-ISAR image after the SVA algorithm

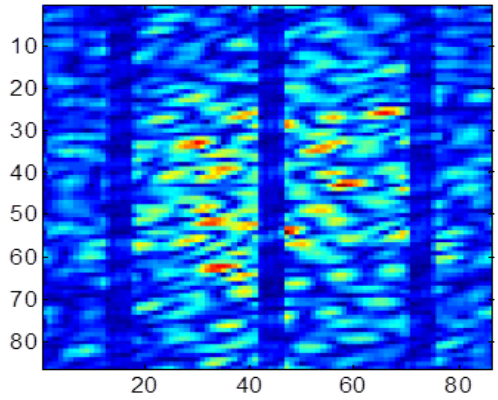


Figure 5.22: Spectral content of the P-ISAR image after the SVA algorithm

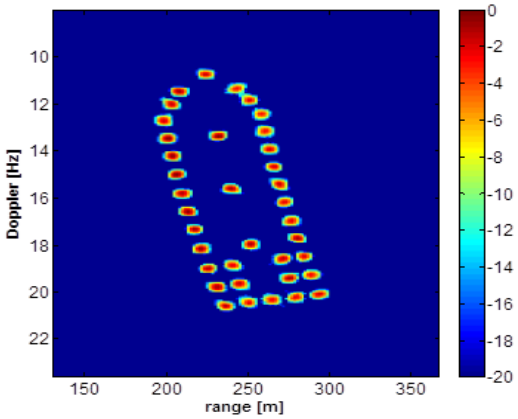


Figure 5.23: P-ISAR image after the cancellation technique

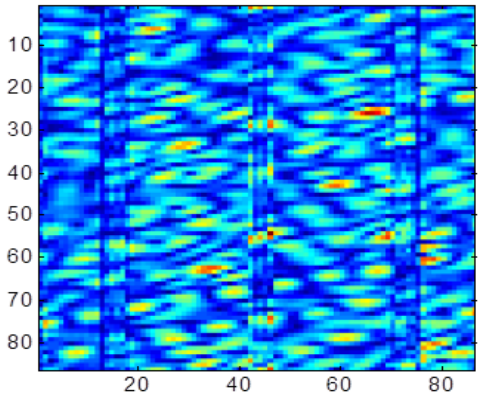


Figure 5.24: Spectral content with the gaps filled out

# Chapter 6

# Results on Real Data

Results based on the use of real data are shown in this section with the aim of proving the P-ISAR concept and to validate the grating lobes cancellation algorithm. Four case studies are presented that refer to four data acquisitions. In the first dataset measured in Pisa (Italy), the target of opportunity was a civilian aircraft. In the second one it was a large ship measured in Livorno's Harbor, whereas the third one was another civilian aircraft, but measured in Madrid (Spain). Before presenting the results, it is worth remarking that:

- the use of only three adjacent DVB-T channels limits significantly the range resolution and therefore meaningful ISAR images of large targets only can be formed
- the bistatic geometry further decreases the ISAR performance in terms of resolutions (both range and cross-range resolutions)
- the low operating frequency (UHF) reduces the cross-range resolution. For these reasons, the P-ISAR images of the ship will highlight the target geometrical features better than in the case of the aircraft, being the latter significantly smaller than the former.

## 6.1 Aerial Target: Boeing 737

The detected target is a BOEING-737 6.1.

Three DVB-T adjacent channels have been acquired. Considering the $24MHz$ of bandwidth and the bistatic angle of 65, due to the target trajectory, the expected range resolution is $\delta_r \cong 7.4m$. The acquisition geometry is depicted in figure 6.2. The transmitter is located on Monte Serra and the


**Wing span: 28,88 m** **Length: 33,40 m**

**Height: 11,13 m**

Figure 6.1: Boeing-737

receiver is located in the radar laboratory in the department of information engineer, in Pisa. The target trajectory is drawn with a blue line and the yellow place marks identify the receiver and the transmitter sites.

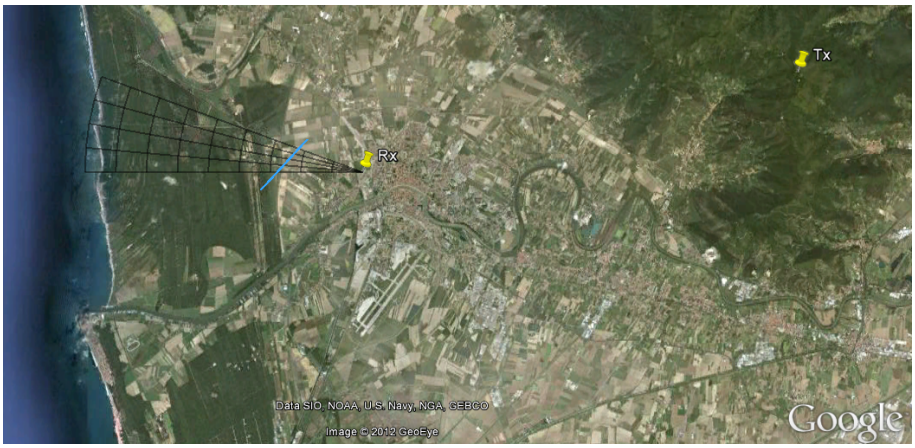


Figure 6.2: Geometry of the real measurements concerning the Boeing-737

The received signal has been acquired by means of low cost hardware solution, that is a Universal Software Radio Peripheral (USRP) device, while the trajectory has been acquired by means of the airnav radarbox device.

Figure 6.3 shows the RD map of the target, which represents the input of the P-ISAR processor.

The RD map of figure 6.3 is obtained by processing data for the whole observation time $4.8s$. As it can be noted, the target is defocused because of

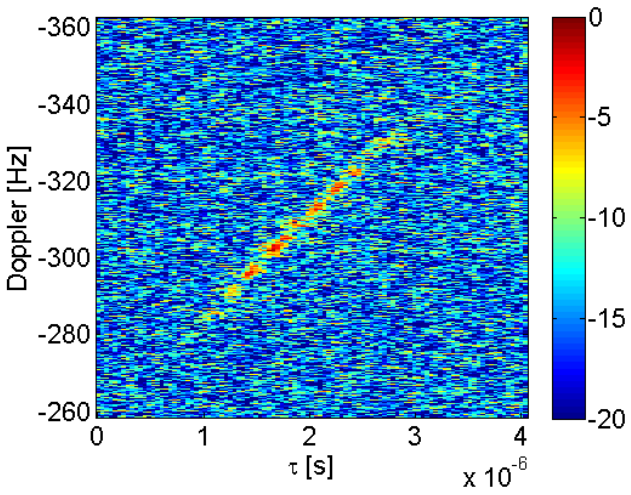


Figure 6.3: Range-Doppler map

the target motion. Figure 6.4 shows the output of the P-ISAR processor, that is the ISAR image.

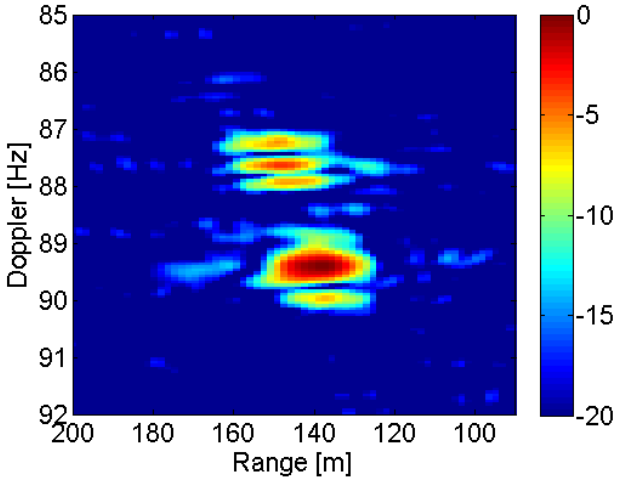


Figure 6.4: P-ISAR image of the target

By comparing figure 6.3 and figure 6.4 can be appreciated the goodness of the P-ISAR processing. The target is now well focused and the main structures can be identified. The shadowing effects, the low central frequency imposed by the illuminator of opportunity, the middle size target, are the main agents for the ISAR image deterioration. In order to better understand the obtained result, the figure 6.5 shows the ISAR image obtained by simulating a point-like

target of the same size and with the same trajectory of the real target.

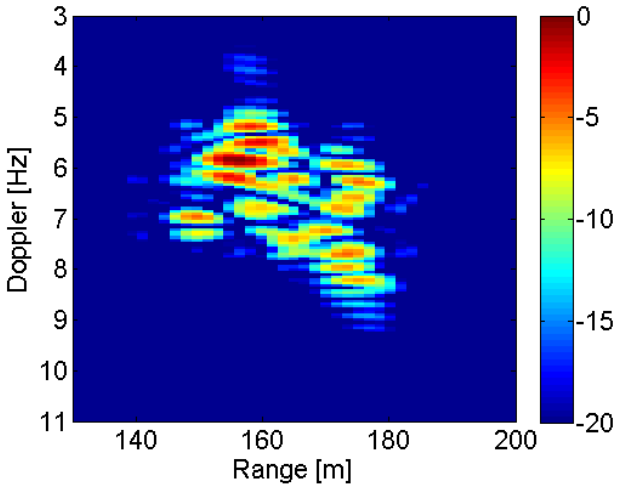


Figure 6.5: Simulated P-ISAR image by substituting the real target with a point-like scatterer one.

By comparing figure 6.4 and figure 6.5, it is worth noting that both images occupy the same number of cells in the Doppler dimension and they have the same orientation. The size of the aircraft in the range dimension is under estimated because of the before mentioned issues. This failing could be considerably improved by using more than three DVB-T channels.

## 6.2 Maritime Target: container ship LIWIA P

The acquisition geometry of the ship dataset is depicted in figure 6.7. The transmitter is the DVB-T illuminator of opportunity located on Monte Serra, and the receiver was located at the Naval academy in Livorno. The wideband signal is composed of three adjacent DVB-T channels centered at $f_0 = 690\ MHz$. In Figure 6.7, the real target trajectory has been represented with a dark line by exploiting available Automatic Identification System (AIS) data. The considered target, shown in Figure 6.6, is a container ship (LIWIA P) of 212 $m$ of length and 32 $m$ of width. The ship was approaching the harbor. The BEM's line of sigth (LoS) is also shown in figure 6.7 .

Figure 6.8 shows a Range-Doppler map obtained by cross-correlating the reference signal and the target signal. The target of interest is circled to highlight its position in bistatic range and Doppler. Such RD map has been

Figure 6.6: A picture of the target used in the first experiment - the target was a container ship


Figure 6.7: Geometry of real data

obtained by processing 800 $ms$ of the available data, which is a reduced dataset used to form a RD map for target detection. The Time delay is related to the target-transmitter and target-receiver distance by the following equation:

$$\tau = \frac{D_{T_x T_g} + D_{R_x T_g} - D_{T_x R_x}}{c} \tag{6.1}$$

where $D_{T_xT_g}$, $D_{R_xT_g}$ and $D_{T_xR_x}$ are, respectively, the distances between the transmitter and the target, the receiver and the target and the transmitter and the receiver, and $c$ is the speed of light in vacuum. From equation 6.1 and by knowing the time delay, the pointing of the receiving antenna and the transmitter and receiver positions, it is possible to estimate the target's distance from the receiver.

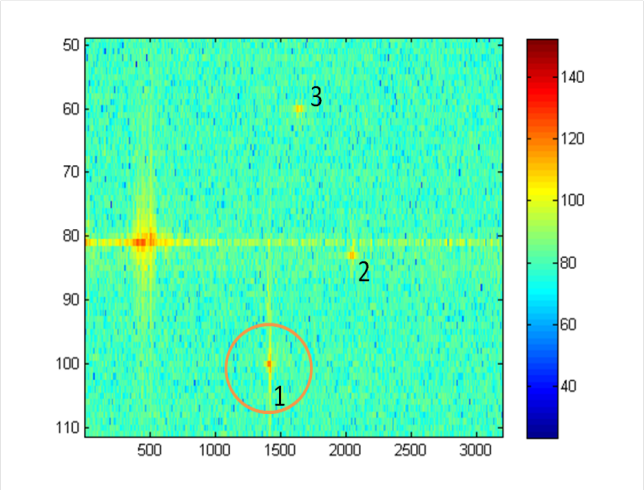


Figure 6.8: Range-Doppler map

As shown in Figure 6.8, for detection purposes small integration time may be sufficient. In this case small targets (small compared to the range and Doppler resolutions) appear as a point in the RD map. For radar imaging purposes, however, longer integration time are needed in order to obtain finer Doppler resolutions. In such a condition, range migration and Doppler frequency changes may occur causing defocusing effects and range and Doppler spread. This, can be noted by observing figure 6.9 where the image of the unfocused target, cropped from a Range Doppler map obtained by processing the whole data ($T_{obs} = 20\ \ s$), is shown.

After the target extraction step, the data in the image domain has been projected back to the data domain, so the range profiles of the target are obtained and are shown in figure 6.10. Specifically, the range profiles are obtained by Inverse Fourier transforming the range-Doppler map in figure 6.9, along the Doppler frequency. Typical range profiles of a moving target are clearly visible. Figure 6.10 highlights the need to compensate radial motion with an autofocusing technique. As detailed in 4.5.4, a suitable time-windowing operation should be used to select data by finding a time interval where the target rotation vector is constant enough to generate a stationary image plane and

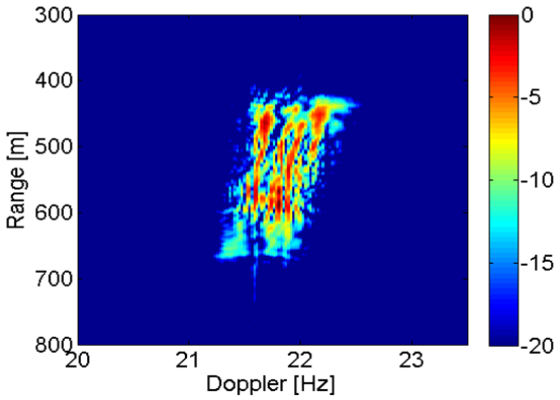


Figure 6.9: Crop of the unfocused target

relatively constant Doppler components. In this case study, two time windows have been selected, as shown in figure 6.10. The results relative to the two time windows are shown below.

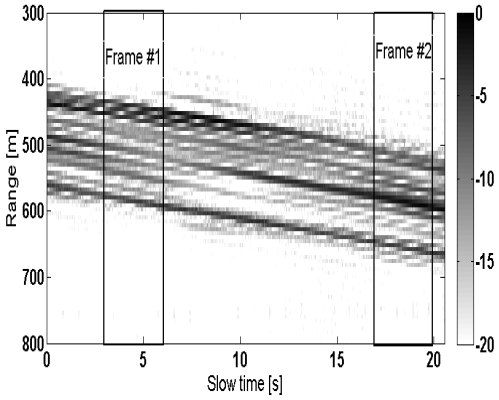


Figure 6.10: Range Profiles of the unfocused target

- Frame 1

The range profiles relative to the first data-frame are shown in Figure 6.10. The autofocus technique adopted here is the ICBA algorithm 4.5.2 based on the image contrast maximisation. The obtained ISAR image is shown in figure 6.11.

It is worth nothing that the ISAR image shown in Figure 6.11 is a projection of the target onto the Image Projection Plane (IPP). For this reason, the estimated target's size could be smaller than the real one. Furthermore, the

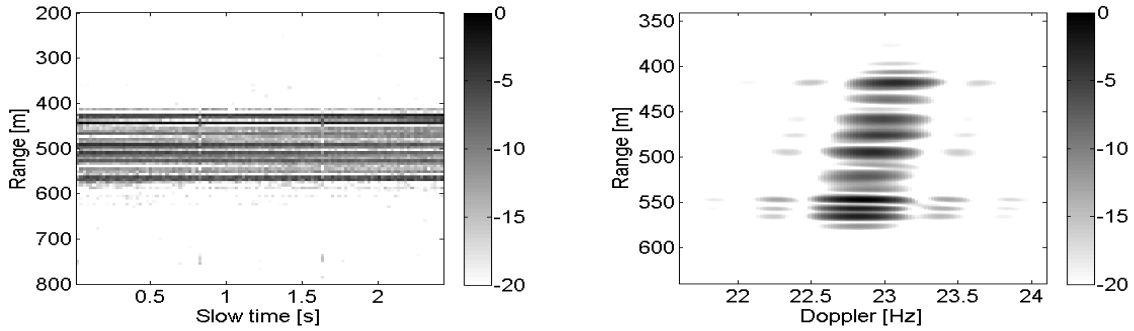


Figure 6.11: Results obtained by considering data frame 1: (left) range profile of the target after autofocusing, (right) ISAR image of the target

range resolution is poor because only three adjacent channels have been used. It should also be mentioned that not all parts of the ship necessarily scatterer energy towards the receiver, either because they are shadowed by other parts of the ship or because scattering mechanisms are too weak to be measured by the receiver. The ISAR image shown in Figure 6.11 is affected by the presence of grating lobes. As already stated in the section 4.7, such grating lobes are due to the presence of bandwidth gaps, which arise when a multi-channel DVB-T signal is used. In order to eliminate them, the algorithm presented in section 4.7 has been applied. The resulting P-ISAR image obtained is shown in Figure 6.12.

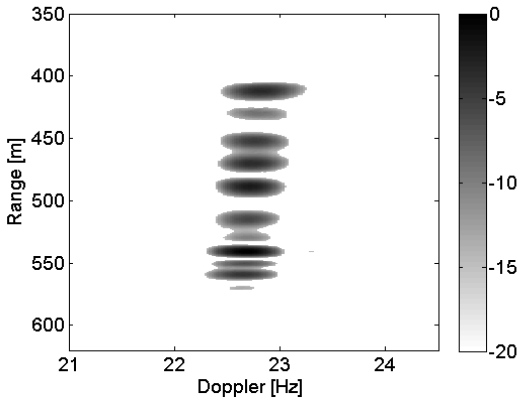


Figure 6.12: ISAR image of the target by considering the frame1, after the Grating Lobes cancellation

- Frame 2

The second frame concerns the last part of the target trajectory. The range profiles relative to the second frame are shown in figure 6.10. The obtained P-ISAR image is shown in the figure 6.13.

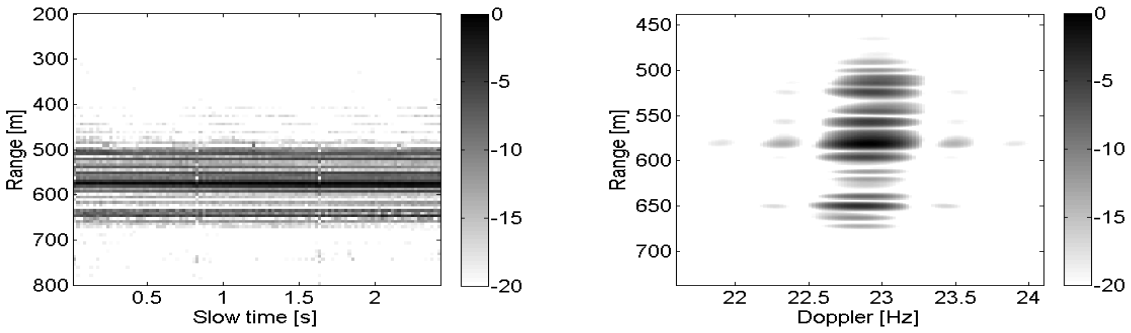


Figure 6.13: Results obtained by considering data frame 2: (left) range profile of the target after autofocusing, (right) ISAR image of the target

As mentioned before, the ISAR image shown in figure 6.13 is a projection of the target onto the IPP. For this reason the estimated size could be smaller than the real one. By comparing figure 6.11 and figure 6.13, a slightly different orientation of the ship can be appreciated between the two frames. This is probably due to the presence of ship's oscillating motions induced by sea waves. Oscillating motions generally produce IPP changes from frame to frame, as noticeable by comparing the two P-ISAR images. Figure 6.14 shows the result of the greating lobes cancellation algorithm, applied to the ISAR image in figure 6.13.

## 6.3 Aerial Target: Airbus 340

The acquisition geometry of the aircraft dataset is depicted in Figure 6.16. The transmitter is the DVB-T illuminator of opportunity located on the Torrespana tower (Madrid), whereas the receiver was located in Paracuellos de Jarama. The solid dark line indicates the real trajectory of the detected target, which was measured by using an Automatic Dependent Surveillance - Broadcast (ADS-B) receiver. The detected target, shown in figure 6.15, was an Airbus 340-313X. The target is 63 m long and has a wingspan of 60 m. It was acquired by using the passive radar prototype, see figure4.1, built under the APIS project.

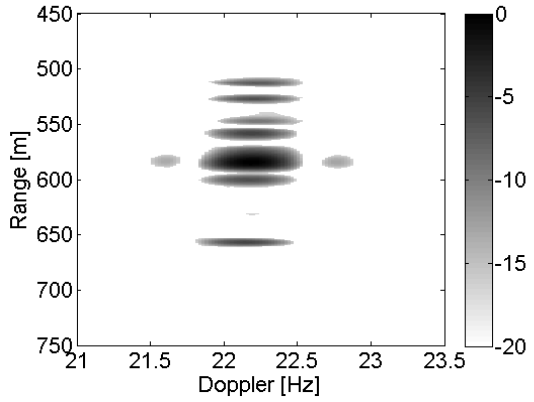


Figure 6.14: ISAR image of the target by considering the frame2, after the Grating Lobes cancellation

Figure 6.15: A picture of the target used in the second experiment - the target was an Airbus 340-313X

The receiver's, trasmitter's and the target's height, were of 630 $m$, 790 $m$ and 690 $m$, respectively. The target's trajectory was 25° off the Bistatic LoS. The wideband signal was composed of three adjacent DVB-T channels centered at the frequency $f_0 = 850\ MHz$.

The output of the standard passive radar processing chain is the Range-Doppler map, which is shown in Figure 6.17. The map has been obtained by processing 400 $ms$ of the available data. The observation time used for imaging purposes is instead equal to $T_{obs} = 25s$. The target has a Doppler frequency of, approximately, $f_d = 250\ Hz$, which corresponds to a radial velocity equal to $v_r = 44\ m/s$.

Figure 6.18 shows the unfocused target's range-Doppler image obtained by


Figure 6.16: Geometry of real data-aerial target

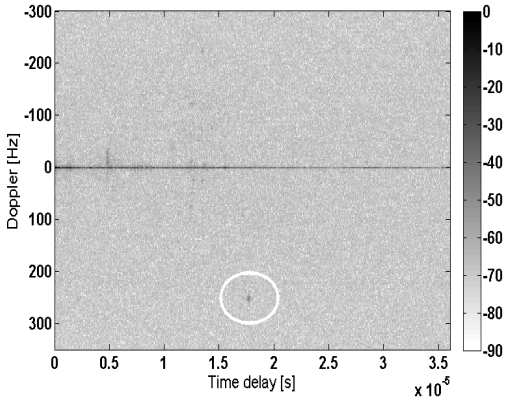


Figure 6.17: Range-Doppler map -Airbus 340

processing the entire dataset (25 s).

The range-Doppler profiles obtained by IFT the RD data in Figure 6.18 are shown in Figure 6.19

Because of target's own complex motions, the P-ISAR algorithm is not able to produce a focused image of the target when the entire dataset is processed. This is due to the fact that the conditions needed to form a well-focused ISAR image are not satisfied. Therefore, a shorter CPI has been chosen by time-windowing the data, as depicted in Figure 6.19. The obtained ISAR image is shown in Figure 6.20

Given the bandwidth of the multichannel DVB-T signal (24 MHz) and the

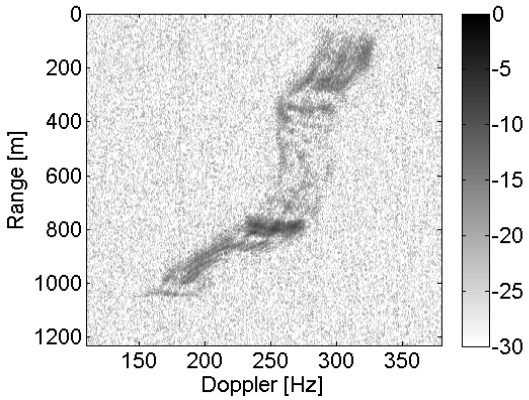


Figure 6.18: Unfocussed target image -Airbus 340

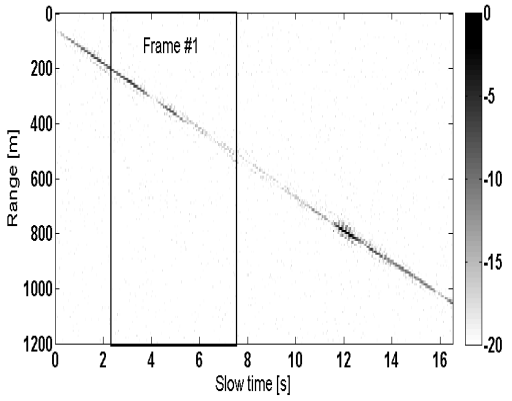


Figure 6.19: Range Profiles of the unfocused target - Airbus 340

bistatic angle, which was approximately 90°, the range resolution is equal to 8.48 $m$, which is quite coarse with respect to the target size. Moreover, as the direction of the target's trajectory was only a few degrees off with respect of the BEM LoS, a target's top view is difficult to obtain. In these conditions, a meaningful P-ISAR image of an aircraft is difficult to obtain as shown in Figure 6.20. Figure 6.21 shows the result of the greating lobes cancellation algorithm when applied to the ISAR image shown in Figure 6.20.

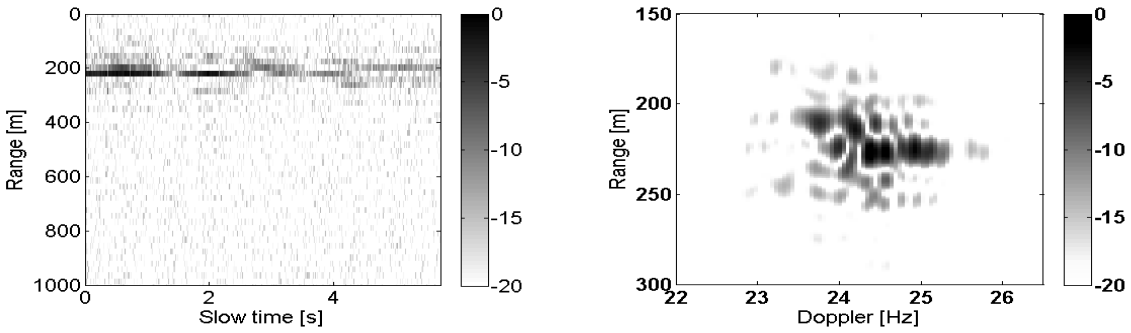


Figure 6.20: (left) range profile of the target after autofocusing, (right) ISAR image of the target

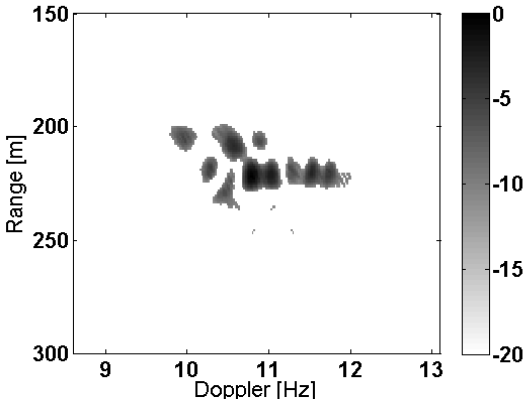


Figure 6.21: ISAR image of the target after Grating Lobes cancellation - Airbus 340

# Chapter 7

# Conclusions

Novel contributions in algorithm development for SAR signal processing has been given. In particular, a general mathematical algorithm was developed for bistatic circular SAR imaging, in the near field region and for the three dimensional reconstruction. The algorithm was implemented and tested on simulated data as well as data recorded in anechoic chamber, mapping its theoretical performance. Furthermore, the algorithm was used to design the final system prototype that is going to be built once the Melissa project will concluded. Starting from some imaging requirements that the final system has to comply with, the working frequency, the receiving array, the sampling criteria, the transmitted waveform were designed. The geometric and radiometric resolutions were analyzed, a theoretical discussion on the signal model was performed and several numerical simulation were performed in order to confirm or to change the MELISSA project requirements. Finally, the designed parameters for the final prototype were summed up in the section 2.4. In the second part of this thesis, novel contributions in algorithm development for ISAR signal processing has been addressed, in particular the ISAR processing was applied to the PBR world, by defining the P-ISAR frame-work, which has not been seen elsewhere. A P-ISAR processing scheme based on multichannel DVB-T signals was proposed that proves the concept. Results based on the application of the proposed algorithm to real life targets of opportunity, have shown that well focused ISAR images can be produced by exploiting passive radars and by using a suitable P-ISAR processing. Grating lobes generated by the gaps present between adjacent DVB-T channels can also be reduced by applying the novel technique proposed in this thesis. Although the technique proposed is still quite heuristic, it shows quite interesting results both on simulated and real data. It must be reminded that the results obtained cannot compete with those obtainable with a dedicated active ISAR system. Nevertheless, an image resolution improvement would be achieved by adjoin-

ing more DVB-T channels, which in our case were limited by the hardware used to collect the data. To conclude, it should be pointed out that with a simple passive radar demonstrator and by making use of P-ISAR processing, it is possible to form bistatic passive ISAR images at those frequencies where it is usually forbidden to transmit, such as Very High Frequency (VHF) and Ultra High Frequency (UHF). Passive ISAR may be therefore a useful tool to measure bistatic Radar Cross Section (RCS) of targets of interests, including mono-statically stealthy targets.

# Bibliography


[1] D. M. Sheen, D.L. McMakin, and T.E. Hall, *Three-Dimensional Millimiter-Wave Imaging for Concealed Weapon Detection*. IEEE Transaction on microwave theory and techniques, vol.49, no.9, September 2001.

[2] F.Berizzi, G.Corsini, *A new Fast Method for the Reconstruction of 2-D Microwave Images of Rotating Objects*,IEEE Transaction on Image Processing, vol.8, no.5, May 1999.

[3] A.Ishimaru, T.K.Chan, and Y.Kuga, *An Imaging Technique Using Confocal Circular Synthetic Aperture Radar*,IEEE Transaction on Geoscience and Remote Sending,vol.36, no.5, September 1998.

[4] W.L. Stuzman, G.A. Thiele, *Antenna Theory and Design*,New York, John Wiley and sons, 1981.

[5] F.Berizzi, *I Sistemi di Telerilevamento Radar*, Apogeo,2005.

[6] J. Fortuny,*An Efficient 3D Near Field ISAR Algorithm*, IEEE Transaction on Aerospace and Electronic Systems, Vol. 34, No.4, October 1998

[7] D. Olivadese, E. Giusti, F. Berizzi, M. Martorella, F. Lombardini, *Near field 3D circular SAR imaging* , Synthetic Aperture Radar (APSAR), 2011 3rd International Asia-Pacific Conference on, pp. 1-4, 26-30 Sept. 2011.

[8] M.Martorella, J.Palmer, J.Homer, B.Littleton, I.D. Longstaff,*On Bistatic Inverse Synthetic Aperture Radar*, IEEE Transaction on Aerospace and Electronic Systems, Vol. 43, pp.1125-1134, 2007

[9] Constantine A. Balanis, *Antenna Theory: Analysis and Design*, John Wiley and Sons, 1996.

[10] B. Riddle, J.Baker - Jarvis, and J. Krupka, "Complex Permittivity Measurements of Common Plastics Over Variable Temperatures, "IEEE Trans. on Microwave Theory and Techniques, vol.51, no.3,pp.727-733, March 2003.

[11] B.B Glover, W.L. Perry, "Microve Properties of TABS particles from Measurements of the Effective Permittivity of TATB Powders, "Propellants Explos. Pyrotech. vol. 34, pp. 347 - 350, 2009.

[12] O.M.Bucci, L.Crocco,T.Isernia, and V.Pascazio, "Inverse Scattering Problems with Multifrequency Data: Reconstruction Capabilities and Solution Strategies, "IEEE Trans. on Geosc. and Rem. Sens., vol.38, n4, pp. 1749-1756, July 2000.

[13] M. Malanowski and G. Mazurek and K. Kulpa and J. Misiurewicz, "FM based PCL radar demonstrator ", Proceedings of the International Radar Symposium, 2007

[14] M. Glende and J. Heckenbach and H. Kuschel and S. Muller and J. Schell and C. Schumacher,"Experimental passive radar systems using digital illuminators (DAB/DVB-T) ", Proceedings of the International Radar Symposium, 2007.

[15] H. Kuschel and J. Heckenbach and J. Schell and D. O'Hagan and M. Ummenhofer, "DVBT passive radar systems PETRA/ CORA ", 2nd Passive radar FHR-PCL-focus day(s), 2009.

[16] M. Conti and D. Petri and A. Capria and M. Martorella and F. Berizzi and E. Dalle Mese, "Ambiguity Function Sidelobes Mitigation in Multichannel DVB-T Passive Bistatic Radar", Proceedings of the International Radar Symposium, 2011.

[17] M. Conti and F. Berizzi and D. Petri and A. Capria and M. Martorella, "High range resolution DVB-T passive radar ", Proceedings of the European Radar Conference (EURAD), 2010.

[18] M. Martorella and J. Palmer and J. Homer and B. Littleton and I. D. Longstaff, "On Bistatic Inverse Synthetic Aperture Radar",on Aerospace and Electronic Systems, 1125-1134, vol.43, 2007.

[19] M. Martorella and E. Giusti and F. Berizzi and A. Bacci and E. Dalle Mese, "ISAR Based Technique for Refocussing Non-cooperative Targets in SAR Images ", IET Radar, Sonar, Navigation, 1-9,vol.6,2012.

[20] Suwa, K. et al., "ISAR imaging of an aircraft target USING ISDB-T digital TV based passive bistatic radar ", IGARSS 2010, 4103-4105. 25-30 July 2010.

[21] Nakamura, K. et al., "An experimental study of enhancement of the cross-range resolution of ISAR imaging using ISDB-T digital TV based bistaic radar", IGARSS 2011, 2837-2840, 24-29 July 2011.

[22] Martorella, M. and Berizzi, F. and Haywood, B., "A Contrast Maximization Based Technique for 2D ISAR Autofocusing ", IEE Proceedings-Radar, Sonar and Navigation,253-262, Vol.152, 2005.

[23] M. Martorella, F. Berizzi, "Time Windowing for highly focused ISAR image reconstruction ", Aerospace and Electronic Systems, IEEE Transaction on, Vol. 41, Issue 3, pp. 992-1007, 2005.

[24] M. Martorella, "Novel approach for ISAR image cross range scaling", Aerospace and Electronic System, IEEE Transaction on, vol. 44, Issue 1, pp. 281-294, 2008.

[25] N.J. Willis, "Bistatic Radar ", Silver Spring, MD, USA: Technology Service Corporation, 1995.

[26] M.C.Jackson, "The geometry of Bistatic Radar Systems ", IEE Proc. 133(7) Pt.F,pp.604-612,December 1986.

[27] J.E.Olsen, "Investigation of bandwidth utilisation methods to optimise performance in passive bistatic radar ", PhD thesis.

[28] ETSI EN 300 744 V1.6.1 (2009-01): "Digital Video Broadcasting (DVB); Framing structure, channel coding and modulation for digital terrestrial television".

[29] Ausherman, D. A. and Kozma, A. and Walker, J. L. and Jones, H. M. and Poggio, E. C.,"Developments in Radar Imaging ", IEEE Transactions on Aerospace and Electronic Systems, 363-400, vol.20,1984.

[30] Walker, J. L., "Range-Doppler Imaging of Rotating Objects ", IEEE Transactions on Aerospace and Electronic Systems, 23-52, vol.16, 1980.

[31] D. Olivadese and M. Martorella and E. Giusti and D. Petri and F. Berizzi, "Passive ISAR with DVB-T Signal ", Proceedings of the EUSAR , 2012.

[32] Olivadese, D. and Martorella, M. and Berizzi, F., "Multi-channel P-ISAR grating lobes cancellation ", Radar 2012, International conference on radar systems, October 2012.

[33] D. Olivadese, E. Giusti, D. Petri, M. Martorella, A. Capria, F. Berizzi, R. Soleti,"PASSIVE ISAR IMAGING OF SHIPS BY USING DVB-T SIGNALS ", Radar 2012, International conference on radar systems, October 2012.

[34] H. C. Stankintz, M.R. Kosek, "Sparse aperture fill for SAR using Super-SVA", Proceedings of the IEEE National Radar Conference, 13-16 May 1996.

[35] W. Zhai, Y. Zhang, "Aplly Super-SVA to SAR Imaging with Both Aperture Gaps and Bandwidth Gaps ", World Academy of Science, Engineering and Technology, 2009.